Geosynthetic Reinforcement of Flexible Pavements: Laboratory Based Pavement Test Sections

FHWA/MT-99-001/8138

PB99-145799

Final Report

Prepared for the
STATE OF MONTANA
DEPARTMENT OF TRANSPORTATION
RESEARCH, DEVELOPMENT AND TECHNOLOGY TRANSFER PROGRAM
in cooperation with the
U.S. DEPARTMENT OF TRANSPORTATION
FEDERAL HIGHWAY ADMINISTRATION

March 17, 1999

Prepared by

Dr. Steven W. Perkins
Associate Professor
Department of Civil Engineering
Montana State University – Bozeman
Bozeman, Montana 59717
Office Telephone: 406-994-6119
Fax: 406-994-6105
E-Mail: stevep@ce.montana.edu

REPRODUCED BY
U.S. DEPARTMENT OF COMMERCE
NATIONAL TECHNICAL
INFORMATION SERVICE
SPRINGFIELD, VA 22161

TECHNICAL REPORT STANDARD PAGE

1. Report No. **FHWA/MT-99-001/8138**	PB99-145799	3. Recipient's Catalog No.
4. Title and Subtitle **Geosynthetic Reinforcement of Flexible Pavements: Laboratory Based Pavement Test Sections**	5. Report Date **March 17, 1999** 6. Performing Organization Code **MSU G&C #290471**	
7. Author **Steven W. Perkins, Ph.D., P.E.**	8. Performing Organization Report No.	
9. Performing Organization Name and Address **Department of Civil Engineering 205 Cobleigh Hall Montana State University Bozeman, Montana 59717**	10. Work Unit No. 11. Contract or Grant No. **8138**	
12. Sponsoring Agency Name and Address **Montana Department of Transportation 2701 Prospect Avenue P.O. Box 201001 Helena, Montana 59620-1001**	13. Type of Report and Period Covered **Final: October 1, 1996 – February 22, 1999** 14. Sponsoring Agency Code **5401**	

15. Supplementary Notes
Preparation in cooperation with the U.S. Department of Transportation, Federal Highway Administration

16. Abstract

Over the course of the last 17 years, approximately 12 different studies have shown the potential for the use of geosynthetic materials (geogrids and geotextiles) as a reinforcement inclusion in the base course aggregate layer of flexible pavements. The attraction of this application lies in the possibility of reducing the thickness of the base course layer such that a roadway of equal service life results or in extending the service life of the roadway. While several existing studies have provided data that aids in describing mechanisms of reinforcement, detailed information required to understand the mechanisms by which geosynthetics reinforce flexible pavements is lacking. In the absence of this information, it has historically been difficult to create mechanistic-based models that adequately describe the process. As such, efforts to establish design solutions have been based largely on empirical data and considerations. Existing design solutions have not been met with open acceptance due to their inability to predict performance for conditions other than those established in the experiments for which the solution was based.

This research was undertaken to provide experimental data that could be used to further establish the mechanisms of geosynthetic-reinforcement that lead to enhanced pavement performance. Subsequent work will involve the use of this data in developing numerical models and design solutions for this application. Pavement test sections have been constructed in a laboratory-based pavement test facility. The facility consists of a large concrete box in which field-scale pavement layers can be constructed. Loading is provided through the application of a cyclic, 40 kN load applied to a stationary plate resting on the pavement surface. The test sections have been instrumented with an extensive series of stress and strain cells. Test section variables have included geosynthetic type (two biaxial geogrid products and one woven geotextile), subgrade type and strength, placement position of the geosynthetic in the base course layer and base course layer thickness.

The results have shown that the inclusion of a geosynthetic provides a significant reinforcement effect. The geosynthetic is shown to have an influence on the amount of lateral spreading that occurs in both the bottom of the base course layer and in the top of the subgrade. Reinforcement is also seen to produce a more distributed vertical stress distribution on the top of the subgrade. As a result of these effects, reinforcement limits the vertical strain developed in the base and subgrade layers, leading to less surface deformation. Given that these mechanisms result from the development of shear interaction between the base and the geosynthetic, the combination of these effects is termed a mechanism of a shear-resisting interface. These effects are seen to be most significant for a soft subgrade where substantial improvement in pavement performance, defined in terms of permanent pavement deformation, has been observed. Geosynthetic type, strength, stiffness and placement position in the base course layer is also seen to influence observed improvement.

17. Key Words **Pavements, Highways, Geogrid, Geotextile, Geosynthetic, Reinforcement, Base Coarse, Test Sections, Instrumentation, Montana**		18. Distribution Statement **Unrestricted. This document is available through the National Technical Information Service, Springfield, VA 21161.**	
19. Security Classif. (of this report) **Unclassified**	20. Security Classif. (of this page) **Unclassified**	21. No. of Pages **140**	22. Price

PREFACE

DISCLAIMER

The opinions, findings and conclusions expressed in this publication are those of the authors and not necessarily those of the Montana Department of Transportation or the Federal Highway Administration

ALTERNATE FORMAT STATEMENT

MDT attempts to provide reasonable accommodations for any known disability that may interfere with a person participating in any service, program or activity of the department. Alternative accessible formats of this document will be provided upon request. For further information, call (406) 444-7693 or TTY (406) 444-7696.

NOTICE

The authors, the State of Montana, and the Federal Highway Administration do not endorse products or manufacturers. Trade and manufacturers names appear herein solely because they are considered essential to the object of the report.

PROTECTED UNDER INTERNATIONAL COPYRIGHT
ALL RIGHTS RESERVED.
NATIONAL TECHNICAL INFORMATION SERVICE
U.S. DEPARTMENT OF COMMERCE

ACKNOWLEDGMENTS

The author gratefully recognizes the generous financial and technical support of the Montana Department of Transportation for this project and projects leading up to this current work. The individual effort of personnel at the MDT-Bozeman Maintenance Yard where this experimental work was performed is highly appreciated. The tireless and dedicated efforts of Dr. Muhannad Ismeik, Mr. Mac Fogelsong, Mr. Yan Wang, Mr. Eli Cuelho and a host of undergraduate student researchers is gratefully recognized. The Amoco Fabrics and Fibers Company and Tensar Earth Technologies, Incorporated graciously donated geosynthetic materials for the project.

TABLE OF CONTENTS

LIST OF TABLES 1
LIST OF FIGURES 2
CONVERSION FACTORS 6
EXECUTIVE SUMMARY 7
1.0 INTRODUCTION 8
2.0 BASIS FOR RESEARCH: LITERATURE REVIEW 10
3.0 PAVEMENT TEST FACILITY 13
3.1 Test Box and Loading Apparatus 14
3.2 Pavement Layer Materials 17
3.2.1 Asphalt Concrete 17
3.2.2 Geosynthetics 18
3.2.3 Base Course Aggregate 23
3.2.4 Subgrades 25
3.3 Instrumentation 26
3.3.1 Pavement Surface Instrumentation 27
3.3.2 Asphalt Concrete Instrumentation 27
3.3.3 Geosynthetic Instrumentation 28
3.3.4 Soil Stress Instrumentation 28
3.3.5 Soil Strain Instrumentation 29
3.3.6 Temperature and Moisture Instrumentation 29
3.3.7 Data Acquisition 30
3.4 Test Section Construction 31
3.4.1 Pavement Material Placement 32
3.4.2 Instrument Placement 34
3.4.3 Instrument Locations 36
3.4.4 Instrument Calibration 38
3.5 As-Constructed Pavement Layer Properties 38
3.6 Instrument Response and Measurement Consistency 47
4.0 DYNAMIC STRESS AND STRAIN FIELDS 55
5.0 PAVEMENT TEST SECTION RESULTS 64
5.1 Clay Subgrade Sections 64
5.1.1 Rutting Behavior 64
5.1.2 Lateral Base Course Restraint 74
5.1.3 Improved Subgrade Vertical Stress Distribution 84
5.1.4 Reduced Lateral Spreading of Subgrade 87
5.1.5 Mechanisms of Increased Base Course Thickness 91
5.2 Silty Sand Subgrade Sections 93
5.2.1 Rutting Behavior 93
5.2.2 Lateral Base Course Restraint 95
5.2.3 Soil-Geosynthetic Compatibility 98
5.2.4 Subgrade Effects 101
5.3 Discussion 101
6.0 SUMMARY AND CONCLUSIONS 104
7.0 REFERENCES 108
APPENDIX A: INSTRUMENT LOCATIONS 110

LIST OF TABLES

Table 3.2.1	Geosynthetic material parameters.	19
Table 3.4.1	Constructed test section variables.	32
Table 3.5.1	As-constructed asphalt concrete properties.	40
Table 3.5.2	Significance of variations of AC layer properties between test sections.	41
Table 3.5.3	Significance of variations in AC thickness between CS sections.	42
Table 3.5.4	Significance of variations in AC air voids between CS sections.	42
Table 3.5.5	Significance of variations in AC air voids between SSS sections.	43
Table 3.5.6	As-constructed base course properties.	43
Table 3.5.7	Coefficient of variation for base course and subgrade construction.	44
Table 3.5.8	As-constructed subgrade properties.	45
Table 5.1.1	Dynamic load induced in the geosynthetics.	76
Table A1	Instrument locations for test section PCS1	111
Table A2	Instrument locations for test section CS2	113
Table A3	Instrument locations for test section CS5	115
Table A4	Instrument locations for test section CS6	117
Table A5	Instrument locations for test section CS7	119
Table A6	Instrument locations for test section CS8	121
Table A7	Instrument locations for test section CS9	123
Table A8	Instrument locations for test section CS10	125
Table A9	Instrument locations for test section CS11	127
Table A10	Instrument locations for test section SSS1	129
Table A11	Instrument locations for test section SSS2	131
Table A12	Instrument locations for test section SSS3	133
Table A13	Instrument locations for test section SSS4	135
Table A14	Instrument locations for test section SSS5	137
Table A15	Instrument locations for test section SSS8	139

LIST OF FIGURES

Figure 2.1	Illustration of proposed shear-resisting interface mechanism of reinforcement.	12
Figure 3.1.1	Schematic diagram of the pavement test facility.	15
Figure 3.1.2	Image of the pavement test facility.	15
Figure 3.1.3	Image of the pavement load plate and surface instrumentation.	16
Figure 3.1.4	Input load pulse and corresponding load cell measurement.	17
Figure 3.2.1	Grain size distribution of hot-mix aggregate, cold-mix aggregate, base course aggregate and silty sand subgrade.	18
Figure 3.2.2	Rapid loading uniaxial tension test results on geogrid A and the geotextile.	20
Figure 3.2.3	Slow loading uniaxial tension test results on geogrid A and the geotextile.	20
Figure 3.2.4	Cyclic loading uniaxial tension test results on geogrid A and the geotextile.	21
Figure 3.2.5	Shear stress versus normal stress for geogrid A – base aggregate interaction.	22
Figure 3.2.6	Shear stress versus normal stress for geotextile – base aggregate interaction.	23
Figure 3.2.7	Shear modulus versus normal stress for geosynthetic – base aggregate interaction.	23
Figure 3.2.8	CU *q-axial strain* triaxial test results on the base aggregate.	24
Figure 3.2.9	CU q- p' triaxial test results on the base aggregate.	25
Figure 3.2.10	CBR versus compaction water content for the clay subgrade.	26
Figure 3.3.1	Asphalt concrete strain gage.	27
Figure 3.3.2	Typical soil stress cell.	29
Figure 3.3.3	Typical soil strain cell.	30
Figure 3.3.4	Data acquisition system and real-time graphics.	31
Figure 3.4.1	Theoretical stress and strain measurements for an element of soil inside a test section.	37
Figure 3.6.1	Peak vertical strain in the base versus radial distance (PCS1, Z=300 mm).	49
Figure 3.6.2	Peak vertical strain in the subgrade versus radial distance (PCS1, Z=450 mm).	49
Figure 3.6.3	Peak radial strain in the subgrade versus radial distance (PCS1, Z=415 mm).	50
Figure 3.6.4	Peak vertical stress in the base versus radial distance (PCS1, Z=300 mm).	50
Figure 3.6.5	Peak vertical stress in the subgrade versus radial distance (PCS1, Z=675 mm).	51
Figure 3.6.6	Time-history of vertical stress in the subgrade (PCS1, R=0, Z=675 mm).	51
Figure 3.6.7	Time-history of radial strain in the base (PCS1, R=100 mm, Z=355 mm).	52
Figure 3.6.8	Permanent rut development for unreinforced test sections (CS2, CS8).	52
Figure 3.6.9	Permanent radial strain in the base versus load cycle (CS2, CS8, R=200 mm, Z=355 mm).	53
Figure 3.6.10	Dynamic vertical stress in the subgrade versus load cycle (CS2, CS8, R=0, Z=450 mm).	53
Figure 3.6.11	Permanent radial strain in the base versus load cycle (SSS1, SSS4, R=115 mm, Z=215 mm).	54

Figure 3.6.12 Dynamic vertical stress in the subgrade versus load cycle (SSS1, SSS4, R=0, Z=350 mm). 54
Figure 3.6.13 Permanent vertical strain in the subgrade versus load cycle (SSS1, SSS4, R=60 mm, Z=575 mm). 55
Figure 4.1 Dynamic load plate pressure versus displacement (PCS1). 56
Figure 4.2 Peak radial strain in the AC versus radial distance (PCS1, Z=67 mm). 57
Figure 4.3 Peak tangential strain in the AC versus radial distance (PCS1, Z=67 mm). 57
Figure 4.4 Peak vertical stress in the base versus radial distance (PCS1, Z=300 mm). 58
Figure 4.5 Peak vertical strain in the base versus radial distance (PCS1, Z=300 mm). 58
Figure 4.6 Peak radial stress in the base versus radial distance (PCS1, Z=225 mm). 59
Figure 4.7 Peak radial strain in the base versus radial distance (PCS1, Z=355 mm). 59
Figure 4.8 Peak tangential stress in the base versus radial distance (PCS1, Z=300 mm). 60
Figure 4.9 Peak tangential strain in the base versus radial distance (PCS1, Z=355 mm). 60
Figure 4.10 Peak vertical stress in the subgrade versus radial distance (PCS1, Z=450 mm). 61
Figure 4.11 Peak vertical strain in the subgrade versus radial distance (PCS1, Z=450 mm). 61
Figure 4.12 Peak radial stress in the subgrade versus radial distance (PCS1, Z=450 mm). 62
Figure 4.13 Peak radial strain in the subgrade versus radial distance (PCS1, Z=415 mm). 62
Figure 4.14 Peak tangential stress in the subgrade versus radial distance (PCS1, Z=450 mm). 63
Figure 4.15 Peak tangential strain in the subgrade versus radial distance (PCS1, Z=415 mm). 63
Figure 5.1.1 Permanent surface deformation versus load cycle (CS2-CS11). 68
Figure 5.1.2 Permanent surface deformation versus load cycle (CS9, CS10). 68
Figure 5.1.3 TBR for sections CS5, 6, 7, 9 and 11 relative to CS2. 69
Figure 5.1.4 TBR for section CS10 relative to CS9. 69
Figure 5.1.5 Permanent surface deformation bowls for cycle 1 (CS2-CS11). 70
Figure 5.1.6 Permanent surface deformation bowls at cycle 40,000 (CS2-CS11). 70
Figure 5.1.7 Permanent surface deformation bowls for cycle 1 (CS9, CS10). 71
Figure 5.1.8 Permanent surface deformation bowls at cycle 125,000 (CS9, CS10). 71
Figure 5.1.9 Dynamic surface deformation bowls for cycle 1 (CS2-CS11). 72
Figure 5.1.10 Dynamic surface deformation bowls at 12.5 mm permanent deformation (CS2-CS11). 72
Figure 5.1.11 Dynamic surface deformation versus load cycle (CS2-CS11). 73
Figure 5.1.12 Dynamic surface deformation versus load cycle (CS9, CS10). 73
Figure 5.1.13 Permanent radial strain in the base versus load cycle (CS2-CS11, R=100 mm, Z=325 mm). 76
Figure 5.1.14 Permanent radial strain in the base versus load cycle (CS2-CS11, R=200 mm, Z=325 mm). 77
Figure 5.1.15 Permanent radial strain in the base versus radial distance for cycle 1 (CS2-CS11, Z=325 mm). 77

Figure 5.1.16 Permanent radial strain in the base versus radial distance at cycle 40,000 (CS2-CS11, Z=325 mm). 78
Figure 5.1.17 Permanent radial strain in the base versus load cycle (CS9, CS10, R=100 mm, Z=400 mm). 78
Figure 5.1.18 Permanent radial strain in the base versus radial distance at cycle 125,000 (CS9, CS10, Z=400 mm). 79
Figure 5.1.19 Dynamic radial strain in the base versus load cycle (CS2-CS11, R=100 mm, Z=325 mm). 79
Figure 5.1.20 Permanent radial strain in the geosynthetics (M) versus load cycle (CS5-CS11, R=15 mm). 80
Figure 5.1.21 Permanent radial strain in the geosynthetics (XM) versus load cycle (CS5-CS11, R=20 mm). 80
Figure 5.1.22 Permanent radial strain in the geosynthetics (M) versus radial distance at cycle 7500 (CS5-CS11). 81
Figure 5.1.23 Dynamic radial strain in the geosynthetics (M) versus load cycle (CS5-CS11, R=15 mm). 81
Figure 5.1.24 Dynamic radial strain in the geosynthetics (XM) versus load cycle (CS5-CS11, R=20 mm). 82
Figure 5.1.25 Dynamic radial strain in the geosynthetics (M) versus radial distance for cycle 1 (CS5-CS11). 82
Figure 5.1.26 Dynamic radial strain in the geosynthetics (M) versus radial distance at cycle 7500 (CS5-CS11). 83
Figure 5.1.27 Permanent vertical strain in the base versus load cycle (CS2-CS11, R=65 mm). 83
Figure 5.1.28 Dynamic vertical stress in the subgrade versus load cycle (CS2-CS11, R=0, Z=450 mm). 84
Figure 5.1.29 Dynamic vertical stress in the subgrade versus load cycle (CS2-CS11, R=0, Z=625 mm). 85
Figure 5.1.30 Dynamic vertical stress in the subgrade versus load cycle (CS2-CS11, R=0, Z=775 mm). 85
Figure 5.1.31 Dynamic vertical stress in the subgrade versus load cycle (CS2-CS11, R=0, Z=1075 mm). 86
Figure 5.1.32 Dynamic vertical stress in the subgrade versus radial distance at cycle 40,000 (CS2-CS11, Z=450 mm). 86
Figure 5.1.33 Permanent radial strain in the subgrade versus radial distance for cycle 1 (CS2-CS11, Z=415 mm). 88
Figure 5.1.34 Permanent radial strain in the subgrade versus radial distance at cycle 40,000 (CS2-CS11, Z=415 mm). 88
Figure 5.1.35 Permanent radial strain in the subgrade versus radial distance at cycle 125,000 (CS9, CS10, Z=490 mm). 89
Figure 5.1.36 Dynamic radial stress in the subgrade versus load cycle (CS9, CS10, R=250 mm, Z=525 mm). 89
Figure 5.1.37 Permanent vertical strain in the subgrade versus load cycle (CS2-CS11, R=65 mm, Z=450 mm). 90
Figure 5.1.38 Permanent vertical strain in the subgrade versus load cycle (CS9, CS10, R=65 mm, Z=525 mm). 90

Figure 5.1.39 Permanent radial strain in the base versus radial distance at cycle 40,000 (CS2, CS8, CS9). 91
Figure 5.1.40 Dynamic vertical stress in the subgrade versus radial distance at cycle 40,000 (CS2, CS9). 92
Figure 5.1.41 Permanent radial strain in the subgrade versus radial distance at cycle 40,000 (CS2, CS8, CS9). 92
Figure 5.1.42 Permanent vertical strain in the subgrade versus load cycle (CS2, CS9). 93
Figure 5.2.1 Permanent surface deformation versus load cycle (SSS1-SSS4). 94
Figure 5.2.2 Permanent radial strain in the asphalt concrete versus load cycle (SSS1-SSS4, R=0, Z=67 mm). 94
Figure 5.2.3 Permanent radial strain in the base versus load cycle (SSS1-SSS4, R=150 mm, Z=215 mm). 96
Figure 5.2.4 Permanent radial strain in the base versus radial distance at cycle 500,000 (SSS1-SSS4, Z=215 mm). 96
Figure 5.2.5 Permanent vertical strain in the base versus load cycle (SSS1-SSS4, R=60 mm, Z=160 mm). 97
Figure 5.2.6 Permanent radial strain in the geosynthetics (M) versus load cycle (SSS2-SSS9, R=15 mm). 97
Figure 5.2.7 Permanent radial strain in the geosynthetics (XM) versus load cycle (SSS2-SSS9, R=23 mm). 98
Figure 5.2.8 Permanent radial strain in geogrid A and base versus radial distance at cycle 5000 (SSS5). 99
Figure 5.2.9 Permanent tangential strain in geogrid A and base versus radial distance at cycle 5000 (SSS5). 99
Figure 5.2.10 Permanent radial strain in geotextile and base versus radial distance at cycle 5000 (SSS8). 100
Figure 5.2.11 Permanent tangential strain in geotextile and base versus radial distance at cycle 5000 (SSS8). 100
Figure 5.2.12 Dynamic vertical stress in the subgrade versus load cycle (SSS1-SSS4, R=0, Z=350 mm). 102
Figure 5.2.13 Dynamic vertical stress in the subgrade versus radial distance at cycle 5000 (SSS1-SSS4, Z=350 mm). 102
Figure 5.3.1 Dynamic vertical stress in the base versus radial distance at cycle 40,000 (Z=300 mm). 104

CONVERSION FACTORS

The following conversion factors are required for interpretation of results contained in this report.

1 m = 3.28 ft
1 mm = 0.0394 in
1 kN = 225 lb
1 kN/m = 68.6 lb/ft
1 kPa = 0.145 psi
1 $MN/m^3 = 7.94\times10^{-6}$ lb/ft^3

EXECUTIVE SUMMARY

Over the course of the last 17 years, approximately 12 different studies have shown the potential for the use of geosynthetic materials (geogrids and geotextiles) as a reinforcement inclusion in the base course aggregate layer of flexible pavements. The attraction of this application lies in the possibility of reducing the thickness of the base course layer such that a roadway of equal service life results or in extending the service life of the roadway. While several existing studies have provided data that aids in describing mechanisms of reinforcement, detailed information required to understand the mechanisms by which geosynthetics reinforce flexible pavements is lacking. In the absence of this information, it has historically been difficult to create mechanistic-based models that adequately describe the process. As such, efforts to establish design solutions have been based largely on empirical data and considerations. Existing design solutions have not been met with open acceptance due to their inability to predict performance for conditions other than those established in the experiments for which the solution was based.

This research was undertaken to provide experimental data that could be used to further establish the mechanisms of geosynthetic-reinforcement that lead to enhanced pavement performance. Subsequent work will involve the use of this data in developing numerical models and design solutions for this application. Pavement test sections have been constructed in a laboratory-based pavement test facility. The facility consists of a large concrete box in which field-scale pavement layers can be constructed. Loading is provided through the application of a cyclic, 40 kN load applied to a stationary plate resting on the pavement surface. The test sections have been instrumented with an extensive series of stress and strain cells. Test section variables have included geosynthetic type (two biaxial geogrid products and one woven geotextile), subgrade type and strength, placement position of the geosynthetic in the base course layer and base course layer thickness.

The results have shown that the inclusion of a geosynthetic provides a significant reinforcement effect. The geosynthetic is shown to have an influence on the amount of lateral spreading that occurs in both the bottom of the base course layer and in the top of the subgrade. Reinforcement is also seen to produce a more distributed vertical stress distribution on the top of the subgrade. As a result of these effects, reinforcement limits the vertical strain developed in the base and subgrade layers, leading to less surface deformation. Given that these mechanisms result from the development of shear interaction between the base and the geosynthetic, the combination of these effects is termed a mechanism of a shear-resisting interface. These effects are seen to be most significant for a soft subgrade where substantial improvement in pavement performance, defined in terms of permanent pavement deformation, has been observed. Geosynthetic type, strength, stiffness and placement position in the base course layer is also seen to influence observed improvement.

1.0 INTRODUCTION

The use of geosynthetics in the design and construction of roadways has steadily gained acceptance and experienced an increase in popularity as the benefits of its use have become more widely recognized. Geosynthetics have been used for a number of applications where their function generally falls within one of several categories, including separation, filtration, drainage and reinforcement. Within the area of reinforcement, several design applications and corresponding geosynthetic reinforcement mechanisms have been proposed and illustrated. The work discussed in this report addresses the application of geosynthetics, namely geogrids and geotextiles, used for the reinforcement of flexible pavement systems where the geosynthetic is placed in or at the bottom of the base course aggregate layer. For this application, reinforcement must be mobilized and become effective for relatively small levels of surface deformation of the roadway.

The attraction of this application lies in the possibility of reducing the thickness of the base course layer such that a roadway of equal service life results or in extending the service life of the roadway. The first alternative is beneficial if the cost of the geosynthetic is less than the combined cost of the replaced base course material and any construction related costs associated with a reduced base course layer (such as excavation, relocation of utilities, and purchase of right-of-way). Benefits are seen with the second alternative when maintenance and replacement costs are offset by the cost of the geosynthetic. Both alternatives are particularly attractive in areas where quality gravel sources are scarce, in urban areas where these sources have become depleted, or in environmentally sensitive areas where the location of gravel quarries is not permitted.

The sponsor of this project (the Montana Department of Transportation, MDT) became interested in the application of geosynthetics for pavement reinforcement for several reasons revolving around conditions in the eastern part of the state that include: 1) Native clayey (A-6, A-7) subgrade soils that exhibit relatively poor support values that traditionally result in pavement sections with relatively thick base course layers and 2) A lack of quality aggregate material and correspondingly excessive construction costs due to long haul distances. In addition, the region 8 office of the FHWA has required state DOT's under its purview to demonstrate the feasibility of this technology prior to its use in roadways constructed with federal aid funds. The

MDT is mainly interested in the use of geosynthetic reinforcement for the purpose of reducing the design thickness of the base course aggregate layer. The intention of the entire project, however, is to provide a design tool that is sufficiently general to allow for this and other performance benefits to be analyzed.

Prior to granting this contract, MDT personnel evaluated the potential cost benefit to the State of Montana by considering the impact of this research on roadway construction projects scheduled over the next 6 years for districts in the eastern portion of the state where gravel costs are typically the greatest. Construction cost savings was evaluated based on reducing the thickness of the base course layer. Different scenarios were considered with variables including geosynthetic cost, base course aggregate cost and the amount by which the base course layer could be reduced. For all scenarios considered, there was a substantial cost savings that was conservatively estimated as $2 million annually.

As presented in the next section, approximately 12 studies have been conducted over the past 17 years that when taken as a whole, demonstrate the feasibility of this technology. While several of these studies have provided data that aids in describing mechanisms of reinforcement, detailed information required to understand the mechanisms by which geosynthetics reinforce flexible pavements is lacking. In the absence of this information, it has historically been difficult to create mechanistic-based models that adequately describe the process. As such, efforts to establish design solutions have been based largely on empirical data and considerations. Existing design solutions have not been met with open acceptance due to their inability to predict performance for conditions other than those established in the experiments for which the solution was based.

The approach taken in this research is to start from the position that sufficient experimental studies have been conducted that demonstrate the feasibility of this technology. It was believed that additional experimental work was needed with well-instrumented test sections to better define mechanisms of reinforcement such that sufficiently descriptive numerical models could be developed to describe and predict structural response. Once such a model is developed, it can be used to examine the performance improvement of a large number of test sections that cannot all be physically modeled.

This report describes the experimental portion of the work described above. In the remaining sections, a brief review of the literature leading to a basis for the research approach

described above is presented. The experimental facility and test sections constructed are described followed by a presentation and interpretation of the results. Appropriate conclusions are made at the end of this report.

2.0 BASIS FOR RESEARCH: LITERATURE REVIEW

Geosynthetics have been examined and used in practice for reinforcement of the base layer of flexible pavements over the past sixteen years, with both successes and failures reported. Early attempts using geotextiles (Brown et al., 1982; Ruddock et al., 1982; Halliday and Potter, 1984) indicated little improvement in rut development characteristics that could be attributed to geotextile reinforcement. For studies involving both geogrids and geotextiles, Anderson and Killeavy (1989), Barksdale et al. (1989) and Cancelli et al. (1996) have demonstrated that geogrids are superior to geotextiles when used as a reinforcement member, while Al-Qadi et al. (1994) showed that superior performance was seen when a geotextile was used.

Improvement in pavement performance has been observed in laboratory-scale experiments involving stationary circular plates to which a cyclic load has been applied (Cancelli et al., 1996; Haas et al., 1988; Miura et al., 1990), test tracks incorporating moving wheel loads (Barksdale et al., 1989; Collin et al., 1996; Kinney et al., 1998a,b; Moghaddas-Nejad and Small, 1996; Webster, 1993) and full-scale roads constructed with normal construction equipment (Al-Qadi et al., 1998; Anderson and Killeavy, 1989; Mirua et al., 1990). Improvement has been defined in terms of an extension of the life of the pavement, or the amount by which the base course layer could be reduced such that equivalent performance is seen. Reinforced pavements have been shown to have a life typically 3 to 10 times that of a similar unreinforced section, while a reduction of base thickness ranging from 22 to 50 % has been observed. Performance has been measured in terms of permanent rut depth. The influence of reinforcement on fatigue cracking of the asphalt concrete layer has not been fully established.

Studies involving geogrids and geotextiles have provided insight into the importance of the roles of separation and filtration and the ensuing effect on reinforcement potential. The only study available where appreciable mixing of the base course and subgrade soils in control sections was noted (Al-Qadi et al., 1994) also corresponds to the one showing superior performance by the geotextile. Other studies exhibiting more moderate amounts of mixing, and

indicative of conditions for which separation and filtration functions were not as critical (Anderson and Killeavy, 1989; Barksdale et al., 1989) indicate that improvement due to geogrid reinforcement can still be observed, but perhaps not to the extent had separation and filtration functions been incorporated into the section designs. On the other extreme, studies exhibiting no problems with mixing (Cancelli et al., 1996; Collin et al., 1996; Haas et al., 1988; Kinney et al., 1998a,b; Mirua et al., 1990; Moghaddas-Nejad and Small, 1996; Webster, 1993) have demonstrated significant improvement with geogrid reinforcement for properly designed sections.

Improvement has been seen for all levels of rut depth below that corresponding to an inoperable condition (25 mm). Measurement of strain on geogrid layers has shown that strain is developed immediately upon the first load application and well before any appreciable rut is developed in the pavement, provided the reinforcement was properly placed in the base layer. Strain measurements have indicated that these materials are engaged in a tensile capacity and that the level to which strain develops is closely related to the amount of improvement observed. These results indicate that this application is well suited for flexible pavements, which cannot tolerate significant surface deformations and remain operational. Perkins and Ismeik (1997a,b) have provided a more comprehensive review and critique of studies addressing this application.

Historically, the main reinforcement function attributed to geosynthetics in paved roads is what has commonly been referred to as the function of base course lateral restraint. This function was originally described by Bender and Barenberg (1978) and later elaborated on by Kinney and Barenberg (1982) for geotextile-reinforced unpaved roads. This name may be somewhat misleading in that the function, as envisioned, incorporates mechanisms in addition to preventing lateral movement of the base course aggregate. A more appropriate description might be to describe this reinforcement function, and its associated mechanisms, as one of a shear-resisting interface.

The reinforcement function of a shear-resisting interface develops through shear interaction of the base course layer with the geosynthetic layer or layers contained in or at the bottom of the base aggregate (Figure 2.1) and consists of four separate reinforcement mechanisms. Vehicular loads applied to the roadway surface create a lateral spreading motion of the base course aggregate. Tensile lateral strains are created in the base as the material moves down and out

away from the applied load. Lateral movement of the base allows for vertical strains to develop leading to a permanent rut in the wheel path.

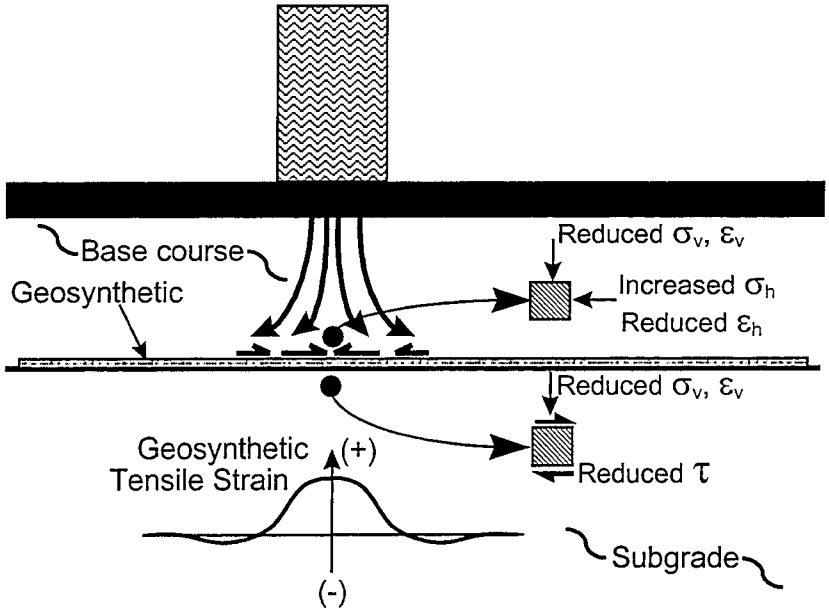

Figure 2.1 Illustration of proposed shear-resisting interface mechanism of reinforcement.

Placement of a geosynthetic layer or layers in the base course allows for shear interaction to develop between the aggregate and the geosynthetic as the base attempts to spread laterally. Tensile load is effectively transmitted from the base aggregate to the geosynthetic. Since the geosynthetic is considerably stiffer in tension as compared to the aggregate, far less lateral tensile strain develops in the system. Lower lateral strain in the base results in less vertical deformation of the roadway surface. Hence, the first mechanism of reinforcement corresponds to direct prevention of lateral spreading of the base aggregate.

Shear stress developed between the base course aggregate and the geosynthetic provides an increase in lateral stress within the base. This increase in lateral confinement leads to an increase in the mean hydrostatic stress. Granular materials generally exhibit an increase in elastic modulus with increasing mean stress. The second reinforcement mechanism results from an increase in stiffness of the base course aggregate when adequate interaction develops between the base and the geosynthetic. The increased stiffness of this layer results in lower vertical strains in the base. It would also be expected that an increase in modulus of the base would result in lower dynamic, recoverable vertical deformations of the roadway surface, implying that

fatigue of the asphalt concrete layer would be reduced. Models of reinforcement incorporating this mechanism include Kinney et al. (1998a) and Sellmeijer (1990).

The presence of a geosynthetic layer in the base can also lead to a change in the state of stress and strain in the subgrade. For layered systems, where a weaker subgrade material lies beneath the base, an increase in modulus of the base layer results in an improved vertical stress distribution on the subgrade. In general, the vertical stress in the base and subgrade directly beneath the applied load should decrease as the base layer stiffness increases. The vertical stress on the subgrade will become more widely distributed, meaning that surface deformation will be less and more uniform. Hence, a third reinforcement mechanism results from an improved vertical stress distribution on the subgrade.

The fourth reinforcement mechanism results from a reduction of shear stress in the subgrade soil. It is expected that shear stress transmitted from the base course to the subgrade would decrease as shearing of the base transmits tensile load to the reinforcement. Less shear stress, coupled with less vertical stress results in a less severe state of loading leading to lower vertical strain in the subgrade.

Prerequisite to realizing the reinforcement mechanisms described above is the development of a strain distribution in the geosynthetic similar to that shown in Figure 2.1. Haas et al. (1988) and Miura et al. (1990) have presented data demonstrating such trends for paved roadways using geogrid reinforcement. Haas et al. has also shown that vertical stress on the subgrade was less when reinforcement was present. While these studies have provided data that aids in illustrating the mechanisms described above, additional data is needed to understand the mechanisms by which geosynthetics reinforce flexible pavements. This information is needed to proceed with research designed to provide numerical models that predict reinforced pavement response. Described in the remainder of this report is experimental work designed to provide insight on the mechanical response of geosynthetic reinforced pavement systems.

3.0 PAVEMENT TEST FACILITY

A test facility was designed and constructed for the purpose of conducting laboratory, large-scale experiments on reinforced and unreinforced pavement sections. The facility was designed to mimic pavement layer materials and geometry, and loading conditions encountered

in the field as realistically as possible with an indoor, laboratory based facility. This type of facility was chosen for this phase of the work because of the control that could be exercised on the construction and control of pavement layer material properties.

Pavement layer materials are similar to those commonly used and encountered in the field. AC and base aggregate layer thickness could be chosen to match most any field condition. Actual layer thickness used in corresponds to sections commonly used on secondary and some primary roadways in Montana. A cyclic, non-moving load with a peak load value of 40 kN was used to mimic dynamic wheel loads. An extensive array of sensors to measure stress, strain, temperature and water content in various pavement layers was used to characterize mechanical response in and without the presence of reinforcement. Descriptions of these components of the facility are provided in the sections below along with a description of test section construction techniques, quality control measures and test section configurations constructed.

A total of 21 sections were constructed. Twelve sections were constructed using a soft clay subgrade. Results from 2 of these 12 sections are not presented for reasons described in Section 3.5 (pg. 46). An additional 9 sections were constructed using a more competent silty sand subgrade. The clay subgrade and silty sand subgrade test sections are referred to as CS and SSS sections, respectively. One of the 12 clay subgrade sections constructed was termed a preliminary clay section (PCS) in that it was constructed for the purpose of establishing a general idea of behavior for the remaining clay sections. This preliminary test section also contained less and differently spaced instrumentation as compared to the remaining sections.

Test section variables examined and implemented into the experimental program consisted of subgrade type, geosynthetic type and location within the base course, and base course layer thickness. Construction of the 21 test sections included in this report began in December, 1996 and terminated in November, 1998.

3.1 Test Box and Loading Apparatus

A test box was constructed having inside dimensions of 2 m in width and length and 1.5 m in height. Walls consisted of 150 mm thick reinforced concrete. The bottom of the box was left open. The front wall is removable in order to facilitate excavation of the test sections. The front wall is attached by 25 mm diameter bolt and nut assemblies. Figure 3.1.1 shows a schematic of the pavement test facility. Figure 3.1.2 shows an actual image of the facility.

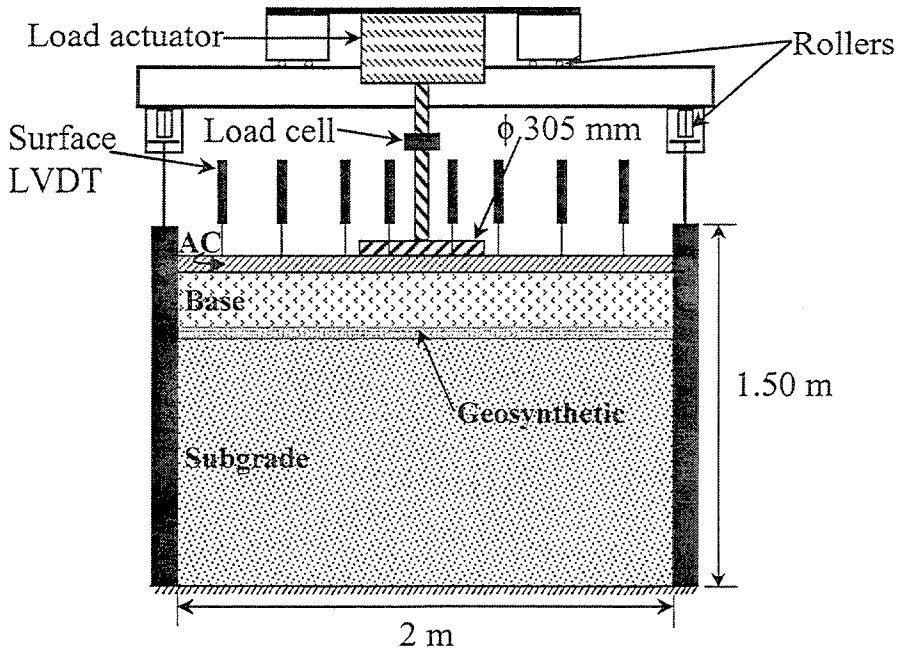

Figure 3.1.1 Schematic diagram of the pavement test facility.

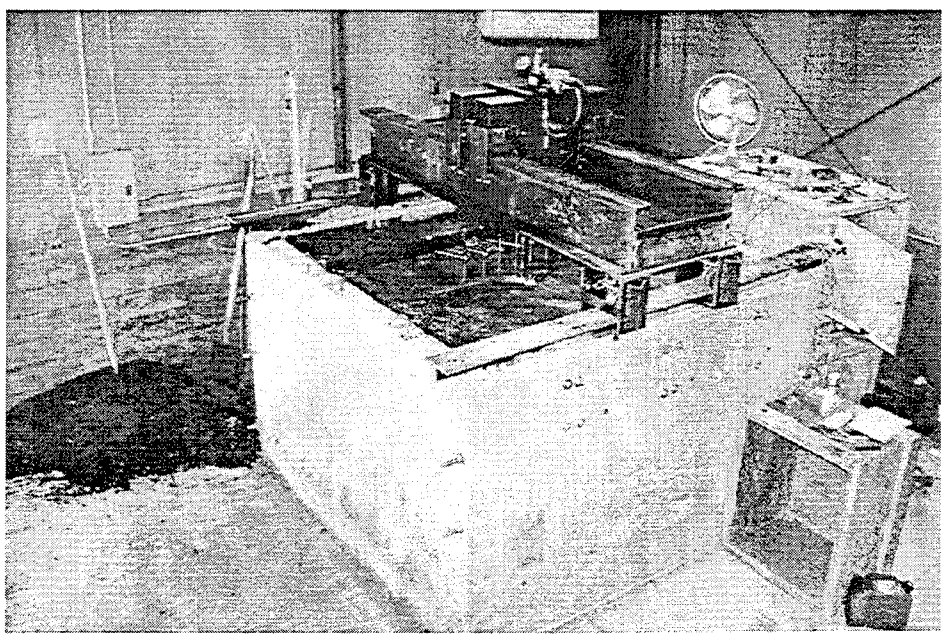

Figure 3.1.2 Image of the pavement test facility.

I-beams were set into two of the concrete walls during construction and serve as a base for the loading frame. The I-beams also allowed the load-frame to be moved such that the load could be applied at various locations across the pavement surface. The applicability of a movable load is discussed later in reference to the preliminary clay section.

A load frame was constructed to rest and ride on the I-beams set into the concrete walls. The frame consists of an additional two I-beams that span and react against the I-beams set into the concrete walls of the box. A load actuator, consisting of a pneumatic cylinder with a 305 mm diameter bore and a stroke of 75 mm, is placed between the two I-beams of the frame. A 50 mm diameter steel rod 300 mm in length extends from the piston of the actuator. The rod is rounded at its tip and fits into a cup welded on top of the load plate that rests on the pavement surface.

The load plate consists of a 305 mm diameter steel plate with a thickness of 25 mm. A 4 mm thick, waffled butyl-rubber pad was placed beneath the load plate in order to provide a uniform pressure and avoid stress concentrations along the plate's perimeter. Figure 3.1.3 shows an image of the load plate resting on the pavement surface.

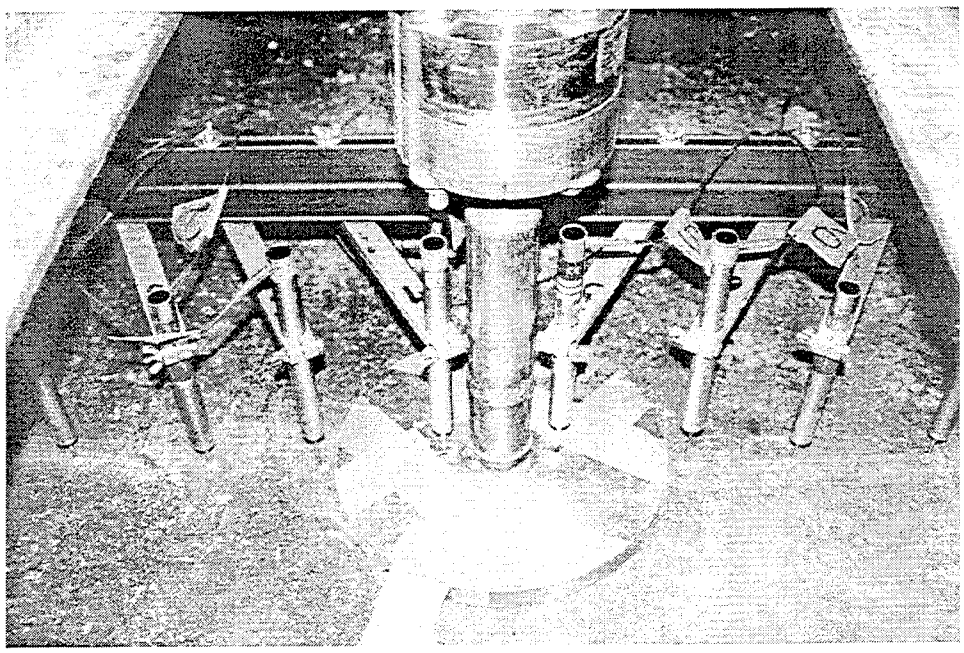

Figure 3.1.3 Image of the pavement load plate and surface instrumentation.

A binary solenoid regulator attached to a computer controlled the load-time history applied to the plate. The software controlling the solenoid was the same software used to collect data from the instruments contained in the pavement sections and is described in later in Section 3. The software was set up to provide the load, or plate pressure pulse shown in Figure 3.1.4. This pulse has a linear load increase from zero to 40 kN over a 0.3 second rise time, followed by a 0.2 second period where the load is held constant, followed by a load decrease to zero over a 0.3

second period and finally followed by a 0.5 second period of zero load before the load cycle is repeated, resulting in a load pulse frequency of 0.67 Hz. The maximum applied load of 40 kN resulted in a pavement pressure of 550 kPa. This load represents one-half of an axle load from an equivalent single axle load (ESAL). The load frequency was selected to allow the data acquisition system time to store data before the next load pulse was applied. The average peak plate pressure and standard deviation over the course of pavement loading is given in Section 3.5 for each test section reported. Also shown in Figure 3.1.4 is the corresponding output from the load cell for a typical load application. The hump seen on the descending branch of the curve is due to back venting of air pressure into the solenoid and was characteristic of all load pulses.

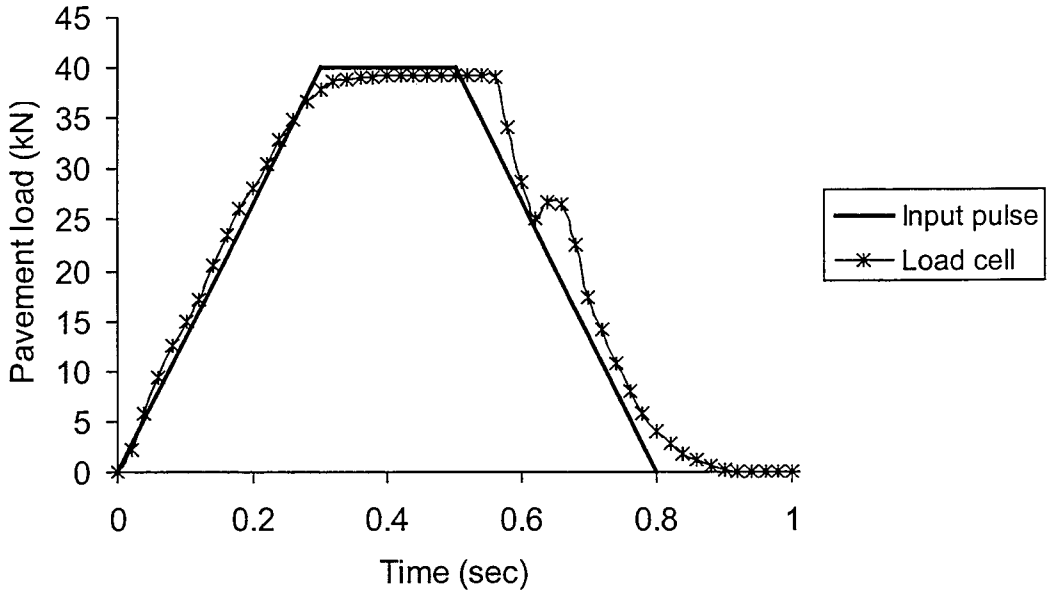

Figure 3.1.4 Input load pulse and corresponding load cell measurement.

3.2 Pavement Layer Materials

Contained in this section are descriptions of the pavement layer materials used to construct the test sections. As-constructed properties of the pavement layers are provided in Section 3.5.

3.2.1 Asphalt Concrete

Hot-mix asphalt concrete was used for clay subgrade sections (CS) 1-11, the preliminary clay subgrade section PCS1, and for the silty-sand subgrade sections (SSS) 1-4. The aggregate gradation meets the Montana Department of Transportation specifications for a Grade A mix design. Asphalt cement used was PG-58/28 and asphalt content was approximately six percent.

Cold-mix asphalt concrete (MC-800 asphalt cement) was used for sections labeled SSS5-SSS9. Cold-mix was used because of the unavailability of hot-mix during winter months. Sections using cold-mix are not used for comparison to sections with hot-mix. Grain size distributions for both the hot-mix and cold-mix are shown in Figure 3.2.1. As-constructed properties of the AC for each test section are given in Section 3.5.

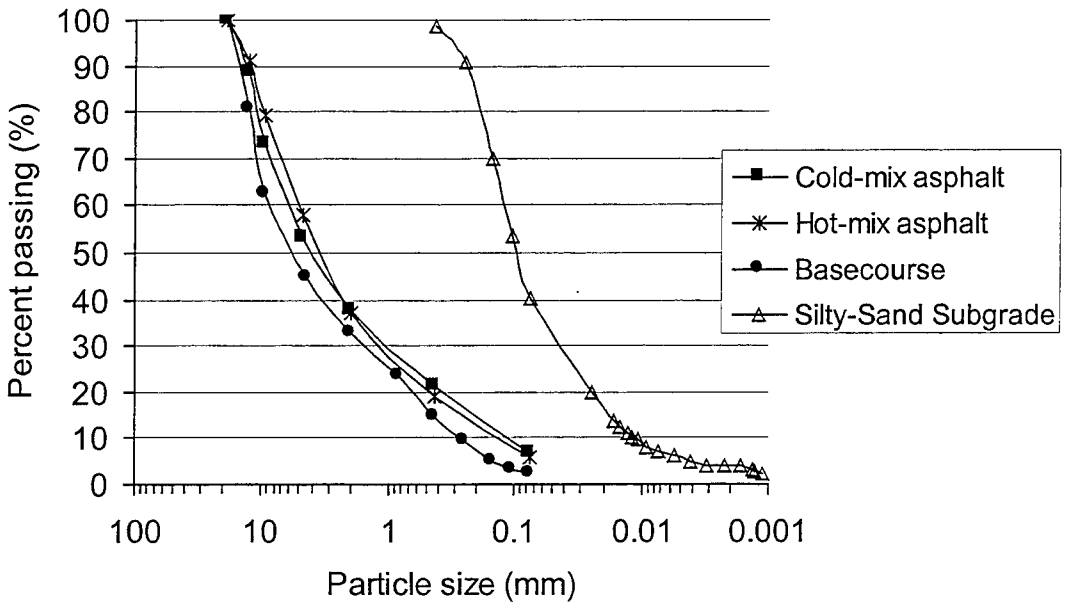

Figure 3.2.1 Grain size distribution of hot-mix aggregate, cold-mix aggregate, base course aggregate and silty sand subgrade.

3.2.2 Geosynthetics

Three geosynthetics were used in this study. A Tensar BX-1100 geogrid, a Tensar BX-1200 geogrid, and an Amoco 2006 woven geotextile were used for reinforced test sections. These products were chosen to provide a wide range of parameters thought to control reinforcement in this application. Differences in tensile properties between these materials are discussed later in this section. Differences in shear-interaction properties, as ascertained from pullout tests, for the different materials are also discussed later in this section. Table 3.2.1 provides material properties for the three geosynthetics used, where these properties are based on manufacturer's data as noted in the table. The reference names listed in this table are the names by which the materials are referred to in the remainder of this report.

Table 3.2.1 Geosynthetic material parameters.

	Geogrid: Tensar BX-1100	Geogrid: Tensar BX-1200	Geotextile: Amoco 2006
Reference Name	Geogrid A	Geogrid B	Geotextile
Material	Polypropylene	Polypropylene	Polypropylene
Structure	Punched Drawn, Biaxial	Punched Drawn, Biaxial	Woven
Mass/Unit Area (g/m^2)	215[1]	309[1]	250[3]
Aperature Size (mm)			
Machine Direction	25[1]	25[1]	None
Cross-Machine Direction	33[1]	33[1]	
Wide-Width Tensile Strength (at 5% Strain, kN/m)			
Machine Direction	9[1]	11[1]	10[3]
Cross-Machine Direction	13[1]	20[1]	22[3]
Ultimate Wide-Width Tensile Strength			
Machine Direction	13[1]	19[1]	31[2]
Cross-Machine Direction	20[1]	31[1]	31[2]

[1] (GFR, 1994)
[2] (GFR, 1997)
[3] (AMOCO, 1996)

An extensive series of uniaxial tension tests were performed on geogrid A and the geotextile. These tests included monotonic uniaxial tension tests at a fast and a slow strain rate, two series of cyclic uniaxial tension tests, and uniaxial tension creep tests. Figure 3.2.2 shows results of rapid loading uniaxial tension tests performed on geogrid A and the geotextile in their machine and cross-machine directions. The geogrid specimens were loaded to rupture. Loading was discontinued prior to rupture for the geotextile specimens due to limited capacity of the load-transfer device. The strain rate of loading ranged from 4 to 16 % strain per second. As can be seen from Figure 3.2.2, the tensile stiffness characteristics of geogrid A and the geotextile are comparable, with the geotextile stiffness properties bracketing that of geogrid A. Test results are not available for geogrid B, which is stiffer than geogrid A. Figure 3.2.2 also contains data from a test performed on geogrid A in a direction 45 degrees to the machine and cross-machine directions. This test was performed to assess the in-plane shear stiffness of the material. The test produced a maximum load of 0.8 kN/m. A similar test performed on the geotextile showed that essentially no load could be carried by the material in this direction.

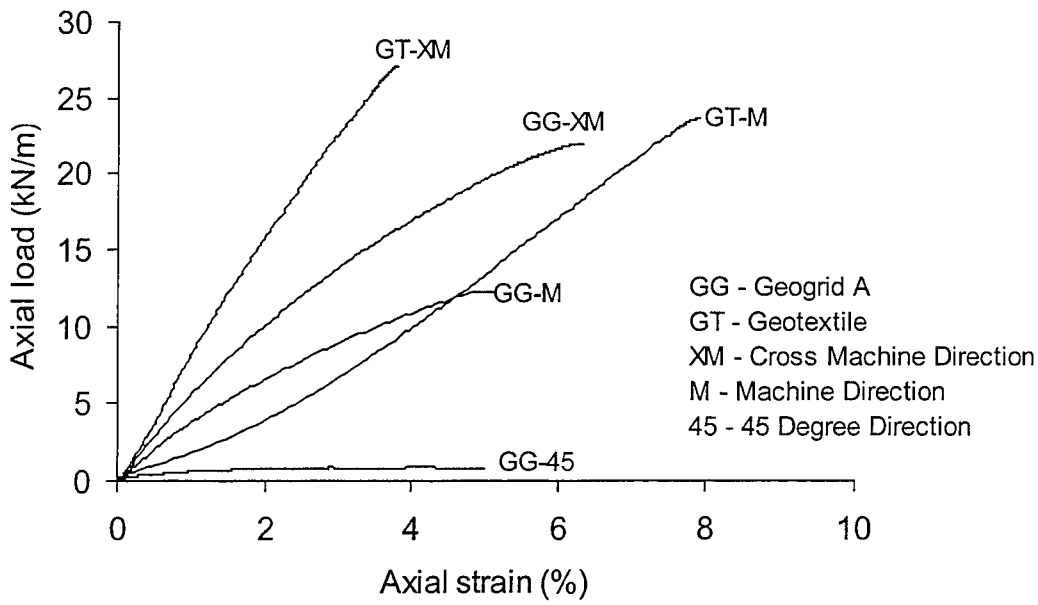

Figure 3.2.2 Rapid loading uniaxial tension test results on geogrid A and the geotextile.

Figure 3.2.3 shows results from similar tests performed at a slow loading rate corresponding to an axial strain rate of 0.26 % strain per minute. Comparison of Figures 3.2.2 and 3.2.3 shows that creep takes place in these materials with creep appearing to be more significant for geogrid A.

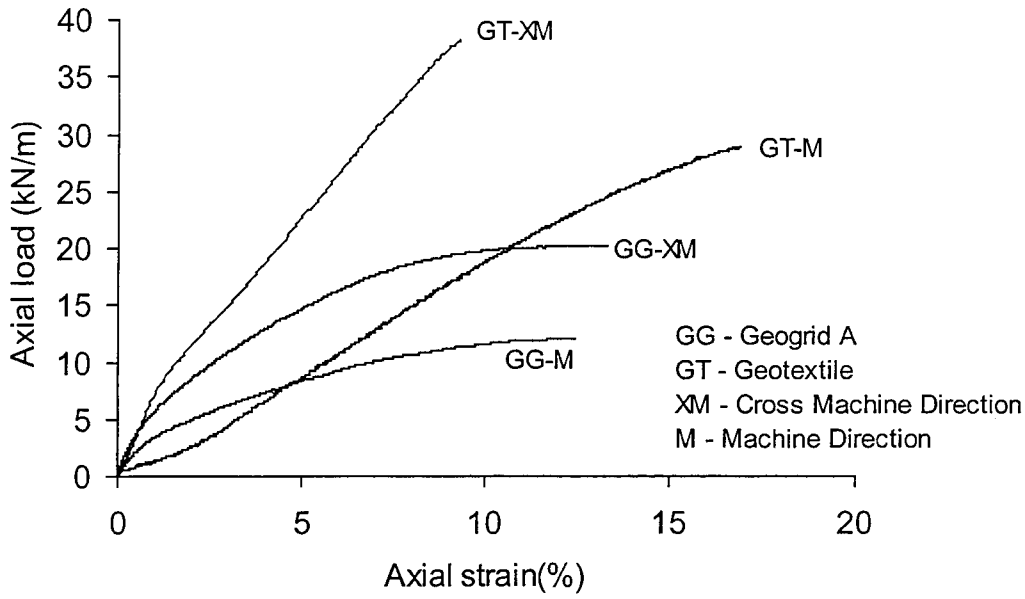

Figure 3.2.3 Slow loading uniaxial tension test results on geogrid A and the geotextile.

Figure 3.2.4 shows results from cyclic uniaxial tension tests performed on geogrid A and the geotextile in the machine and cross-machine directions. These tests were performed by applying a constant axial load for a certain number of cycles, followed by the application of a greater load for another number of load cycles, with this process repeated for 14 increasing load levels. The loads applied to the geotextile were, on the average, slightly less than those applied to the geogrid. The permanent axial strain measured between load cycles is plotted against load cycle in Figure 3.2.4. The results illustrate that slightly more strain is developed in the geotextile for lower load cycle numbers where the load level was lower. For higher loads, more strain develops in the geogrid, which is consistent with findings seen in Figure 3.2.3 that show that the geogrid tends to exhibit greater creep strains. Uniaxial tension creep tests have also shown this.

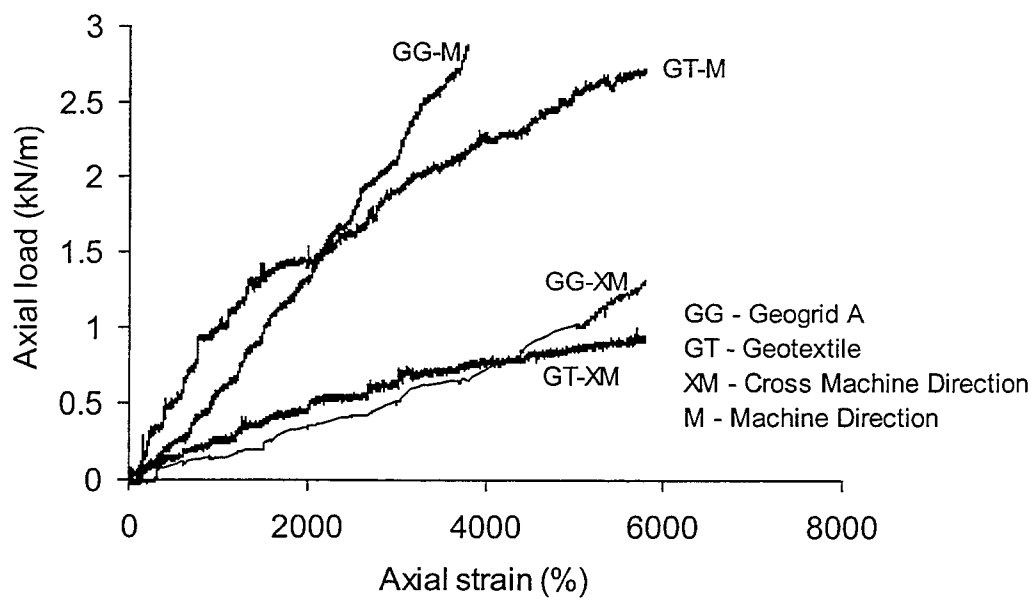

Figure 3.2.4 Cyclic loading uniaxial tension test results on geogrid A and the geotextile.

Pullout tests were conducted on geogrid A and the geotextile where these materials were embedded in the base course aggregate. A pullout box, described by Cuelho (1998), having inside dimensions of 1100 mm high, 900 mm wide and 1250 mm long, was used to conduct pullout tests at normal stress confinement levels of 5, 15 and 35 kPa. A numerical solution was formulated to describe the shear-interaction that occurs between the geosynthetics and the base aggregate. This solution accounts for the nonlinear stress-strain behavior of the geosynthetics and the mobilization of shearing resistance along the length of the geosynthetic. A nonlinear

shear stress – shear displacement relationship for the elemental interaction between geosynthetic and base aggregate was used in the solution. This relationship incorporates a shear stiffness, a peak friction angle and a residual friction angle. The shear stiffness describes the initial slope of the shear stress versus shear displacement curve. The peak friction angle describes the relationship between shear stress and normal stress for the peak strength condition. The residual friction angle describes the same parameter for large levels of shear displacement. These parameters are important in describing the shear interaction and relative slip that occurs between the geosynthetics and the base aggregate when load is applied that induces lateral movement of the base aggregate.

Figures 3.2.5 and 3.2.6 show strength envelopes for peak and residual strength for geogrid A and the geotextile. For geogrid A, peak friction angles of 54° and 58° were obtained when material was pulled in the machine and cross-machine directions, respectively. Residual friction angles of 52° and 56° in the machine and cross-machine directions, respectively, were obtained for geogrid A. For the geotextile, no difference between peak and residual friction angles were observed, with values ranging between 40° to 53° in the machine direction and 37° to 48° in the cross-machine direction. Values of shear stiffness for geogrid A and the geotextile are shown in Figure 3.2.7, where it is seen that a constant value of 200 MN/m^3 was obtained for geogrid A and values ranging from 30-100 MN/m^3 were obtained for the geotextile.

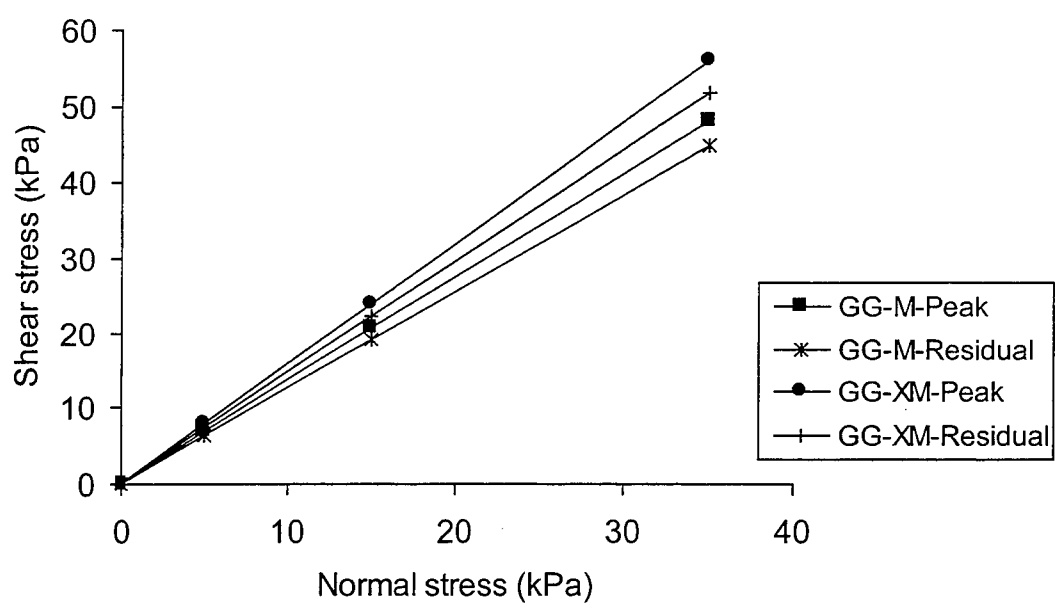

Figure 3.2.5 Shear stress versus normal stress for geogrid A – base aggregate interaction.

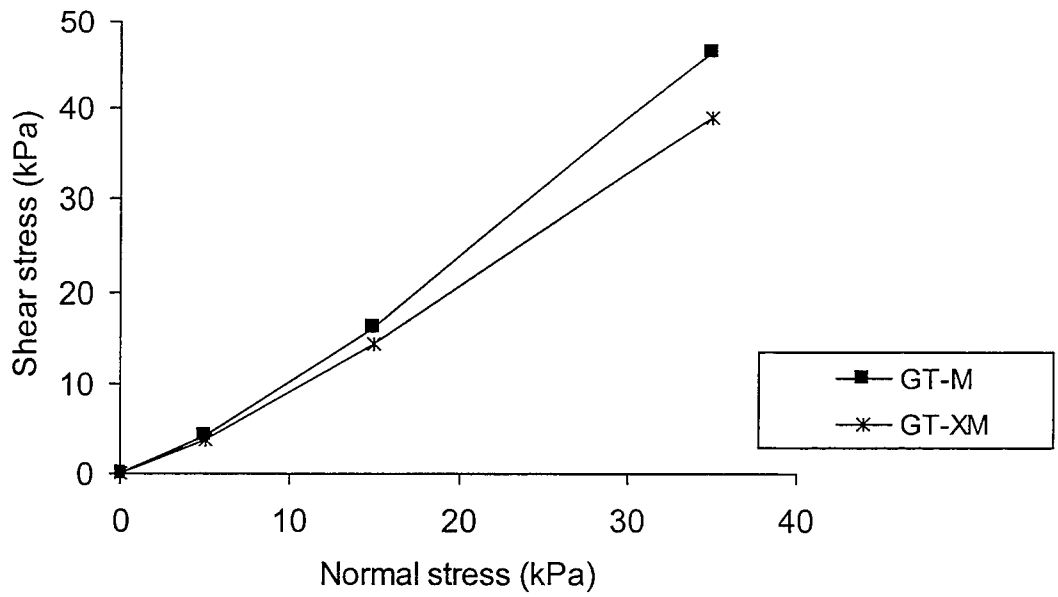

Figure 3.2.6 Shear stress versus normal stress for geotextile – base aggregate interaction.

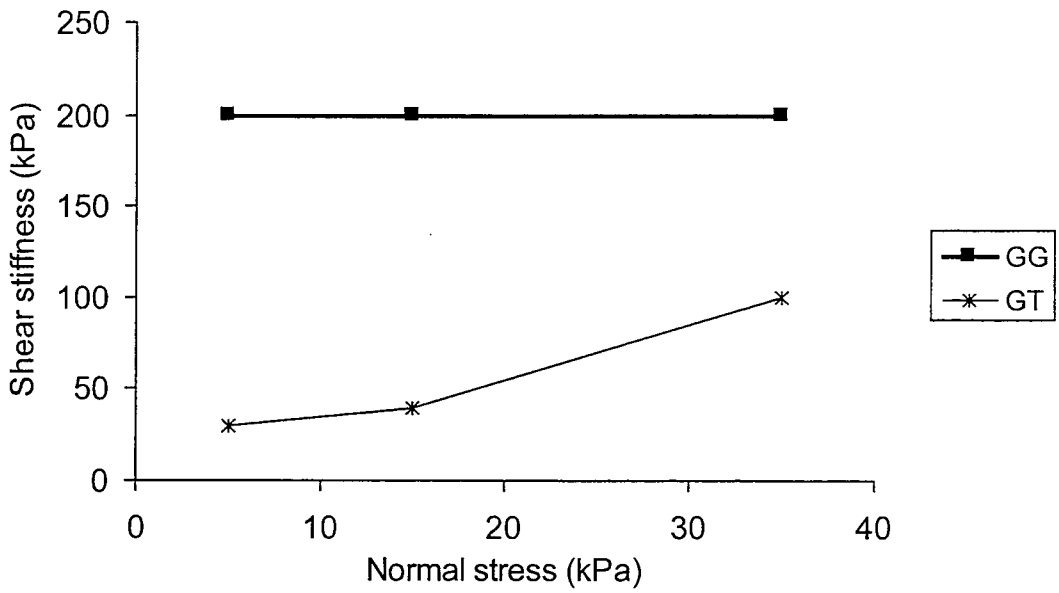

Figure 3.2.7 Shear modulus versus normal stress for geosynthetic – base aggregate interaction.

3.2.3 Base Course Aggregate

A crushed-stone base course meeting the Montana Department of Transportation specifications for Type A, grade 3 was used for all experimental test sections. The base course grain size distribution is shown in Figure 3.2.1, where it is seen that 100 % passes the 19 mm

sieve. The material is classified as an A-1-a or a GW. Specific gravity of the material is 2.63. Modified Proctor tests resulted in a maximum dry unit weight of 21.5 kN/m^3 at an optimum moisture content of 7.2 %. This material was typically compacted at a water content of 6.3 % and to a dry unit weight of 21 kN/m^3. As-constructed properties of the base course for each test section is given in Section 3.5.

Figures 3.2.8 and 3.2.9 provide results from consolidated-undrained (CU) triaxial test results performed on the base aggregate. CU tests were performed for purposes of calibrating a specific constitutive model for this material. These tests were performed at overconsolidation ratios (OCR) of 1, 2 and 6. These values of OCR were achieved by increasing and then lowering cell pressure with drainage lines open prior to the start of the shearing phase of the test. A failure envelope is drawn through the results in Figure 3.2.9, yielding a friction angle of 47.6 degrees. In these figures, q is the deviator stress and p' is the mean effective stress, each given by:

$$q = \sigma_1 - \sigma_3$$

$$p' = \frac{1}{3}(\sigma_1' + 2\sigma_3')$$

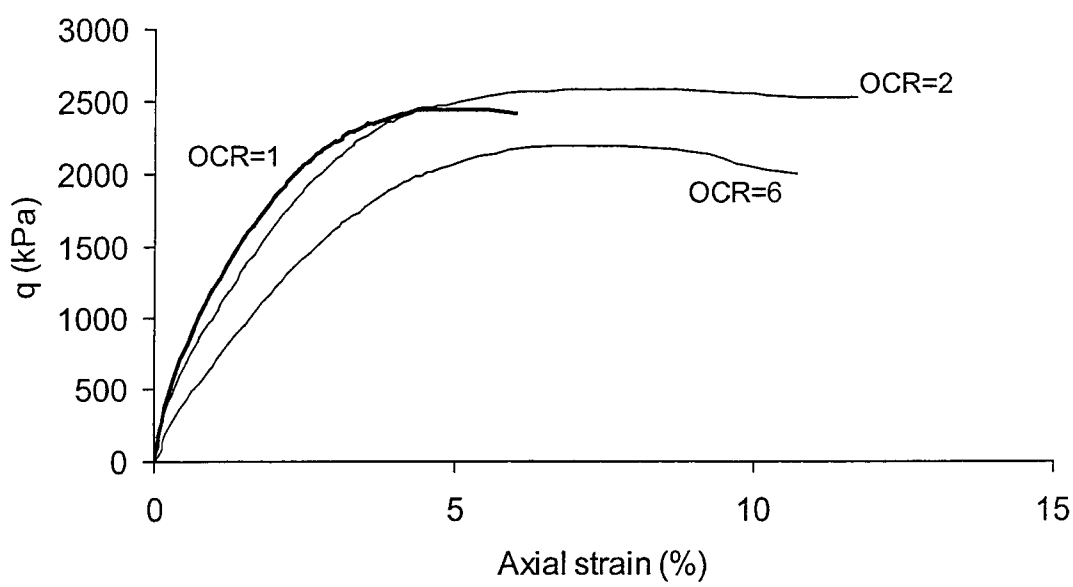

Figure 3.2.8 CU *q-axial strain* triaxial test results on the base aggregate.

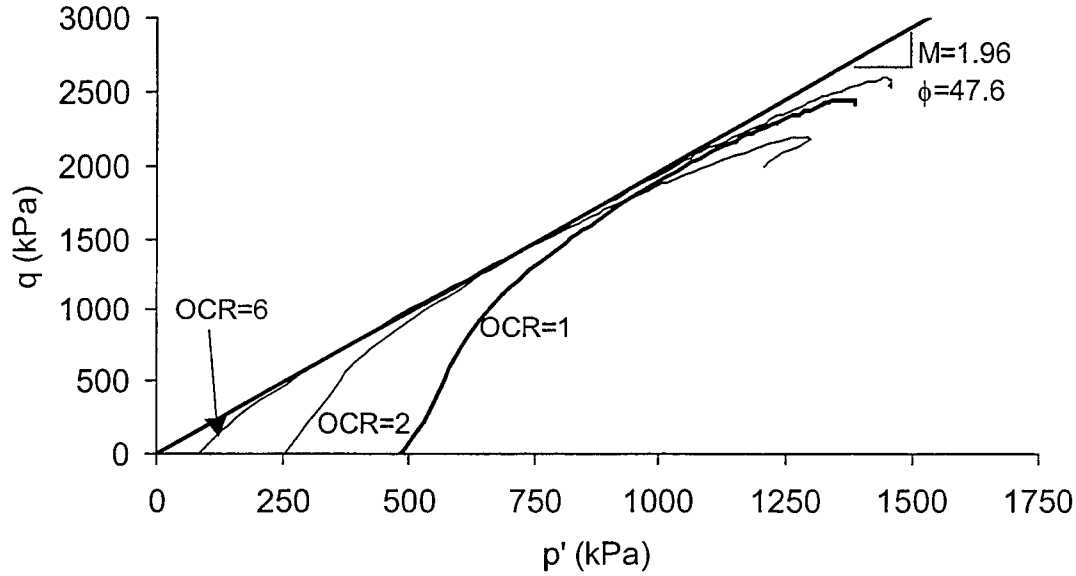

Figure 3.2.9 CU q- p' triaxial test results on the base aggregate.

3.2.4 Subgrades

To provide information on the influence of subgrade strength on reinforcement benefits, two subgrade materials were used in this study. A highly plastic clay subgrade was used to represent a "weak" subgrade while a silty-sand was used to represent a "strong" subgrade. The weaker subgrade consisted of a CH or A7-(6) clay, having a liquid limit of 100 % and a plastic limit of 40 %. 100 % of the clay material passes the #200 sieve. Specific gravity of the clay is 2.70. Modified Proctor compaction tests resulted in a maximum dry density of 16.0 kN/m^3 occurring at an optimum moisture content of 20.0 %. The clay was compacted at a water content of approximately 45 % in order to obtain a California bearing ratio (CBR) of 1.5.

The target water content of 45 % was established by conducting laboratory, unsoaked CBR tests. Figure 3.2.10 shows the variation of CBR with compaction water content. On this figure, it is noted that only a relatively small change in CBR results between a water content range of 43 to 46 %.

The stronger subgrade (approximate CBR=15 at a moisture content of 14%) consisted of fines trapped from the baghouse of a local batch hot-mix plant. The material is classified as a SM or A-4, with 40 % non-plastic fines and a liquid limit of 18 %. Specific gravity of the silty-sand is 2.68. Modified Proctor tests resulted in a maximum dry density of 18.2 kN/m^3 occurring

at a moisture content of 11.5 %. This material was typically compacted at a water content of 14.8 % and a dry unit weight of 17.5 kN/m^3. As constructed properties of the compacted silt subgrade in the test sections is given in Section 3.5.

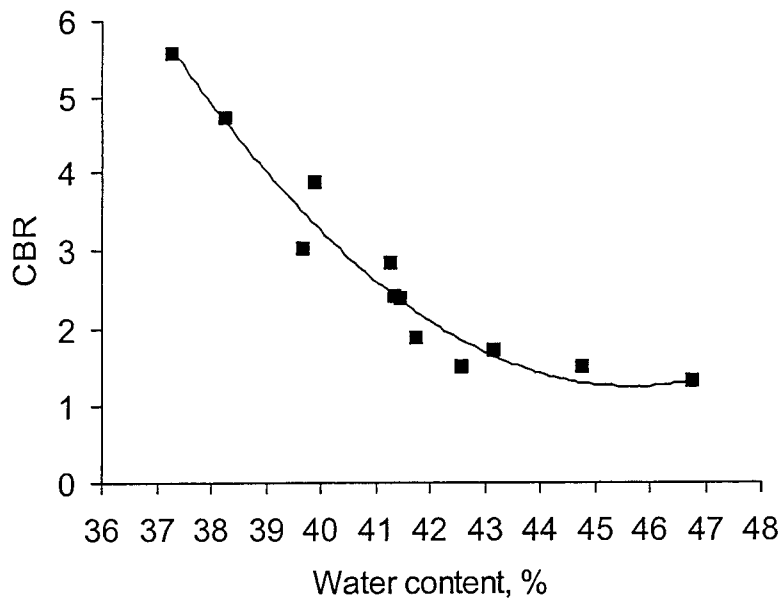

Figure 3.2.10 CBR versus compaction water content for the clay subgrade.

3.3 Instrumentation

An extensive array of instrumentation has been used in the test sections to quantify the mechanical response of the pavement materials to pavement loading and has aided in describing reinforcement mechanisms. The test sections contained as many as 90 instruments measuring applied pavement load, surface deflection, and stress, strain, temperature and moisture content in the various pavement layers. Instrumentation has been categorized into sensors measuring applied pavement load, asphalt surface deflection, tensile strain in the asphalt concrete, stress and strain in the base course and subgrade, strain on the geosynthetic, and general instrumentation measuring water content and temperature in the base and subgrade layers. Data acquisition software was configured to record information on the full time-history of response for prescribed load cycles and maximum and minimum sensor response for other load cycles. Additional details of the data acquisition system is given in Section 3.3.7

3.3.1 Pavement Surface Instrumentation

A load cell was placed between the rod emerging from the pneumatic actuator and the pavement load plate to measure applied pavement load. The load cell was manufactured by Sensotec (Columbus, OH) and had a range of 0-90 kN. The load cell can be seen attached to the load actuator rod in the upper portion of Figure 3.1.3. Eight Linear Variable Differential Transducers (LVDT) were used to monitor surface deformation of the asphalt concrete layer. These LVDT's can also be seen in Figure 3.1.3 and were manufactured by RDP Electronics (Pottstown, PA). Two different gages were used with ranges of 25 mm and 50 mm. The LVDT's with the greatest range were placed closest to the center of the load plate where the largest surface deformations occurred. The other gages were placed at increasing radii from the load centerline. The two LVDT's closest to the load plate centerline extended through the load plate and waffled rubber pad and rested on the pavement surface.

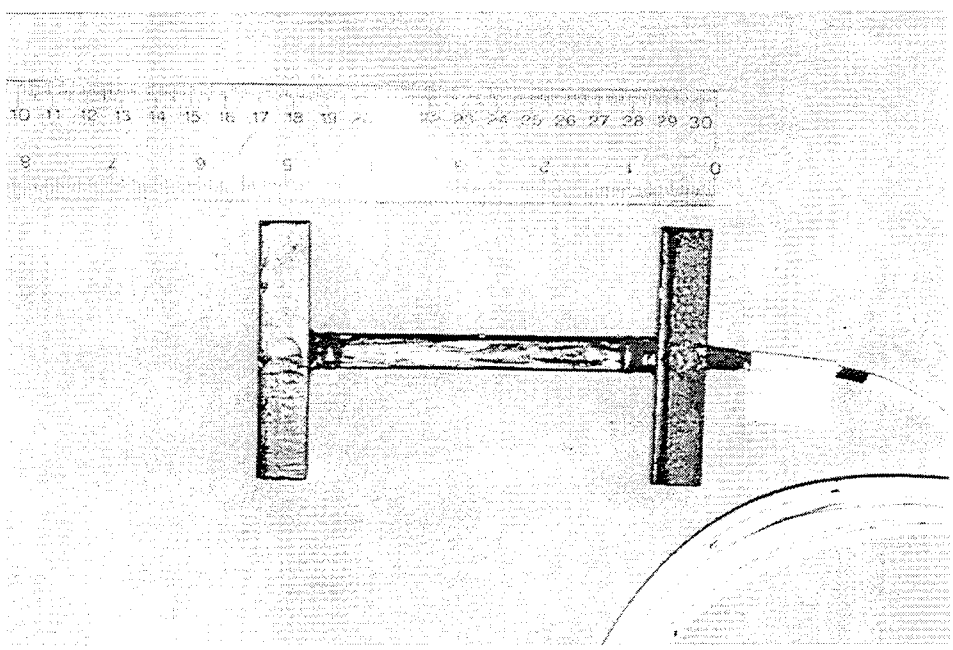

Figure 3.3.1 Asphalt concrete strain gage.

3.3.2 Asphalt Concrete Instrumentation

H-type, PAST (PAvement Strain Transducer) asphalt strain gages manufactured by Dynatest, Inc. (Ojai, CA), were used to measure tensile strain in the bottom of the asphalt concrete. The gages measure 135 mm in length and 70 mm in width and are shown in Figure

3.3.1. These gages have a range of approximately 0-1500 microstrain (0.15 %). The inside of the gage consists of a strain gage embedded in a strip of glass-fiber reinforced epoxy that has a high flexibility and relatively low strength. A multi-layer coating protects the gage from chemical effects. The average elastic modulus of the cell body is 2.2 MPa, resulting in a low "strain force" of 0.11 N/microstrain. This tends to limit the influence of the gage on the response of the surrounding material. Fatigue life is theoretically estimated at 1×10^6 cycles.

3.3.3 Geosynthetic Instrumentation

Foil strain gages were mounted to geogrid and geotextile samples in order to quantify in-situ strain behavior during pavement loading. Small, 18 mm long strain gages (Micromeasurements Group, Inc., Raleigh, NC, model EP-080500GB-120) were used for the geogrid specimens. These gages have a range of approximately 20 % strain, and a fatigue life of approximately 10,000 cycles under 0.1 % dynamic strain. Foil strain gages 110 mm in length (Micromeasurements Group, Inc., model EP-08-40CBY-120) were attached to geotextile specimens. These gages also have a range of approximately 20 % strain, but only 10 % of the range was active for greater sensitivity. Longer length gages were used for the geotextile to overcome problems with bonding of short gages to the irregular surface of the geotextile. Attachment of the foil strain gages to geosynthetic samples is briefly described in Section 3.4 while more details are available in Cuelho (1998).

3.3.4 Soil Stress Instrumentation

Stress cells (SOil Pressure Transducer, SOPT) marketed by Dynatest, Inc. (Ojai, CA) were placed in both the base course and the subgrade in order to quantify the dynamic stress behavior of the system. These cells have a diameter of 68 mm and a thickness of 13 mm. The cell utilizes a thin, 0.5 mm thick membrane that covers a layer of fluid. Fluid pressure is measured by a fully-bridged strain gage pressure transducer inside the cell. The cells are coated with epoxy and sand to insure proper bonding to soil materials. Fatigue life is listed at 3×10^6 cycles. Two types of stress cells were utilized in the test sections having different operating ranges. Type A stress cells were placed in both the base course and subgrade and had a range of 10-200 kPa. Type B stress cells having a maximum range of 800 kPa, were placed in a horizontal orientation to measure vertical stress in the base course directly beneath the load plate. The type B cells were

placed directly beneath the load because of higher pressures expected. A typical stress cell is shown in Figure 3.3.2. Performance and calibration of these cells have been discussed in Ullidtz et al. (1996), Askegaard et al. (1997) and Selig et al. (1997).

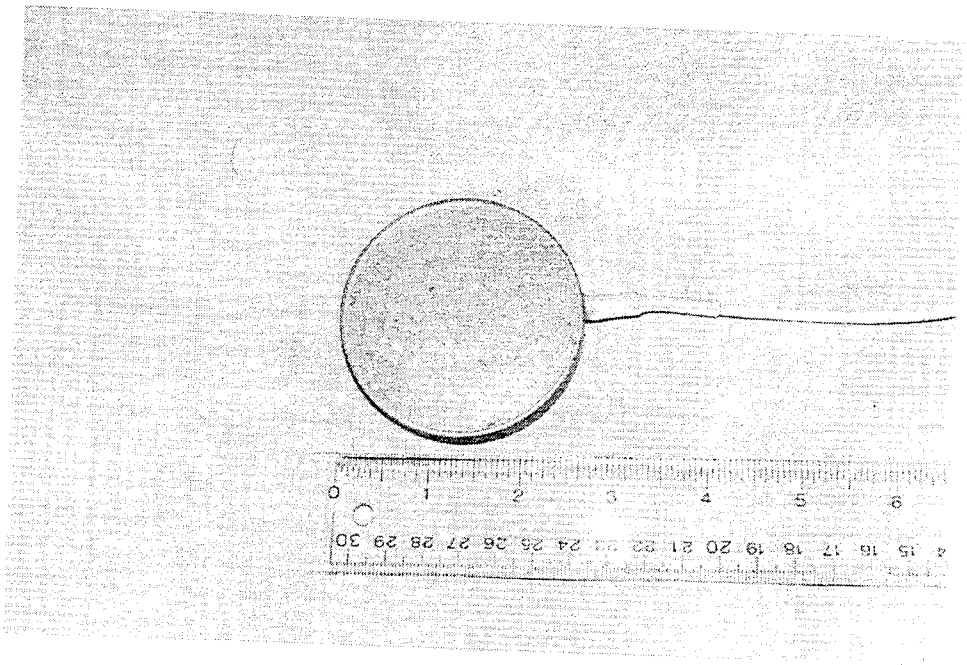

Figure 3.3.2 Typical soil stress cell.

3.3.5 Soil Strain Instrumentation

Soil strain was measured by alternating current (AC) LVDT's fitted with steel end plates measuring 50 mm x 15 mm x 5 mm in thickness. The LVDT's (model D5/400W) were obtained from RDP Electronics (Pottstown, PA). The gages have a nominal gage length of 70-80 mm, which corresponds to a 0.2-10 % strain range depending on the electronic amplification used for the sensor. A typical LVDT used in the test sections is shown in Figure 3.3.3.

3.3.6 Temperature and Moisture Instrumentation

Temperature probes from RDP Electronics (Pottstown, PA), were used in certain tests to record temperature in the base and subgrade layers for the purpose of correcting stress cell readings for minor temperature variations. The stress cells drifted by as much as 2-5 kPa with a temperature variation of 8.3 degrees Celsius. Time Domain Reflectometry (TDR) moisture content probes manufactured by Campbell Scientific (Logan, UT) were used in the subgrade to

monitor any changes in moisture content of the subgrade following construction and through pavement loading.

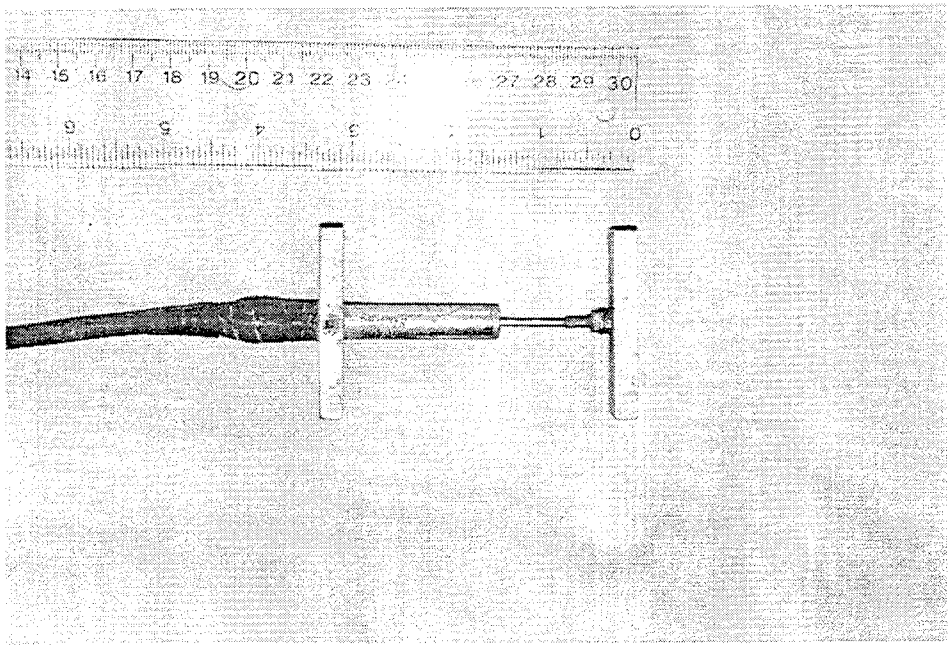

Figure 3.3.3 Typical soil strain cell.

3.3.7 Data Acquisition

The data acquisition system consisted of several groups of amplifiers (RDP Electronics model 611) connected to a laptop computer running Labview Software marketed by National Instruments (Austin, TX). Instruments were connected to amplifiers, which supplied excitation voltage to the sensors through 7-pin DIN connectors. Return signals from instruments were amplified and sent to the software program. The software saved the full time-history sensor response for prescribed load cycles where a sampling frequency of 50 Hz was used (which is 80 times faster than the frequency of loading), along with maximum and minimum sensor responses for a larger number of load cycles. Labview also allowed for specification of the load pulse shape discussed earlier in Section 3.1. The software provided onscreen, real-time viewing of data generated by any of the instruments in a test section. As many as four instruments could be viewed at any one time on the screen. A typical view of the amplifiers and the Labview on-screen display and real-time graphics is shown in Figure 3.3.4.

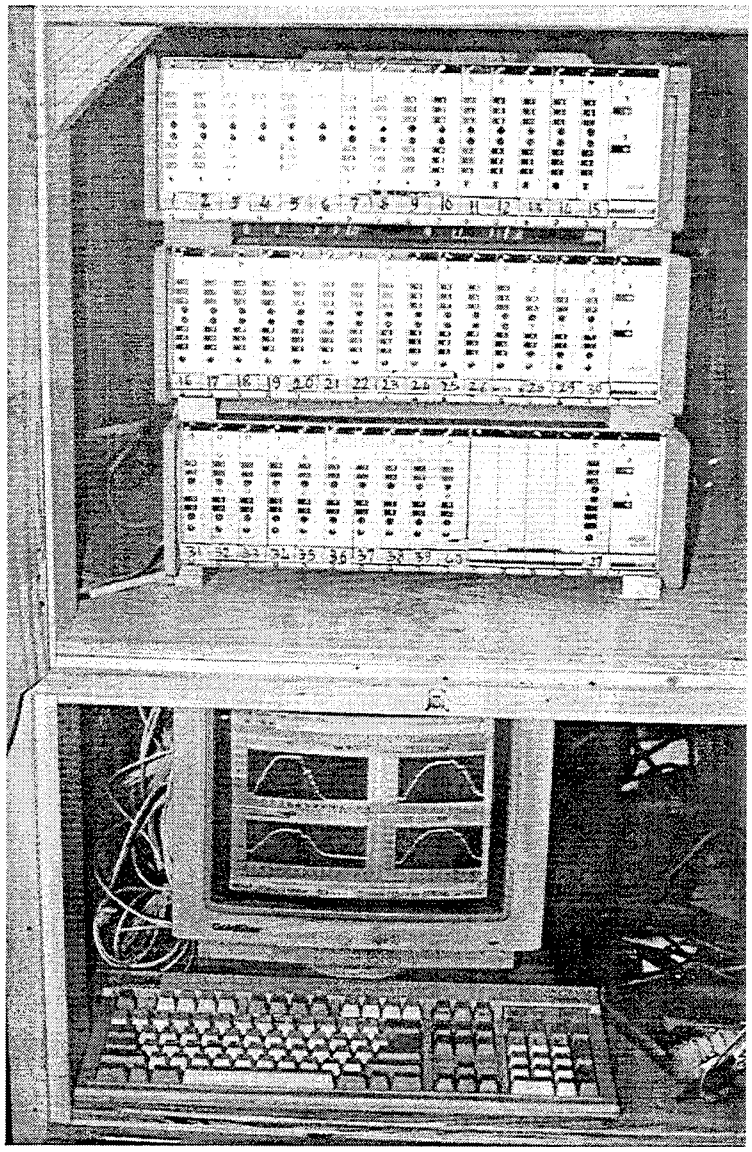

Figure 3.3.4 Data acquisition system and real-time graphics.

3.4 Test Section Construction

Table 3.4.1 provides information on the types and names of the test sections constructed. Variables included in the test sections listed below are: subgrade type, geosynthetic type, geosynthetic placement position in the base layer, and base course thickness. As-constructed values of layer thickness are provided in Section 3.5. A CS4 test section was constructed and loaded and contained two layers of geogrid A at the bottom and at 100 mm above the base-

subgrade interface. The performance of this section was very poor. Additional time and resources were not available to return to this configuration to examine if this behavior was valid or if construction variables were responsible for the poor behavior. For this reason, results from this test section are not reported herein.

Table 3.4.1 Constructed test section variables.

Section [a]	Subgrade Type	Geosynthetic	Position
PCS1[c]	Clay	Control	N/A
CS1[c]	Clay	Geogrid A	Base/subgrade interface
CS2[c]	Clay	Control	N/A
CS3[c]	Clay	Geogrid A	100 mm above base/subgrade interface
CS5[c]	Clay	Geogrid B	Base/subgrade interface
CS6[c]	Clay	Geotextile	Base/subgrade interface
CS7[c]	Clay	Geogrid A	100 mm above base/subgrade interface
CS8[c]	Clay	Control	N/A
CS9[d]	Clay	Control	N/A
CS10[d]	Clay	Geogrid A	Base/subgrade interface
CS11[c]	Clay	Geogrid A	Base/subgrade interface
SSS1[b]	Silty-sand	Control	N/A
SSS2[b]	Silty-sand	Geogrid A	40 mm above base/subgrade interface
SSS3[b]	Silty-sand	Geotextile	40 mm above base/subgrade interface
SSS4[b]	Silty-sand	Control	N/A
SSS5[b]	Silty-sand	Geogrid A	Base/subgrade interface
SSS6[b]	Silty-sand	Control	N/A
SSS7[b]	Silty-sand	Control	N/A
SSS8[b]	Silty-sand	Geotextile	Base/subgrade interface
SSS9[b]	Silty-sand	Geogrid A	Base/subgrade interface

[a] Nominal AC thickness = 75 mm for all sections.
[b] Nominal base course thickness = 200 mm.
[c] Nominal base course thickness = 300 mm.
[d] Nominal base course thickness = 375 mm.
N/A = Not applicable

3.4.1 Pavement Material Placement

The clay subgrades were constructed in approximately ten 75 mm lifts and compacted with a gasoline powered "jumping jack" trench compactor. The lift thickness of 75 mm was determined through trial and error so as to yield a uniform density in the layer without large void spaces. Thickness was measured with a standard auto-level and Philadelphia rod. The clay material was mixed to a target water content of 45 % with a skid-steer loader. Numerous water

content measurements were taken during mixing until the target water content was reached. Once a lift was compacted, approximately 4 samples were taken for oven drying to determine in-place moisture content. Five density measurements were taken for each lift with a Troxler model 3411-B nuclear densometer and verified occasionally by sand-cone tests. Dry density was calculated from the oven dried moisture content and the measured total density. Values of water content and dry density reported in Section 3.5 are an average of values collected for the entire subgrade (i.e. approximately 40 water content samples and 50 density measurements). Water content and density measurements were also made during excavation of the test section to verify that only minor changes took place during loading for material outside the influence of the applied load.

The silty-sand subgrades were constructed in approximately ten 100 mm lifts and measured with a standard auto-level and Philadelphia rod. The silty sand was mixed to a target water content of 14.8 % using the equipment described above. A vibratory plate compactor was used to compact each lift. Approximately two to three passes with the compactor yielded the desired density. Densities were measured as above with a nuclear densometer and verified for the first test section by sand-cone tests. Sections SSS1-4 used subgrades that had been placed in the manner described above. Sections SSS5-9 involved removing and replacing only the base, geosynthetic and AC layers. Hence, the subgrade was reused starting from section SSS4. The subgrades of sections SSS5-9 were not excavated and reconstructed due to time limitations.

For both subgrades a dynamic cone penetrometer was used for determination and validation of the target subgrade strength. The subgrade CBR was determined from the dynamic penetration index (DPI) using the correlation from MnRoad (1993). Shelby tubes were also pushed into the subgrades during excavation of the test section. These samples were used for triaxial compression experiments.

The base course material was also mixed with the skid steer loader to a target water content of 6.2 % and placed in 100 mm lifts. For the SSS series tests, the base course was placed in two lifts, and was placed in three to four lifts for the CS series tests. Compaction was achieved with a vibratory plate compactor. Compacted water content was measured by collecting samples and oven-drying these samples. Densities were taken with a nuclear densometer and verified with sand-cone tests. Water content and density was also measured during excavation of the test section. Layer surfaces were roughened with a rake prior to a subsequent lift placement or prior to geosynthetic placement in order to provide layer bonding.

The asphalt concrete layer was placed in two lifts corresponding to a total thickness of 75 mm and compacted with a vibratory plate compactor. Hot-mix was typically placed at 250 degrees Fahrenheit. The hot-mix was delivered via truck from a local batch plant in approximately 2700 kg (3-ton) loads. Mix in excess of that needed for the test section was ordered in order for the batch to remain hot while placement occurred. In-place density was measured with a nuclear gage and later from drilled cores. These cores were taken from outside the loaded area after loading was completed. The asphalt layer was allowed to cure for one day prior to loading.

3.4.2 Instrument Placement

When construction reached the point where instruments were to be installed, the soil was excavated immediately surrounding the area of the instrument, to the proposed level with a hand trowel and the instrument placed. To facilitate location of sensors, a template was used for each level of sensors placed in the section. Use of the template allowed precise placement of the sensors from layer to layer, and kept the center point of the box constant throughout all tests. The template had small holes drilled at the locations of the instruments whereby small nails were pushed through into the soil below. The template was then removed and a chalk line was snapped for X and Y coordinates. Perpendicular lines were then snapped at each instrument location.

For the vertically oriented LVDT's measuring vertical strain, round holes approximately 65 mm in diameter were excavated with a small hand trowel to a predetermined depth which was then verified with the auto-level. The LVDT was placed vertically into the hole and small amounts of soil were dumped and compacted with a metal rod around the instrument. Near the top of the hole, the core of the LVDT was adjusted up or down and voltage monitored, so as to provide for sufficient travel during the test. Voltages were monitored via a voltmeter during instrument installation. Instruments were then covered and the surface soil was hand compacted.

Horizontal LVDT's measuring radial and tangential strain were placed in the same way except that a small level approximately 25 mm by 10 mm was used to level the instrument before compacting around the instrument. The core of the LVDT was initially placed to be in the middle of its range. Compaction then proceeded by hand up to the top of the soil surface. Gains

(electronic amplification of the LVDT signal) were set to give a range appropriate for the sensor location in the section.

Stress cells were placed in the same way as the LVDT's with the use of a template. Holes approximately 80 mm in diameter were excavated to a predetermined depth, and were measured with the auto-level. For stress cells measuring vertical stress in the subgrade, the bottom of the hole was flattened with a 75 mm diameter "puck" the same size as the stress cell. This flattening of the bottom of the hole provided a level base for the stress cell. The stress cell was then placed into the hole with the active face in the upward position and the small bubble level was placed on the instrument. The instrument was adjusted until level and soil backfilled and compacted in small increments over the sensor. Stress cells measuring radial and tangential stresses were placed in the same manner except for their orientation.

Stress cells placed in the base course used a 4-5 mm layer of sand placed on either side of the instrument to eliminate stress concentrations caused by large gravel particles. For stress cells measuring vertical stress, the sand was pluviated onto the active face of the cell after leveling to the desired thickness and backfilled as described previously. Stress cells measuring radial and tangential stresses were placed in a vertical orientation in the excavated hole. Two pieces of cardboard equal to the size of the instrument were placed on the active and passive faces of the cell. Soil was compacted around the cell/cardboard configuration until the top of the stress cell was just visible. The two cardboard pieces were then removed leaving a 3-4 mm thick void around the cell. This void was filled with fine sand to prevent inclusion of large rock particles from the base course from damaging the active face of the stress cell. Compaction then proceeded above the instrument. Wires from all instruments were placed in 25 mm deep channels and routed out of the box to the data acquisition system to prevent disruption from compaction of subsequent lifts by the vibratory plate and "jumping-jack" compactors.

Foil strain gages were installed on both the geogrid and geotextile samples. Two gages were installed on opposite sides of the geosynthetic at the same measurement location in a ½ Wheatstone Bridge configuration. This configuration provided temperature compensation and reduced errors in strain readings due to bending of the geosynthetic. Foil gage preparation and attachment procedures for geogrid and geotextile samples have been given in Cuelho (1998). Included in Cuelho (1998) is a description of the environmental protection used for geotextile and geogrid specimens placed in the soil.

For geosynthetic materials placed within the base course layer, a small amount of fine sand was placed beneath each gage before the geosynthetic was installed. The geosynthetic was then installed and a small amount of sand was placed over each gage for protection from large particles. Gravel was then spread by hand over the geosynthetic starting at the center of the box and proceeding outward toward the edges of the test box. Placement of the gravel in this way allowed the geosynthetic to be placed without slack or folds. The gravel was then compacted over the top of the geosynthetic with the vibratory plate compactor. Readings of each foil gage were taken with each subsequent lift placement of base course in order to determine if compaction-induced strains were significant. Placement strains varied, but usually showed the geosynthetic to be in tension by strain values ranging from 0.002-0.01 %. Strains of this magnitude were much smaller than the strains observed during loading, which were on the order of 0.1-3.0 %. Installation of the geotextile or geogrid at the base course/subgrade interface proceeded in the same manner as for placement inside the base course, except that the fine sand was only added on top of the geosynthetic gages.

Asphalt strain gages were placed 5-10 mm from the bottom of the asphalt concrete in order to observe tensile strains. A thin layer (5-10 mm) of asphalt concrete was placed in the desired location of the sensor. All particles larger than the #4 sieve were removed and the layer was compacted using a rubber mallet. The gage was then placed on top of the material, leveled, and more AC was added around the gage. Again, large particles were removed in the vicinity of the gage. Compaction proceeded over the top of the instrument. Asphalt concrete was placed around the instrument and compacted with the vibratory plate compactor.

Eight LVDT's, measuring surface deflection of the asphalt, were placed in a rigid frame separate from the loading apparatus. Roofing nails were driven into the asphalt while it was still warm for the tips of the LVDT's to rest on. Two instruments were placed through 5 mm diameter holes drilled through the load plate and waffled rubber pad to measure deflection directly under the plate. Three instruments were spaced on either side of the plate, with the array of instruments spanning approximately one meter.

3.4.3 Instrument Locations

Instruments were located in the test sections where stresses and strains were thought to be most critical. Locations identified as critical to describing reinforcement mechanisms and

benefits were: 1) areas directly beneath and in the vicinity of the load plate, 2) locations on and near the geosynthetic, 3) the bottom of the AC layer, and 4) the top of the subgrade. Instruments were also placed to provide a description of a response parameter for a given layer with radial distance from the load centerline. Tables of instrument locations for the test sections contained in this report are given in Appendix A. Tables for sections CS1 and CS3 are not presented since this data was not used in this report for reasons described in Section 3.5 (pg. 46). Tables for sections SSS6-9 are not included due to the limited data used from these sections.

Generally, the instruments were concentrated in the base layer and in the top 100 mm of the subgrade. Stress and strain instruments were placed to provide measurements in vertical, radial, and tangential directions at varying radii from the load centerline. Several instruments measuring the same parameter were placed at varying radial distances from the load centerline in order to provide a description of how this parameter varied with radial distance. For instance, three to four vertical LVDT's (measuring vertical strain, ε_v) were placed at a given depth in the base to provide a profile of vertical strain versus radial distance. The same was done for soil strain cells measuring radial and tangential strain, and stress cells measuring vertical, radial and tangential stress. Foil gages were located on the geosynthetic specimens in both the machine and cross-machine directions to provide measurements of radial and circumferential strain. Figure 3.4.1 illustrates the direction and types of measurements for an elemental volume of soil inside a test section. This figure is not meant to imply that all six measures were made at the same point since only a single sensor could be placed at any one location.

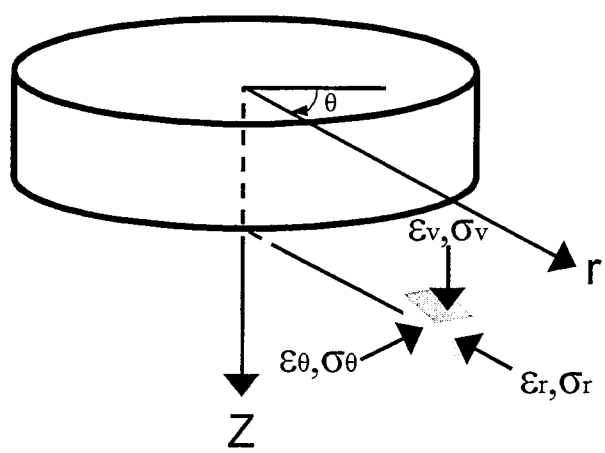

Figure 3.4.1 Theoretical stress and strain measurements for an element of soil inside a test section.

In addition to the two levels of instruments mentioned previously, AC strain gages were installed to measure radial and tangential strain in the bottom of the AC. Additionally, three levels of stress and soil strain cells measuring vertical stress and strain were installed directly beneath the load center at increasing depths in the subgrade.

The placement of instruments in the preliminary clay subgrade section (PCS1) was different from the other clay and silty-sand subgrade sections. Orientation of the instruments was such that on average, two instruments were placed in each layer (mainly the base and the top of the subgrade) measuring the same parameter. Two instruments were placed in each level measuring vertical, radial and tangential stress and strain. Additionally, measurements of vertical stress and strain were made deeper in the subgrade in the center of the box.

3.4.4 Instrument Calibration

Instruments that required calibration included the LVDT's used for surface deformations and for the soil strain cells, and the temperature probes. The stress cells and H-type asphalt concrete strain gages were calibrated by Dynatest at the factory. The LVDT's were calibrated before each test was conducted with minor changes in the calibration factors occurring between tests. To calculate strain from the soil strain cells, a gage length for the LVDT was defined as the inside distance between the end plates when the sensor was placed in the soil. Strain was defined as the change in length between the two end plates divided by the original gage length.

3.5 As-Constructed Pavement Layer Properties

The variables included in the 21 test sections constructed were listed in Table 3.4.1 in Section 3.4. The quality control measures taken to provide information on the consistency of the pavement layer materials between test sections was outlined in Section 3.4.1. These measures included measurement of in situ water content and dry density in the subgrade and base course layers during construction and during excavation, DCP tests on the compacted subgrade during construction and during excavation, measurement of in-place density of the compacted AC, and measurement of in-place density of the AC from 100 mm and 150 mm diameter AC drill cores. Additional tests were performed on both bulk AC samples and the 100 mm diameter cores. These tests included determination of asphalt cement content, air voids, rice specific gravity, Marshall stability, penetration and kinematic viscosity. At the time of this report, creep tests

were being performed to define viscoelastic material properties of the AC. Consolidated-Undrained triaxial compression tests were also being performed at the time of this report on undisturbed samples of the clay and silty-sand subgrade obtained by pushing shelby tubes into these materials during excavation. In addition to reporting results from the quality control measures reported above, a statistical analysis of these measures is provided in this section. This analysis is performed for the purpose of illustrating which sections can be directly compared and if differences exist, what resulting impact on comparisons of pavement performance is expected.

As-constructed asphalt concrete properties for all test sections are given in Table 3.5.1. The number of samples used for the determination of each measure is given in parentheses. The coefficient of variation (CV) of the measure from the samples used is listed for the properties of thickness, density, and air voids content, where CV is defined as the measure of dispersion relative to the central value (i.e. standard deviation divided by the mean). In addition to examining the CV for a particular parameter measured in a given test section, a statistical comparison of the average values of different parameters between groups of test sections was made. This has been done for the purpose of establishing whether statistically significant differences in these parameters exist between test section groups, which would lead to differences in pavement performance that would need to be accounted for when making comparisons of performance between sections. The AC properties that were examined in this analysis include thickness, density and air voids. The test section groups for which comparisons were made included CS1-CS11 and SSS1-SSS4.

To establish whether statistically significant differences exist between the parameters of thickness, density and air voids within the two test section groups described above, an analysis of variance (ANOVA) was performed (Peterson, 1985). This analysis involved testing the null hypothesis, which states that the mean of a variable (i.e. thickness, density or air voids) within a given test section was equal to all other test section means. Failure of the null hypothesis implies that differences in the variable exists between test sections. The analysis assumes a normal distribution of the means of the test sections and a normal distribution of the random error associated with each sample within each test section. The analysis uses a ratio of variances to determine whether differences between test sections are significant. This ratio is calculated as the mean square of all means divided by the mean square for error. The importance of this ratio is determined by a comparison with the standard F distribution. The significance of the ratio was

quantified as the probability of obtaining a larger value from the standard F distribution. A relatively small probability of obtaining a larger value indicated that the differences between test sections were large relative to the variability of results within test sections.

Table 3.5.1 As-constructed asphalt concrete properties.

Section	Thickness (mm)[a]	CV (%)	Density (kN/m^3) (cores)	CV (%)	Air Voids (%)	CV (%)	Asphalt Cement (%)	Marshalls	
								Stability (lbs.)	Flow
PCS1	75.0	N/A	N/A	N/A	N/A	N/A	N/A	N/A	N/A
CS1	77.7 (10)	3.8	22.5 (3)	0.9	7.4 (3)	10.9	6.8	1840 (3)	15
CS2	78.4 (10)	2.3	23.1 (6)	0.4	3.3 (6)	12.6	6.8	2013 (6)	26
CS3	80.3 (9)	2.6	21.9 (5)	2.1	7.9 (4)	7.6	6.6	1440 (5)	17
CS5	76.2 (10)	3.0	22.6 (6)	2.1	5.6 (6)	35.6	6.1	2292 (6)	13
CS6	75.3 (10)	1.4	23.3 (6)	0.2	3.1 (6)	10.3	6.6	2471 (6)	18
CS7	75.3 (10)	2.6	22.9 (6)	1.6	4.3 (6)	34.2	6.6	1979 (6)	16
CS8	76.3 (10)	2.7	23.1 (6)	0.7	3.3 (6)	17.9	6.1	2527 (6)	15
CS9	79.0 (10)	3.7	22.7 (6)	2.0	5.2 (6)	35.5	6.3	2167 (6)	14
CS10	75.1 (10)	1.6	22.9 (6)	1.0	4.3 (6)	22.0	6.5	2190 (6)	13
CS11	77.4 (10)	4.6	23.4 (6)	0.4	1.9 (6)	17.8	6.0	2480 (6)	20
SSS1	78.4 (9)	10.8	23.0 (9)	1.4	4.1 (9)	33.0	5.4	2956 (4)	17
SSS2	79.1 (10)	5.6	22.6 (10)	1.9	6.3 (10)	24.8	5.7	2043 (4)	18
SSS3	77.0 (9)	3.2	22.4 (9)	3.2	6.7 (9)	30.0	6.2	1372 (4)	17
SSS4	77.5 (10)	2.7	22.8 (10)	1.1	4.4 (10)	24.9	6.1	2125 (4)	17
SSS5	75[b]	N/A	N/A	N/A	N/A	N/A	4.7	4716 (3)[d]	10[d]
SSS6	75[b]	N/A	N/A	N/A	N/A	N/A	4.7	5400 (3)[d]	10[d]
SSS7	75[b]	N/A	22.1[c]	N/A	N/A	N/A	5.3	4933 (3)[d]	8[d]
SSS8	75[b]	N/A	21.5[c]	N/A	N/A	N/A	5.9	6970 (3)[d]	10[d]
SSS9	75[b]	N/A	21.9[c]	N/A	N/A	N/A	5.1	4630 (3)[d]	9[d]

Note: The number of samples is listed next to the measured quantity in parentheses()
N/A= Not Available
[a] Average thickness of 100 mm and 150 mm diameter cores
[b] Cold-mix sections in which cores were not possible
[c] In-place densities measured by nuclear densometer
[d] Re-compacted Marshall's from bulk sample

Table 3.5.2 provides the results of this analysis. The values listed in this table are significance parameters and have the meaning that if the value is less than 0.05, it can be stated with confidence that significant differences exist between test sections in terms of the measurement parameter used in the analysis. From Table 3.5.2 it is seen that significant

differences in these three parameters exist within each test section group with the exception of thickness for the SSS1-SSS4 group.

Table 3.5.2 Significance of variations of AC layer properties between test sections.

	Thickness	Density	Air Voids
CS1-CS11	0.000	0.000	0.000
SSS1-SSS4	0.930	0.021	0.001

When significant differences were noted between test sections for a variable, a multiple pairwise comparison was made. The null hypothesis that the two means between two test sections were equal was tested for each possible pair. The Least Significant Difference (LSD) method was used to test the null hypothesis. The significance of a calculated test statistic was quantified as the probability of obtaining a larger value from the student *t* distribution. A relatively small probability of obtaining a larger value indicated that the difference between the two test sections was large relative to the variability of this difference.

The remaining tables and discussion focuses on which sections are statistically different with respect to the parameters given above. Table 3.5.3 shows the significance of variations in AC thickness for the clay subgrade sections. Section CS10 contained the minimum average thickness (75.1 mm) and was used for comparison to the remaining sections. As such, all the remaining sections contained a thicker AC layer. From this table it is seen that in terms of thickness, sections CS3 and CS9 are significantly different from CS10. It will be shown in Section 5 that CS3 performed poorly with respect to CS7. CS3 and CS7 have identical test section variables. CS3 contained a greater average AC thickness and showed a significance of 0.001 when compared to CS7. Given the AC thickness data, it would be expected that CS3 would have performed better than CS7, when in fact the results show the opposite. This suggests that the significance in the variation of AC thickness does not result in a corresponding significance in overall rut development performance or that the pavement performance improvement due to a 5 mm increase in AC thickness of CS3 over CS7 is outweighed by variations in density or air voids between these two sections. Examination of CS2 and CS8 also provides insight into the importance of variations in AC thickness. A 2.1 mm difference in AC thickness existed between these sections with CS2 being thicker. The average density and air voids of the AC between these two sections was identical. As will be shown in Section 5, the

performance of CS2 and CS8 was essentially identical with CS2 performing slightly better. This suggests that this level of difference in AC thickness does not have a significant impact on pavement response.

Table 3.5.3 Significance of variations in AC thickness between CS sections.

	CS1	CS2	CS3	CS5	CS6	CS7	CS8	CS9	CS11
CS10	0.270	0.062	0.000	0.978	1.000	1.000	0.978	0.011	0.469

Table 3.5.4 shows the significance of variations in AC air voids between the clay subgrade sections. Section CS2, which was one of the unreinforced sections, was used for comparison. From this table it is seen that the two unreinforced sections (CS2, CS8) and the geotextile section (CS6) compare very well. Sections CS1 and CS3 compare very poorly and are statistically different from the control section. The remaining sections are not statistically different from CS2, however CS5 is close to being statistically different.

Table 3.5.4 Significance of variations in AC air voids between CS sections.

	CS1	CS3	CS5	CS6	CS7	CS8	CS9	CS10	CS11
CS2	0.001	0.000	0.067	1.000	0.908	1.000	0.218	0.916	0.631

CS1 and CS3 have an AC air voids that is significantly greater than CS2. As shown in Table 3.5.3, AC thickness between these two sections was not significantly different. It might be expected that the performance of CS1 and CS3 would be poor in light of this variable. It might also be expected that the performance of CS5 would be somewhat better if the air voids in the AC of this section was more comparable to CS2 and the other sections.

Table 3.5.5 shows the significance of variations in AC air voids between the silty-sand subgrade sections SSS1-SSS4. The results show that SSS1 and SSS4 (the two control sections) are very comparable but SSS2 and SSS3 are not comparable to the controls in terms of AC air voids. The significance between SSS2 and SSS3 was 0.994, which indicates that these two sections are very comparable. Later in this section, as-constructed properties of the base and subgrade are presented and discussed in light of statistical variations. At the end of this section, a summary is made of what should be expected when making comparisons between sections.

Table 3.5.5 Significance of variations in AC air voids between SSS sections.

	SSS2	SSS3	SSS4
SSS1	0.018	0.005	0.988

Table 3.5.6 As-constructed base course properties.

	Construction			Excavation
Section	Thickness (mm)	Water Content (%)	Dry Density (kN/m^3)	Water Content (%)
PCS1	300	6.2	20.9	5.6
CS1	300	6.1	20.7	5.8
CS2	300	6.3	20.6	6.4
CS3	300	6.3	20.3	6.5
CS5	300	6.2	20.6	5.8
CS6	300	5.8	21.0	5.8
CS7	300	5.5	20.6	5.9
CS8	300	6.9	20.7	6.1
CS9	375	6.4	20.9	6.8
CS10	375	6.7	20.5	6.2
CS11	300	6.3	20.5	6.6
SSS1	210	7.6	20.6	5.7
SSS2	205	7.4	20.7	6.1
SSS3	200	7.1	20.8	5.5
SSS4	200	6.4	21.1	4.6
SSS5	200	6.3	20.2	5.2
SSS6	200	6.2	20.5	5.3
SSS7	200	6.3	20.5	5.0
SSS8	200	6.4	20.9	5.1
SSS9	200	6.0	20.9	5.1

As-constructed properties of the base course layer are given in Table 3.5.6. Listed in the table are compacted thickness, in-place water content and dry density measured during construction and water content measured during excavation. Water content and dry density are average values determined from approximately 16 and 20 samples, respectively. The coefficient of variation (CV) associated with the samples used to report the average values given in Table 3.5.6 are listed in Table 3.5.7. Variations in dry density within a given test section are relatively minor, indicating good quality control during construction. The variations in water content are more significant. It is believed, however, that the impact of the variation in compacted water

content in the base on test section performance is small and that dry density is a more important parameter controlling test section performance. The CV of average dry density of the base for both the CS and SSS sections was 1.0 %, which is within the range of CV for the individual test sections. Given these results, minor differences in test section performance due to variations in the mechanical properties of the base course aggregate are expected.

Table 3.5.7 Coefficient of variation for base course and subgrade construction.

	Basecourse		Subgrade	
Section	Dry Density CV (%)	Water Content CV (%)	Dry Density CV (%)	Water Content CV (%)
PCS1	1.2	5.4	1.7	3.7
CS1	2.6	3.2	0.4	1.3
CS2	1.2	9.0	1.9	0.6
CS3	1.5	6.9	1.8	2.1
CS5	2.9	3.2	1.5	1.1
CS6	2.3	17.2	1.6	1.6
CS7	1.8	15.5	1.8	2.8
CS8	1.8	3.2	1.3	2.6
CS9	1.6	5.6	1.4	1.6
CS10	1.5	8.6	1.4	3.1
CS11	2.0	4.5	1.6	0.9
SSS1	0.7	3.7	1.1	0.8
SSS2	0.6	3.7	1.1	0.8
SSS3	0.6	4.5	0.9	0.7
SSS4	1.9	5.6	1.2	1.4
SSS5	0.9	1.1	N/A[a]	N/A[a]
SSS6	1.4	1.1	N/A[a]	N/A[a]
SSS7	0.6	1.1	N/A[a]	N/A[a]
SSS8	1.9	1.1	N/A[a]	N/A[a]
SSS9	1.5	0.0	N/A[a]	N/A[a]

[a] Subgrade was reused from SSS4

As-constructed properties of the clay and silty-sand subgrades are listed in Table 3.5.8. Average values of water content and dry density are reported from approximately 40 and 50 samples, respectively. The coefficient of variation for water content and dry density within a given test section are shown in Table 3.5.7. These values indicate that excellent uniformity of subgrade properties were achieved during construction of a given test section. Comparison of average values between the clay test sections resulted in a coefficient of variation of 1.2 % and

1.1 % for water content and dry density, respectively, which is within the range of CV for individual clay sections. For the SSS1-SSS4 sections, the CV between sections for water content and dry density was 0.6 and 0.3, respectively, which is less than any of the CV's reported for an individual silty-sand section. Given these results, minor differences in test section performance due to variations in the mechanical properties of the subgrade are expected.

Table 3.5.8 As-constructed subgrade properties.

		Construction			Excavation	
Section	Thickness (mm)	Water Content (%)	Dry Density (kN/m^3)	Pretest CBR	Water Content (%)	Dry Density (kN/m^3)
PCS1	1045	43.6	11.6	1.5[e]	42.4	11.6
CS1	1045	44.8	11.5	1.5[e]	43.4	11.7
CS2	1045	44.8	11.4	1.5[e]	43.9	11.6
CS3	1045	44.9	11.5	1.5[e]	44.1	11.8
CS5	1045	44.9	11.4	1.5[e]	43.3	11.4
CS6	1045	44.4	11.1	1.5[e]	44.6	11.4
CS7	1045	44.2	11.4	1.5[e]	44.7	11.4
CS8	1045	44.8	11.5	1.5[e]	44.5	11.5
CS9	970	44.9	11.4	1.5[e]	44.6	11.3
CS10	970	44.9	11.3	1.5[e]	44.7	11.2
CS11	1045	45.1	11.4	1.5[e]	43.7	11.5
SSS1	1128	14.7	17.0	14.0[d]	14.8	17.1
SSS2	1131	14.9	17.0	15.0[d]	13.2	17.3
SSS3	1147	14.8	17.1	15.5[d]	14.0	17.0
SSS4	1145	14.8	17.1	16.0[d]	11.7	N/A
SSS5	1145[a]	12.6[b]	N/A	20.5[d]	11.3[b]	N/A
SSS6	1145[a]	N/A	N/A	20.2[d]	N/A	N/A
SSS7	1145[a]	11.4[b]	18.3[c]	21.7[d]	11.4[b]	18.3[c]
SSS8	1145[a]	12.5[b]	18.0[c]	22.9[d]	12.5[b]	18.0[c]
SSS9	1145[a]	N/A	18.0[c]	24.0[d]	13.8[b]	17.7

[a] Subgrade from SSS4 was re-used for these tests
[b] Measurements taken 60 mm below top of subgrade
[c] Measurements taken at base/subgrade interface
[d] Defined by the DCP test
[e] Defined from laboratory CBR tests at corresponding in-situ water content
N/A = Not Available

The presentation of as-constructed properties for the AC, base and subgrade materials has shown that excellent quality control was achieved with respect to compacted dry density of the base and dry density and water content of the subgrade and that no statistical differences exist between the base and subgrade of test sections within the CS and SSS series. The minor differences in compacted water content of the base are believed to be insignificant in terms of impact on test section performance. For the AC, it was shown that statistical differences in AC thickness existed for two of the test sections in the CS series (CS3 and CS9) while the SSS series showed no differences. Additionally, it was argued that the differences seen in AC thickness in the CS series tests had a minor influence on overall test section performance.

With respect to AC air voids, it was seen that statistical differences existed between CS1 and CS3 as compared to the remaining CS test sections. The performance of CS1 and CS3 was better than CS2 and CS8 but was considerably worse than that of CS11 and CS7, which were repeats of CS1 and CS3, respectively. Given the data presented above, it is concluded that the increased AC air voids in CS1 and CS3 was responsible for the poor behavior exhibited by these test sections and that this is a critical control parameter needed for proper comparison of test sections. For this reason, results from CS1 and CS3 have not been included in Section 5 and results from CS11 and CS7, which were statistically comparable to the control sections, have been used in their place. It should also be noted that the rutting behavior of CS1 and CS3 showed an acceleration in the rate of rutting midway through the test which is believed to be due to fatigue of the improperly compacted AC material. This type of behavior was not seen for the other test sections for which air voids was more comparable to the control sections. The statistical analysis also showed that CS5 had an AC air voids which placed it on the fringe of being statistically different from the control sections. In Section 5, it might be expected that CS5 would have performed slightly better if its air voids had been more comparable.

For the silty-sand subgrade sections SSS1-SSS4, it was noted that sections SSS1 and SSS4 were very comparable and that SSS2 and SSS3 were also very comparable, but that the two sets were not comparable to each other with respect to AC air voids. For this reason, it is not possible to directly compare SSS2 and SSS3 to SSS1 or SSS4. Certain, qualified comparisons between these sections will, however, be made in Section 5. It should be noted that the identification of viscoelastic material parameters for the AC material from various test sections will allow for comparisons of all test sections as part of the numerical modeling work being conducted at the

time of this report. It should also be noted that the use of cold-mix AC in test sections SSS5-9 led to performance that was inconsistent between test sections. For this reason, only certain results from these test sections will be used in Section 5 to illustrate reinforcement mechanisms.

3.6 Instrument Response and Measurement Consistency

A preliminary clay section termed PCS1 was constructed in order to provide insight on the performance of an unreinforced clay section and to provide information on instrument response and measurement consistency. This section describes the instrumentation used with PCS1, loading of the section, and an illustration and discussion of measurement consistency. The plots of instrument response given in this section are not necessarily intended for comparison to other sections, but are primarily used to show measurement consistency and trends in stress and strain fields. Data on stress and strain fields from PCS1 not given in this section will be given in Section 4.

Construction of PCS1 was similar to other clay sections, except that fewer instruments were installed. The location of these instruments was described at the end of Section 3.4.3. With instruments arranged in this fashion, fields of stress and strain were obtained by moving the load plate and applying load at a series of locations on the pavement surface. With this section, the load was moved in two perpendicular directions parallel to the box walls from the center of the box in 100 mm increments, resulting in a total of 41 load applications. At each location, three load pulses were applied to the pavement surface. The duplication of instruments allows for direct comparison of measurement responses to evaluate measurement consistency. Information on measurement consistency and stress and strain fields was used in establishing an instrument plan for subsequent test sections.

Other means of establishing consistency of measurement response and test section behavior includes an examination of similar variables measured in two duplicate control test sections with the clay subgrade (CS2 and CS8) and two control sections with the silty-sand subgrade (SSS1 and SSS4). When applicable, additional examples of measurement consistency between sections CS2 and CS8 and sections SSS1 and SSS4 will be illustrated in Section 5.

Figure 3.6.1 illustrates peak vertical strain from two soil strain cells located in the base course layer of PCS1. Peak measures of stress and strain refer to the peak value of the time-history response curve for the single load pulse application. The peak vertical strain was

determined for each of the three load pulses applied at different radii from the sensor. The cells were located at a depth of 300 mm below the AC surface, as noted in the figure caption. The data labels denote the sensor number from which the data was generated where exact locations of these sensors is contained in the tables in Appendix A. Figure 3.6.2 shows peak vertical strain in the top of the subgrade for two soil strain sensors from section PCS1. Figure 3.6.3 illustrates reasonable agreement between two radial soil strain sensors in the top of the subgrade layer. Figures 3.6.4 and 3.6.5 show a distribution of peak vertical stress in the base and the top of the subgrade, respectively, from duplicate stress cells from section PCS1. Figures 3.6.6 and 3.6.7 illustrate the consistency of the time-history of response for stress and strain measures. Figure 3.6.6 shows a measure of vertical stress in the subgrade from two different sensors, while Figure 3.6.7 shows a measure of radial strain in the base. Figures 3.6.1 – 3.6.7 illustrate good peak measurement response consistency for duplicate sensors contained in one test section subject to a dynamic load pulse.

The following three figures present information from long-term measurements from test sections CS2 and CS8. Figure 3.6.8 illustrates the permanent rut development of both sections, exhibiting good agreement for two sections constructed identically. Figure 3.6.9 shows permanent radial strain in the bottom of the base for two control sections (CS2 and CS8). Permanent response measures refer to measurements taken between load pulse applications where the applied load is zero. Figure 3.6.10 shows the dynamic vertical stress directly beneath the load center in the top of the subgrade versus load cycle. Dynamic stress is taken as the difference between the peak value of stress for the load pulse and the permanent value of stress on the sensor taken immediately before the load pulse is applied.

Figures 3.6.11 – 3.6.13 provide a comparison of results between two control sections (SSS1 and SSS4) where the silty-sand subgrade was used. Figure 3.6.11 shows the permanent radial strain versus cycle number at the bottom of the base layer. Figure 3.6.12 gives the dynamic vertical stress measured in the top of the subgrade versus load cycle number. Figure 3.6.13 provides a comparison of the vertical strain measured in the top of the subgrade. The consistency of these measures between these two identical sections is very good.

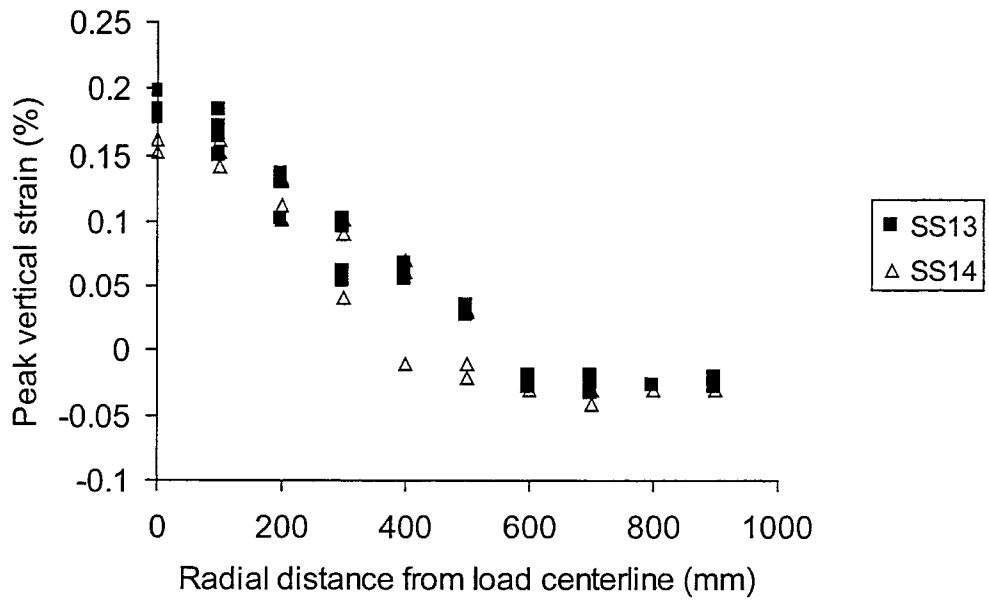

Figure 3.6.1 Peak vertical strain in the base versus radial distance (PCS1, Z=300 mm).

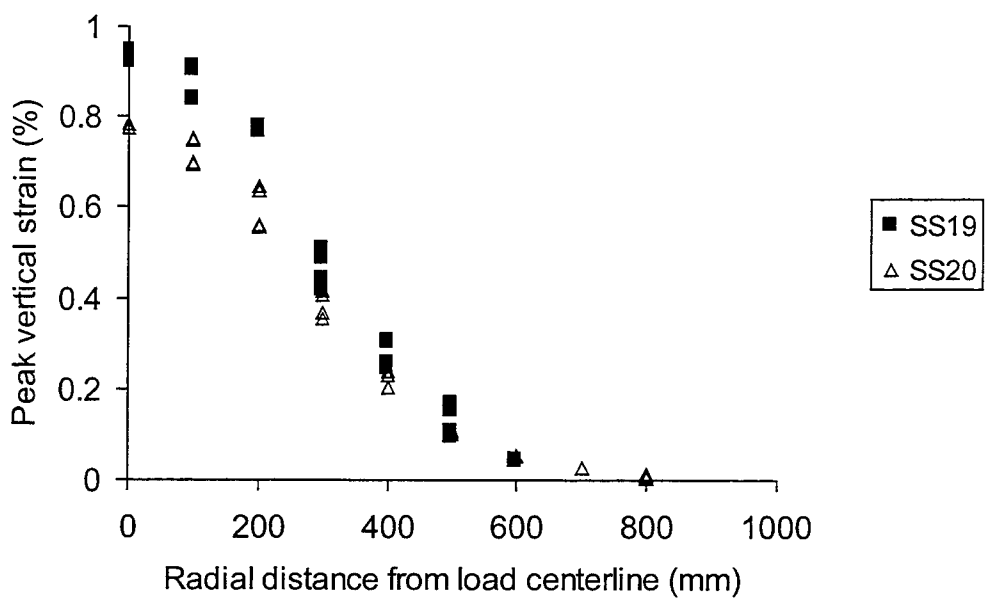

Figure 3.6.2 Peak vertical strain in the subgrade versus radial distance (PCS1, Z=450 mm).

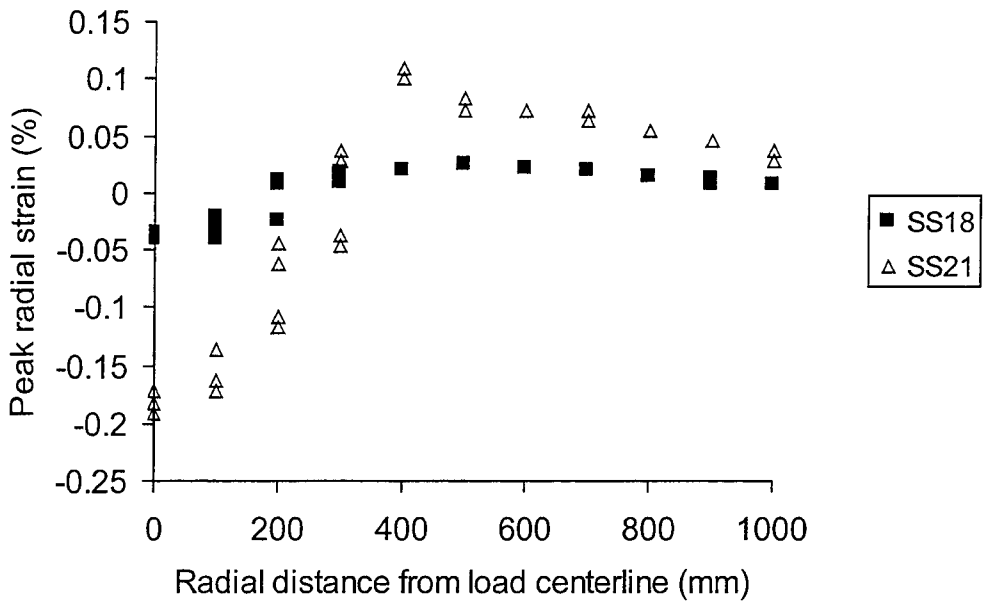

Figure 3.6.3 Peak radial strain in the subgrade versus radial distance (PCS1, Z=415 mm).

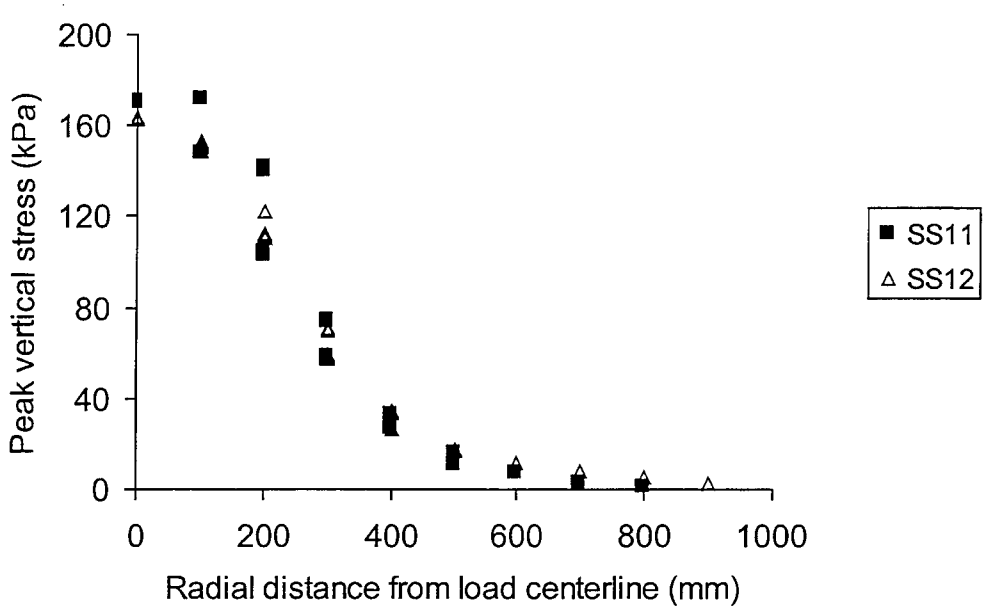

Figure 3.6.4 Peak vertical stress in the base versus radial distance (PCS1, Z=300 mm).

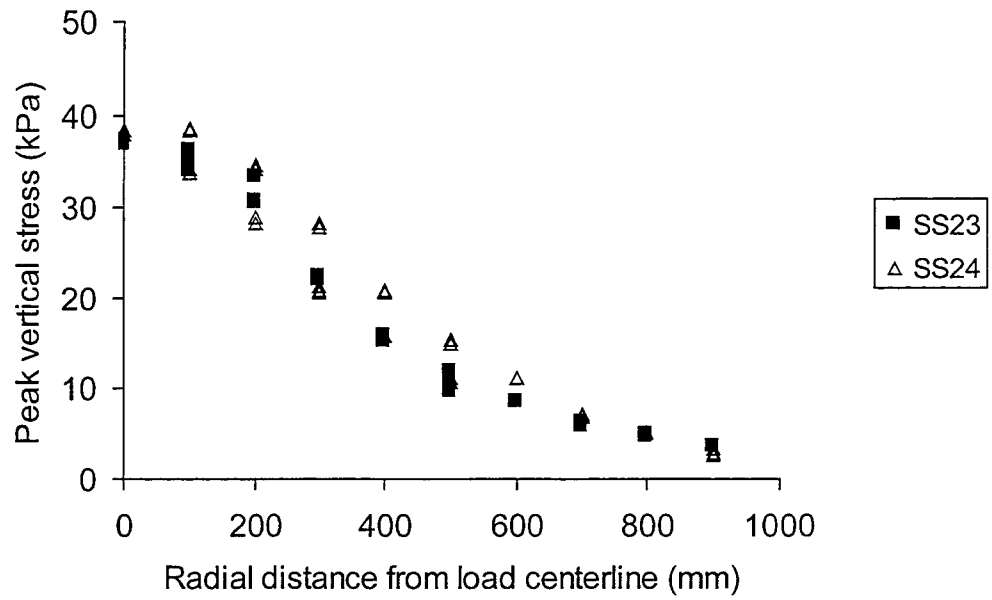

Figure 3.6.5 Peak vertical stress in the subgrade versus radial distance (PCS1, Z=675 mm).

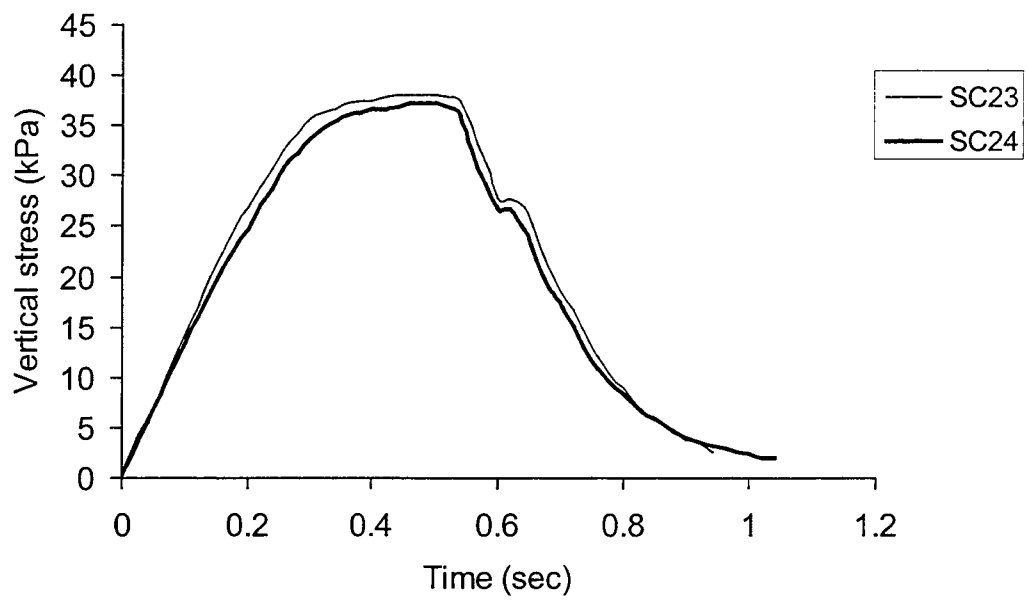

Figure 3.6.6 Time-history of vertical stress in the subgrade (PCS1, R=0, Z=675 mm).

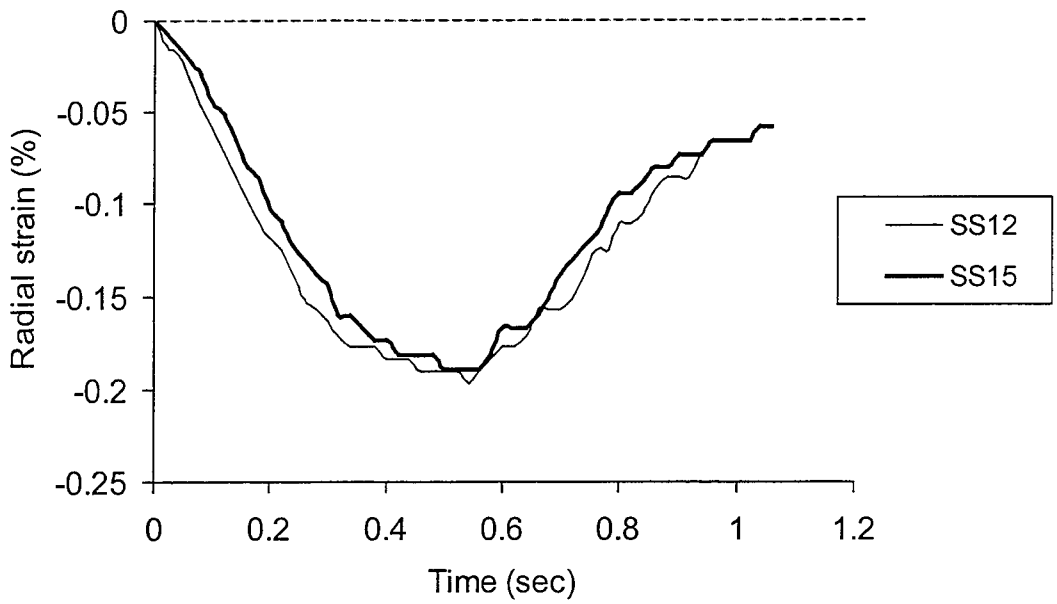

Figure 3.6.7 Time-history of radial strain in the base (PCS1, R=100 mm, Z=355 mm).

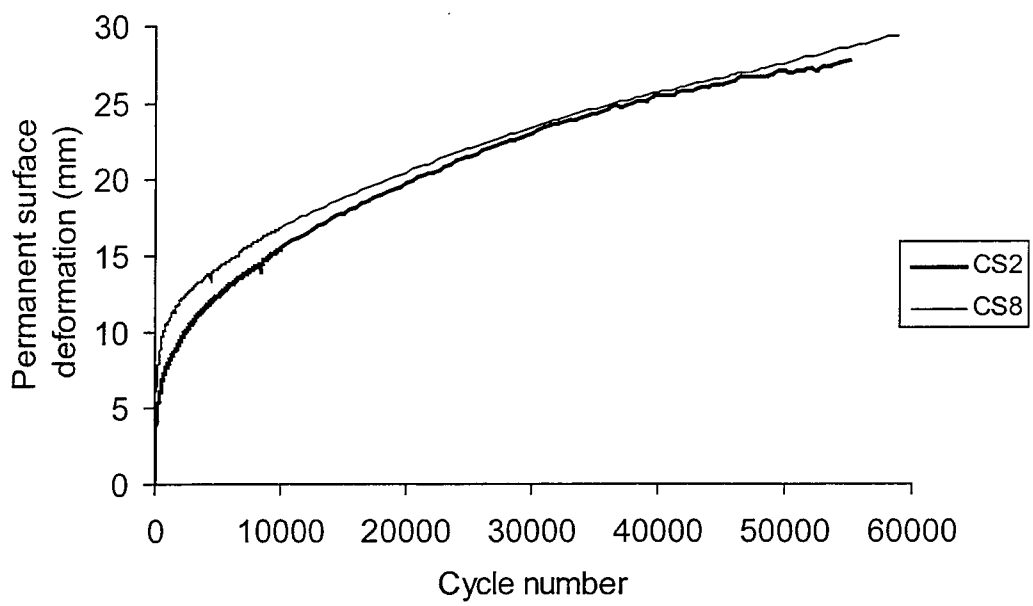

Figure 3.6.8 Permanent rut development for unreinforced test sections (CS2, CS8).

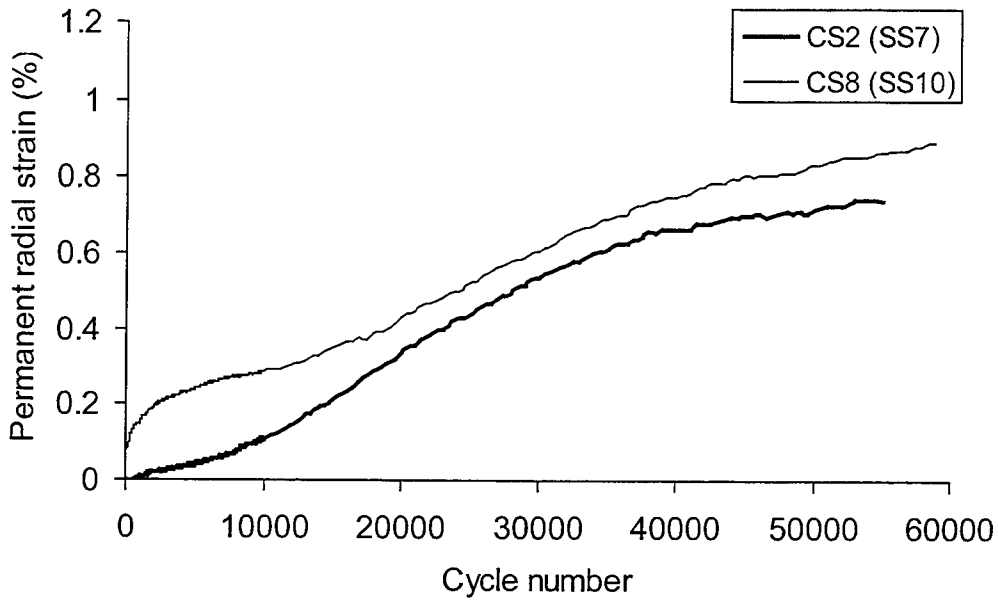

Figure 3.6.9 Permanent radial strain in the base versus load cycle (CS2, CS8, R=200 mm, Z=355 mm).

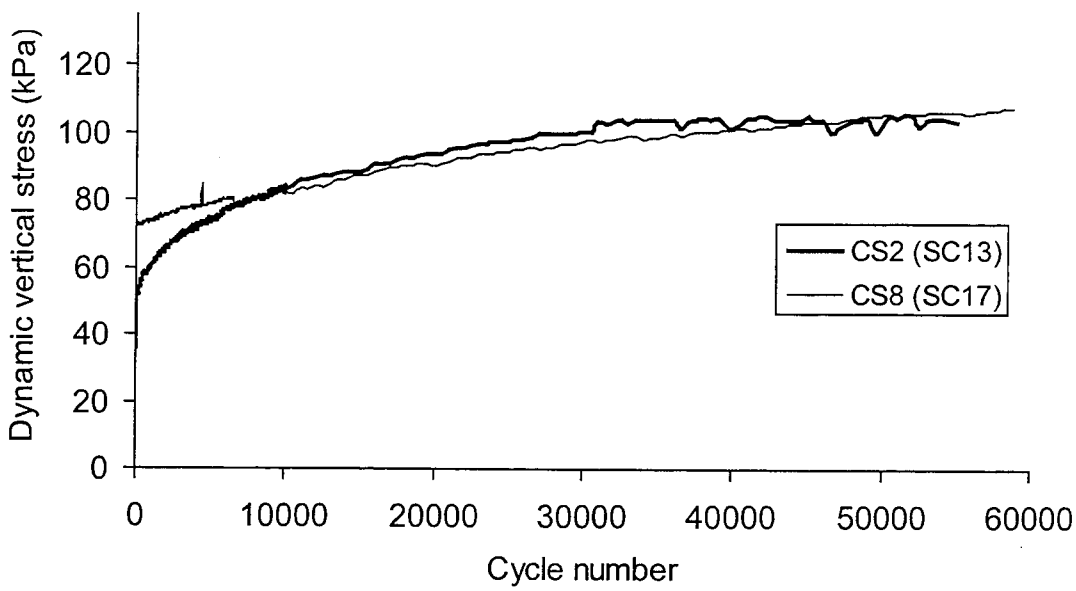

Figure 3.6.10 Dynamic vertical stress in the subgrade versus load cycle (CS2, CS8, R=0, Z=450 mm).

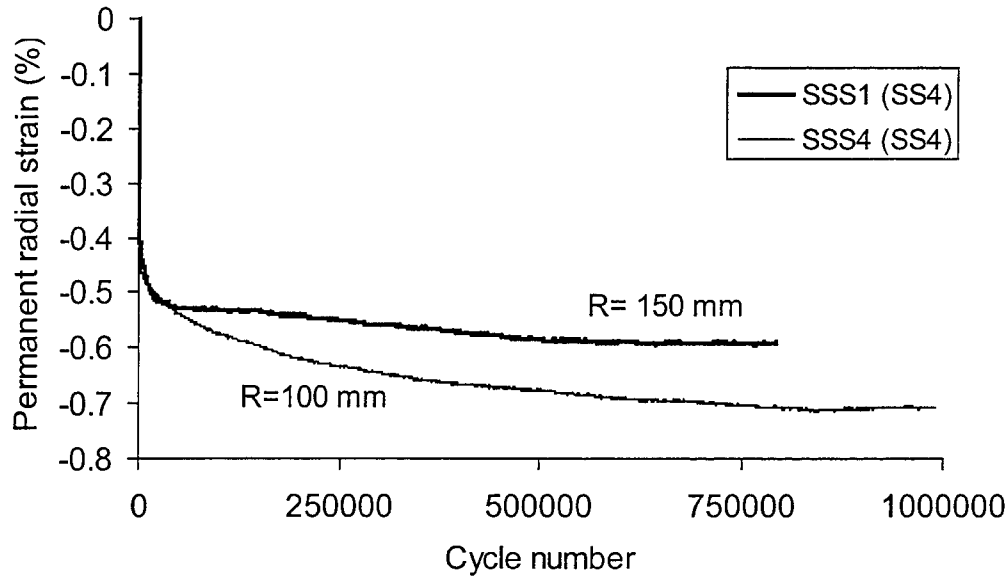

Figure 3.6.11 Permanent radial strain in the base versus load cycle (SSS1, SSS4, Z=215 mm).

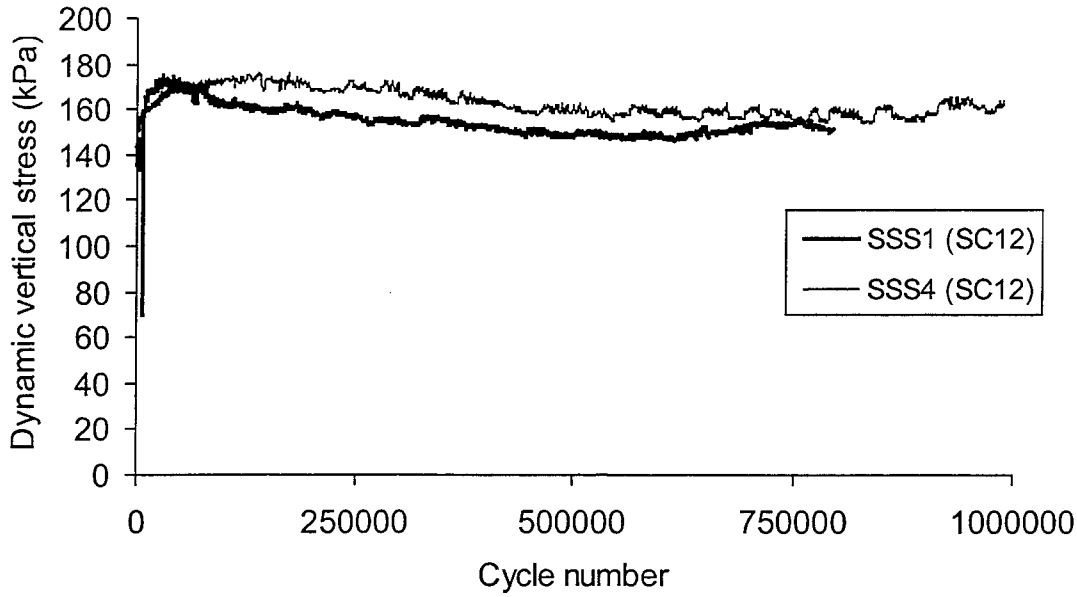

Figure 3.6.12 Dynamic vertical stress in the subgrade versus load cycle (SSS1, SSS4, R=0, Z=350 mm).

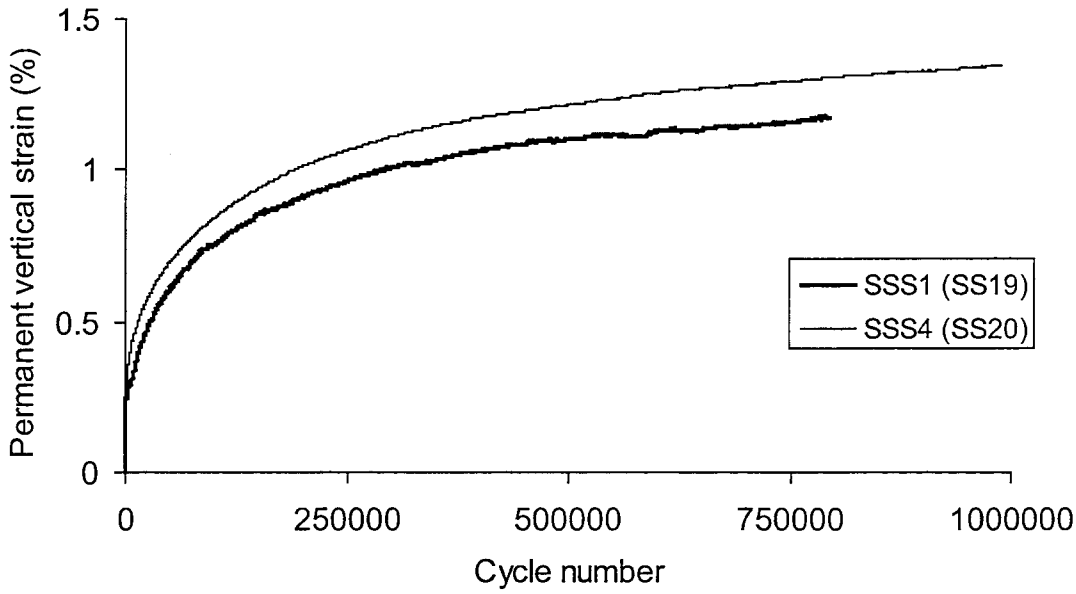

Figure 3.6.13 Permanent vertical strain in the subgrade versus load cycle (SSS1, SSS4, R=60 mm, Z=575 mm).

4.0 DYNAMIC STRESS AND STRAIN FIELDS

The purpose of this section is to present additional results from the preliminary clay section PCS1 that illustrate trends in stress and strain parameters for the pavement layers. Section PCS1 contained no reinforcement. The results are not intended to provide insight into reinforcement functions but are rather presented to show trends in stress and strain measures in the pavement layers. An examination of these trends is useful when data from the other sections discussed in Section 5 is examined. The data presented in this section has been obtained by applying single load pulses to section PCS1 in the manner described in Section 3.6.

Figure 4.1 shows the response of the pavement surface given by the plate pressure plotted against the average displacement of the plate. The response is seen to be nonlinear and hysteretic. Figures 4.2 and 4.3 show the radial and tangential strain developed in the bottom of the AC layer. The strain plotted is the peak measure from the single pulse response curve. Positive strain is extensional. In the radial direction, extensional strain is developed out to a radius of approximately 250 mm, where after compressional stains are experienced. In the tangential direction, strains are always in extension.

Figures 4.4 and 4.5 show peak vertical stress and strain in the bottom of the base at a depth of 300 mm below the pavement surface. Positive stresses and strains correspond to compression. A slight lifting of the base is noted beyond a radius of approximately 600 mm. Figures 4.6 and 4.7 show radial stress and strain in the bottom of the base at depths of 225 and 355 mm below the pavement surface. Significant extensional radial strain is noted out to a radius of approximately 300 mm. A region of tensile stress is observed out to a radius of approximately 100 mm. Tensile values of stress do not imply that the aggregate was carrying a tensile load but simply that the compressive geostatic radial stresses present before the load application were released by the tensile values shown in Figure 4.6. The inability of the aggregate to carry tensile stresses clearly contributes to the magnitude of extensional strains seen in Figure 4.7. Fogelsong (1998) has shown that layered linear-elastic pavement models greatly overpredict the tensile stresses carried by the bottom of the base and as a result underpredict the radial extensional strains developed beneath the load centerline. Figures 4.8 and 4.9 show peak tangential stress and strain in the bottom of the base at depths of 300 and 355 mm below the pavement surface.

Similar measures made in the subgrade are shown in Figures 4.10-4.15. Figures 4.10 and 4.11 show peak vertical stress and strain in the top of the subgrade. Figures 4.12 and 4.13 show peak radial stress and strain in the top of the subgrade. Positive radial stresses are observed while extensional radial strain is seen out to a radius of approximately 250 mm. Figures 4.14 and 4.15 show peak tangential stress and strain in the top of the subgrade.

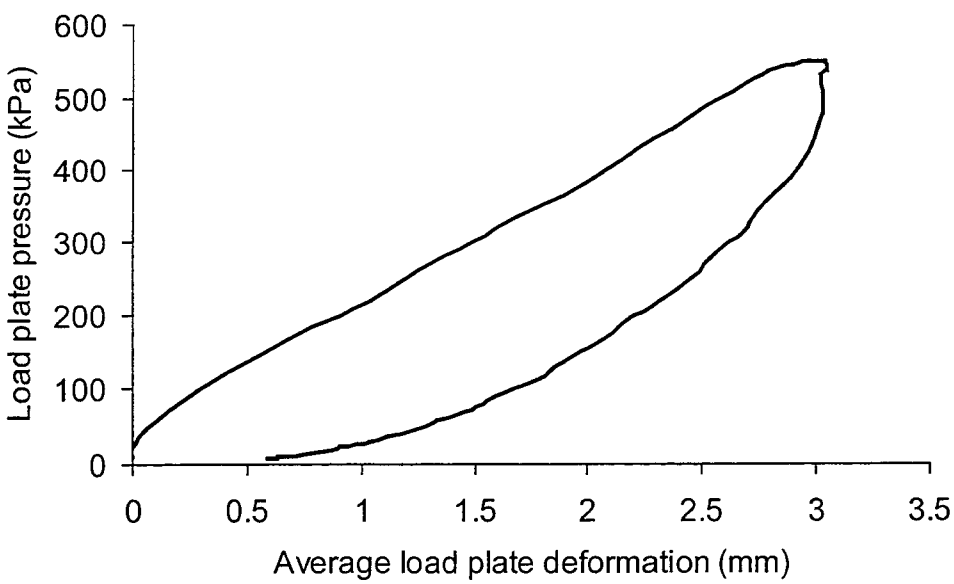

Figure 4.1 Dynamic load plate pressure versus displacement (PCS1).

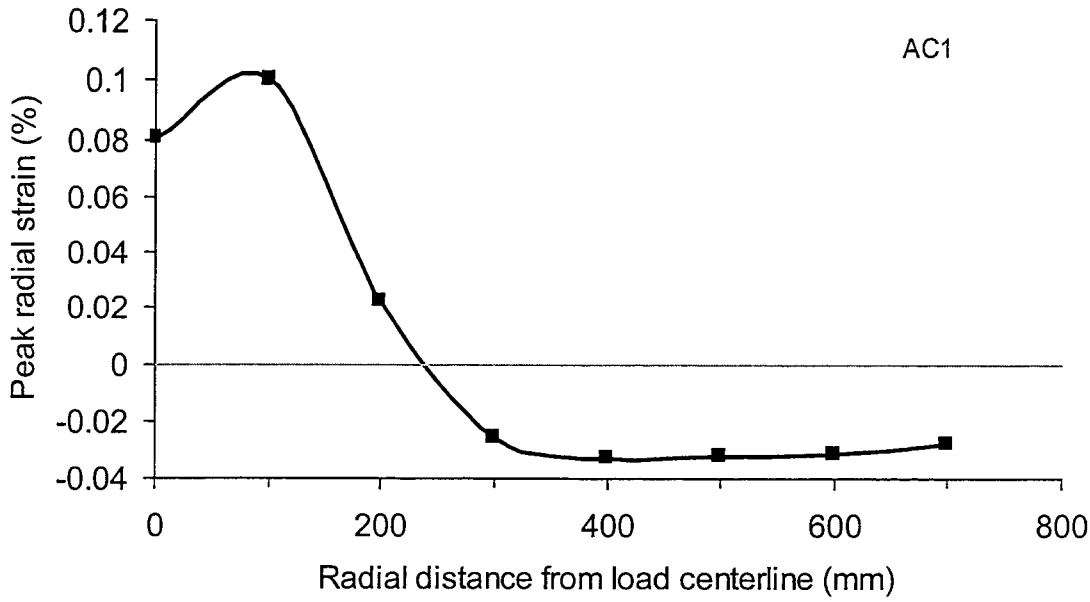

Figure 4.2 Peak radial strain in the AC versus radial distance (PCS1, Z=67 mm).

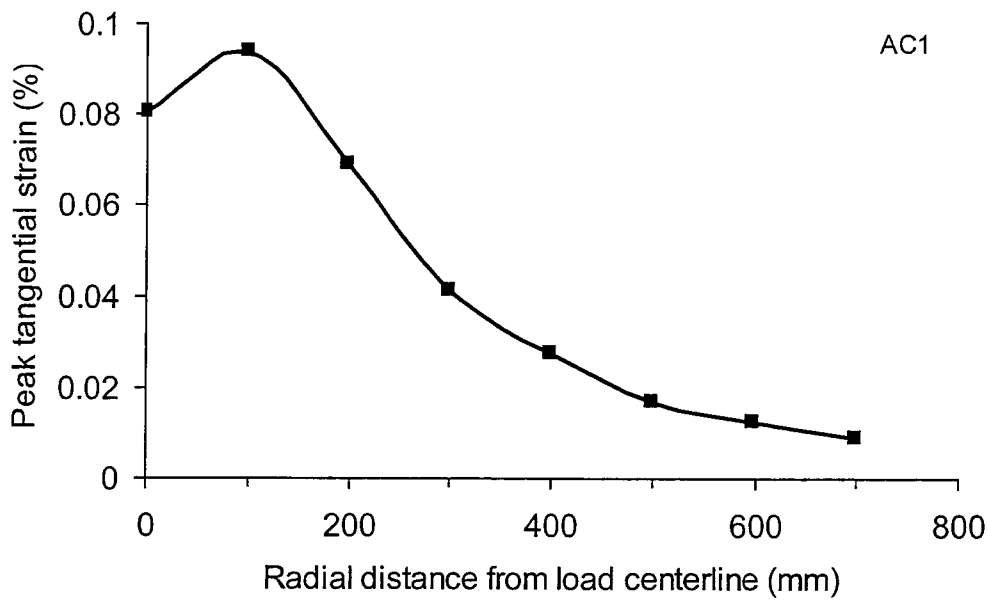

Figure 4.3 Peak tangential strain in the AC versus radial distance (PCS1, Z=67 mm).

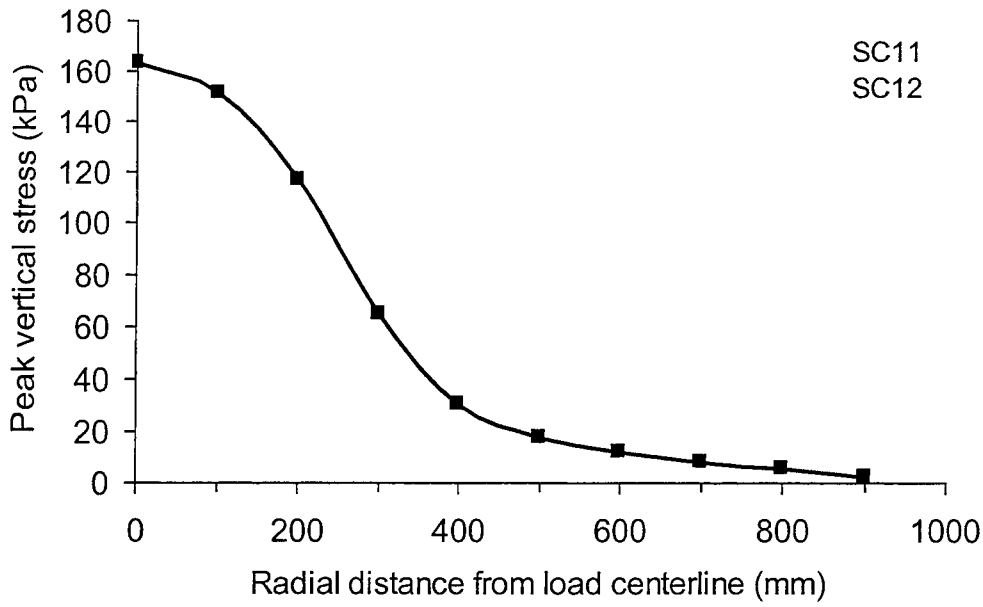

Figure 4.4 Peak vertical stress in the base versus radial distance (PCS1, Z=300 mm).

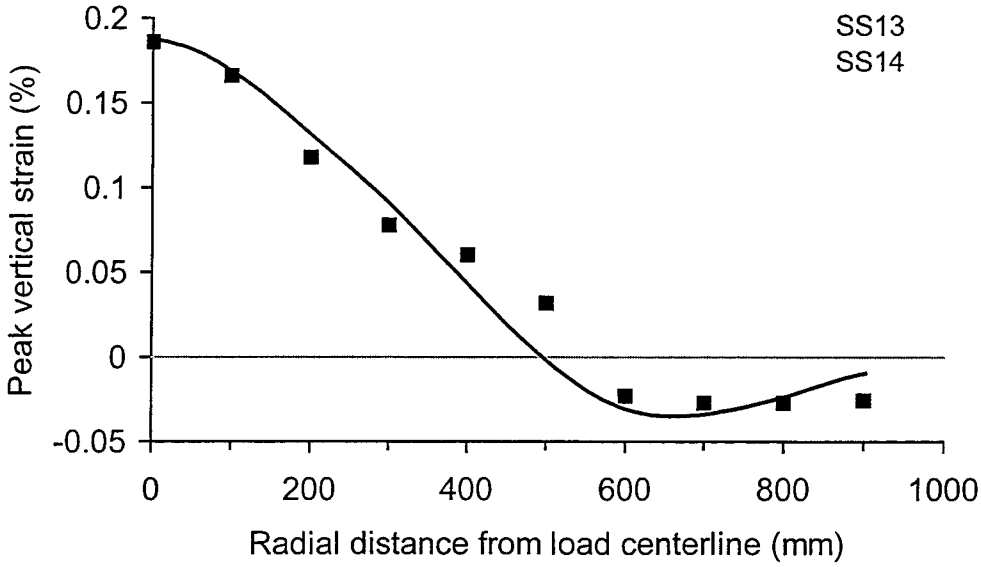

Figure 4.5 Peak vertical strain in the base versus radial distance (PCS1, Z=300 mm).

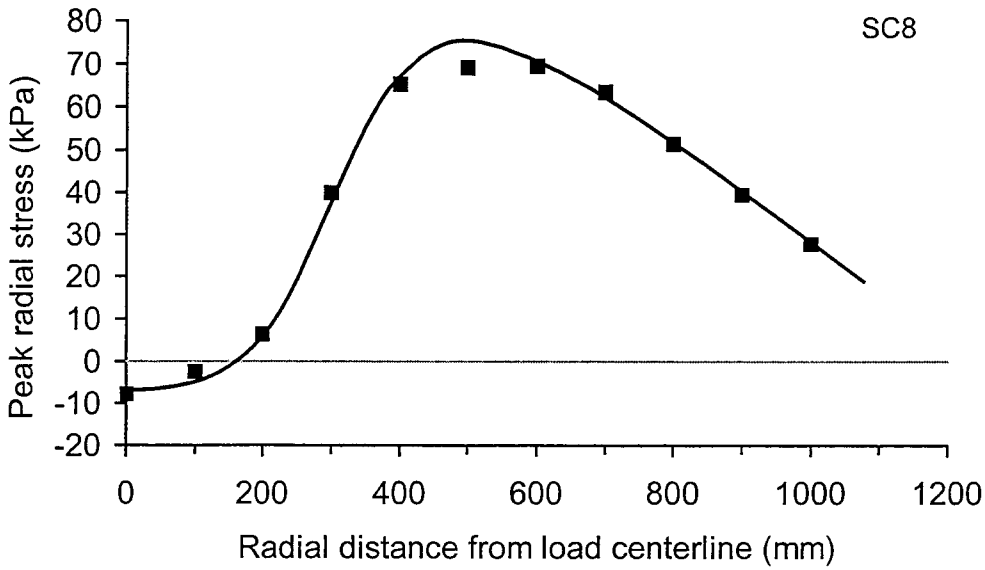

Figure 4.6 Peak radial stress in the base versus radial distance (PCS1, Z=225 mm).

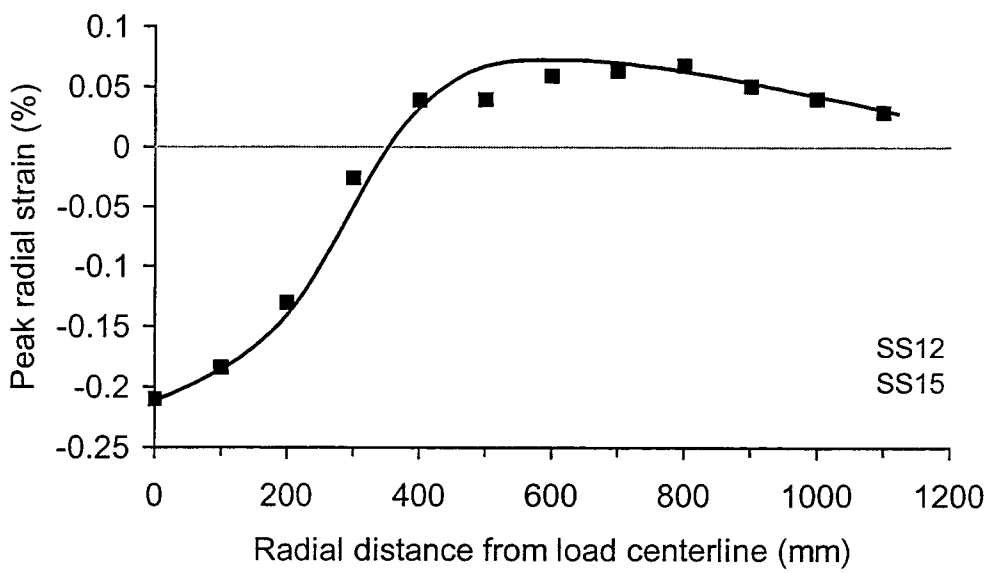

Figure 4.7 Peak radial strain in the base versus radial distance (PCS1, Z=355 mm).

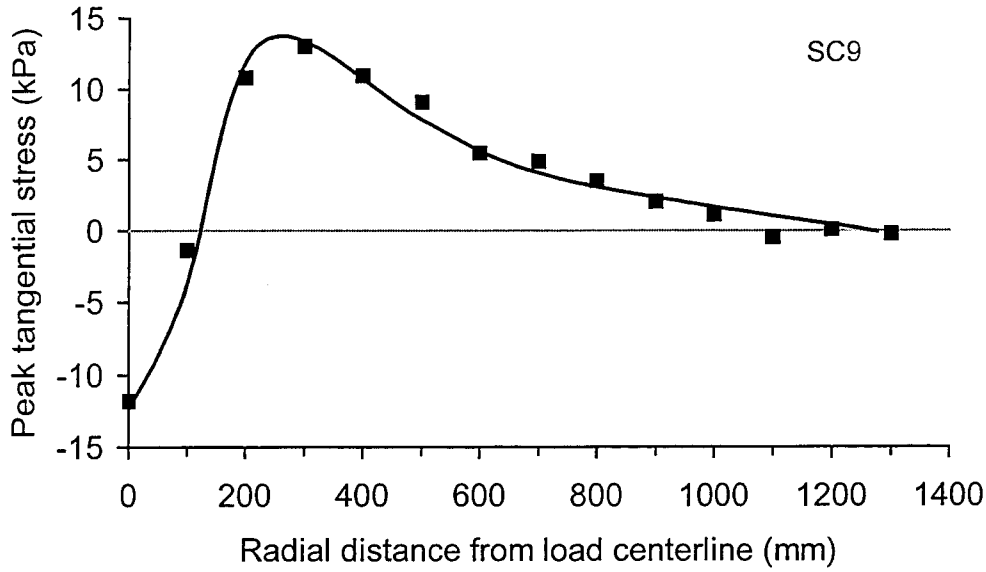

Figure 4.8 Peak tangential stress in the base versus radial distance (PCS1, Z=300 mm).

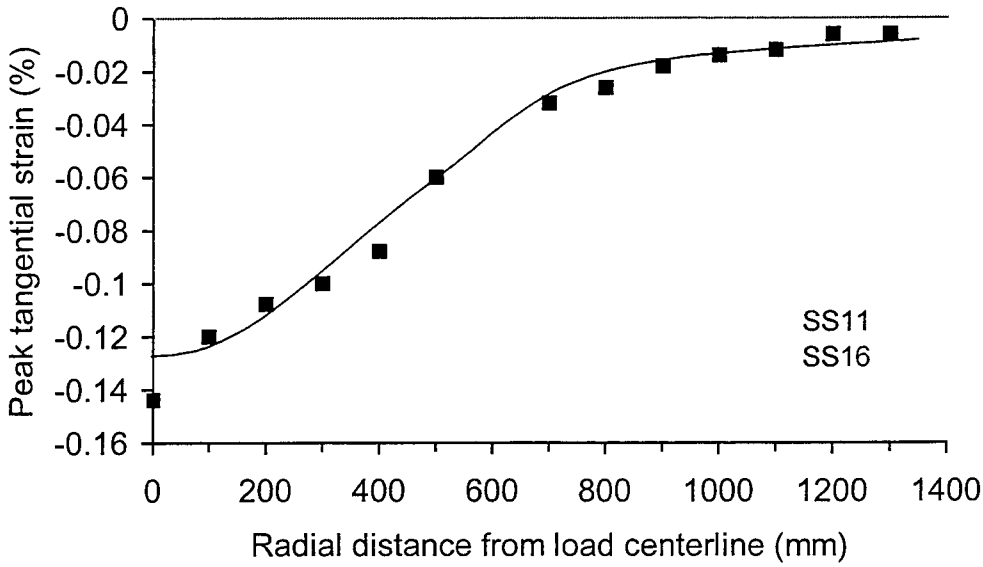

Figure 4.9 Peak tangential strain in the base versus radial distance (PCS1, Z=355 mm).

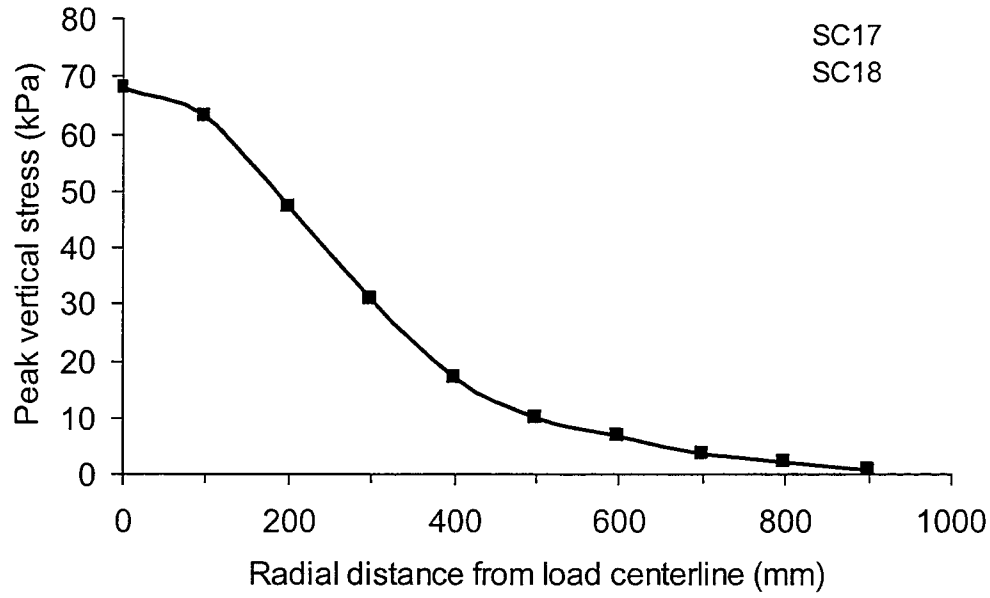

Figure 4.10 Peak vertical stress in the subgrade versus radial distance (PCS1, Z=450 mm).

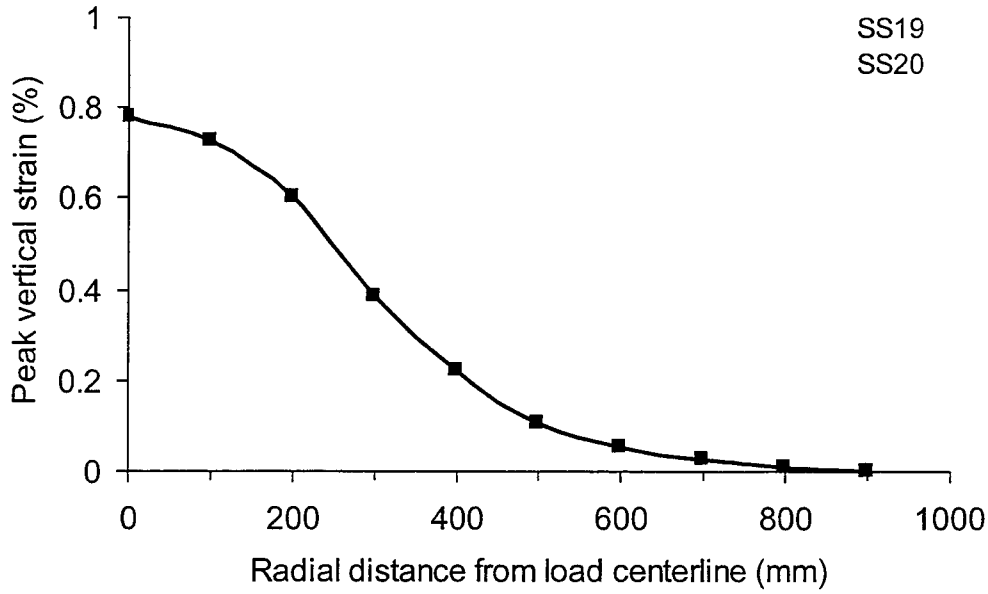

Figure 4.11 Peak vertical strain in the subgrade versus radial distance (PCS1, Z=450 mm).

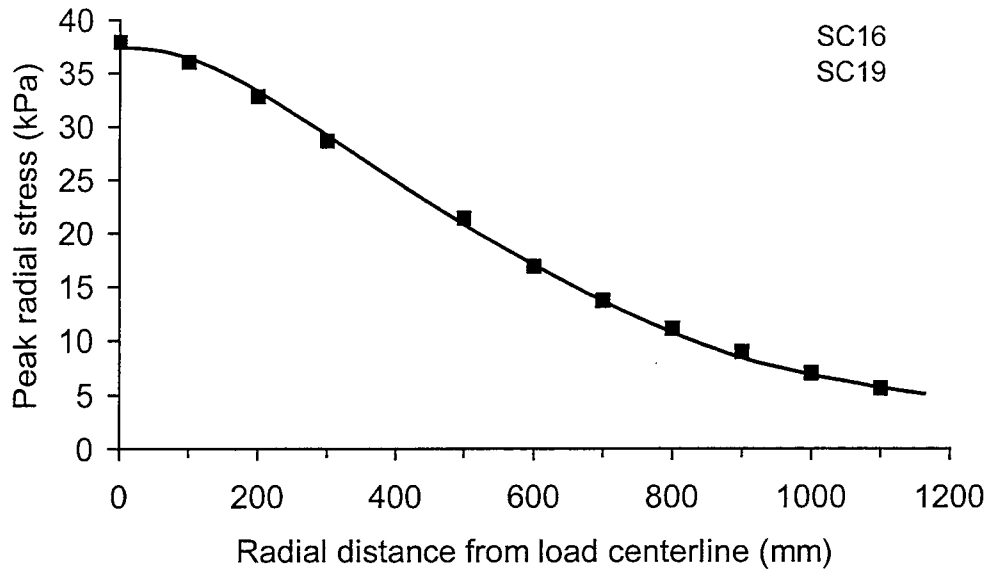

Figure 4.12 Peak radial stress in the subgrade versus radial distance (PCS1, Z=450 mm).

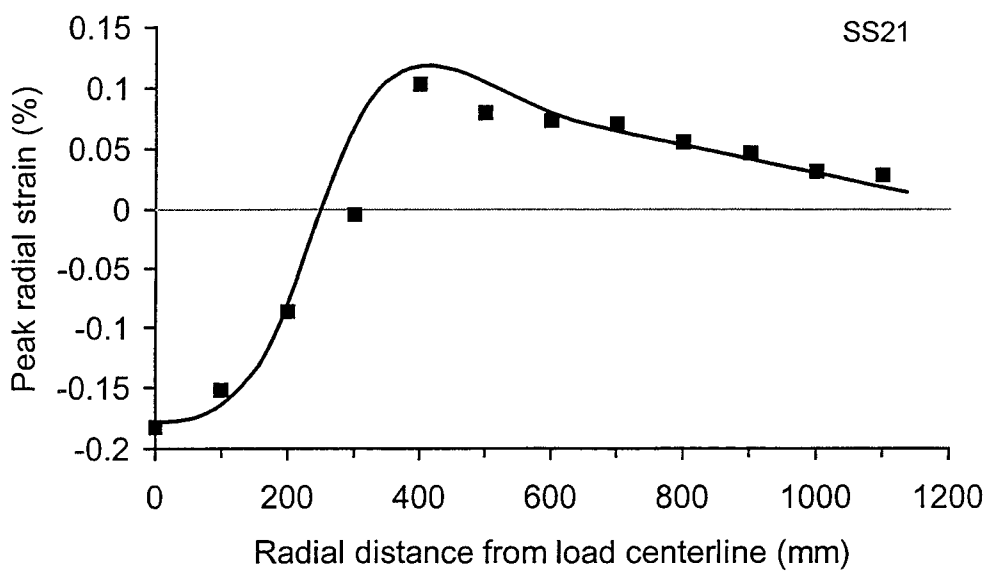

Figure 4.13 Peak radial strain in the subgrade versus radial distance (PCS1, Z=415 mm).

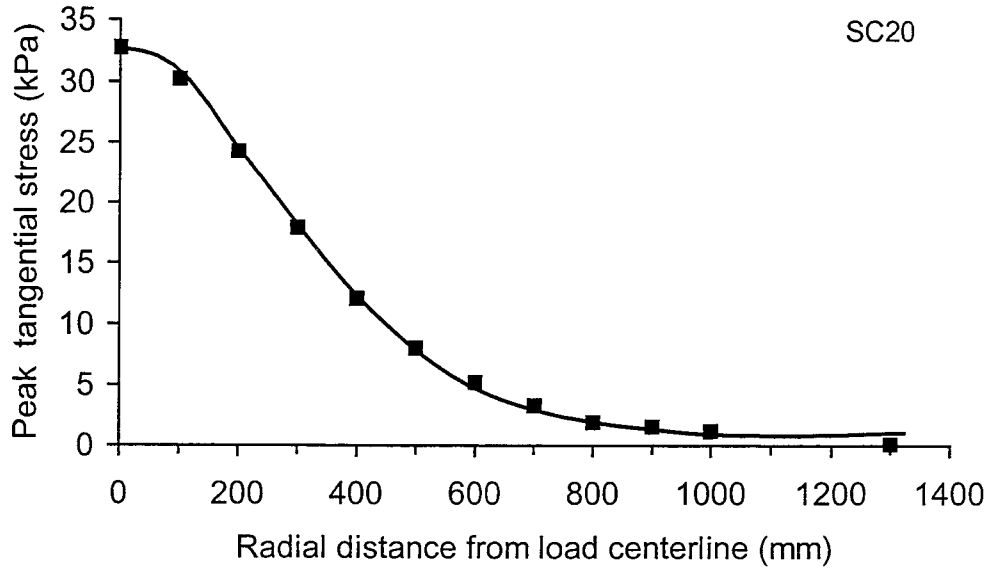

Figure 4.14 Peak tangential stress in the subgrade versus radial distance (PCS1, Z=450 mm).

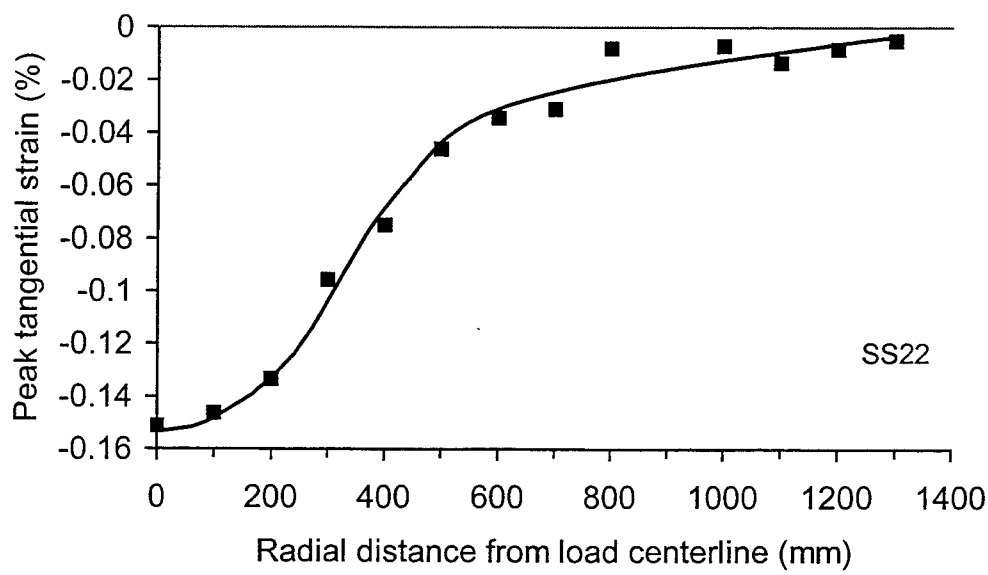

Figure 4.15 Peak tangential strain in the subgrade versus radial distance (PCS1, Z=415 mm).

5.0 PAVEMENT TEST SECTION RESULTS

This section presents results from test sections CS2, CS5-CS11, SSS1-SSS4 and selected results from SSS5 through SSS9. Results from sections CS2 and CS3 are not presented for reasons described in Section 3.5 (pg. 46). Only selected results from sections SSS5-SSS9 are presented due to the quality of the sections that could be achieved using cold-mix AC. Results are grouped and presented to illustrate reinforcement mechanisms described in Section 2. This is accomplished by presenting data that supports improvements in lateral spreading of the base and subgrade and vertical stress distribution on the subgrade. Mechanisms discussed in Section 2 that have not been demonstrated with the measurements made in this work are discussed at the end of this section. A comparison is made between the clay subgrade control sections with 300 mm of base (CS2 and CS8) and the clay subgrade section with 375 mm of base to illustrate the types of mechanical improvement realized by the addition of base course aggregate.

5.1 Clay Subgrade (CS) Test Sections

5.1.1 Rutting Behavior

This section provides results from the clay subgrade test sections that describe overall performance in terms of surface deformations. Figure 5.1.1 shows the development of permanent surface deformation with applied load cycle. Permanent surface deformation was determined as the average of the two interior-most LVDT's extending through the load plate. Figure 5.1.2 shows permanent surface deformation for the thicker base course sections CS9 and CS10. Figure 5.1.3 shows traffic benefit ratios (TBR) calculated at every 1 mm of permanent deformation for sections CS5, 6, 7, 9 and 11 as compared to section CS2. Figure 5.1.4 shows TBR values for CS10 as compared to CS9. TBR is defined as the number of load cycles necessary to reach a certain permanent deformation in a section divided by the cycles necessary to reach this same deformation in a comparable control section.

The overall results show a definite and substantial effect of reinforcement on rutting behavior. In light of material discussed in Section 3.5, sections CS2, CS8 and CS6 have very comparable as-constructed material properties. Sections CS7 and CS11 do not have statistically significant differences in material properties as compared to CS2. Section CS5 also does not have statistically significant differences in material properties as compared to CS2 but is a

borderline case. Given the conclusions from this analysis, it is assumed that CS2, CS8, CS6 CS7 and CS11 can be directly compared for purposes of making conclusions on reinforcement behavior. Given the significance of asphalt air voids on overall behavior, it is believed that CS5 would have performed better had its AC air voids been closer to that of CS2 and would have most likely performed better than CS7.

Figure 5.1.1 shows that all the geosynthetic products used provided a performance benefit as measured by rut development. The two geogrid products used provided improvement that was superior to the geotextile product selected. This should not be interpreted to mean that all geogrid products will be superior to all geotextile products in this application, but simply that the characteristics of the geogrid and geotextile products used in this research were such that superior performance was seen with the geogrids. These characteristics include intrinsic material properties of the geosynthetic and shear-interaction properties of the geosynthetic with surrounding soil. Further discussion of this point is made in this section in light of stress and strain data collected from the test sections.

Comparison of CS11 and CS5 suggests that with all other factors being equal, an increase in stiffness and strength of the geosynthetic results in superior pavement performance. Comparison of CS11 and CS7 indicates that placement position of the geosynthetic in the base course layer has a significant impact on pavement performance. In this particular case, placing the geogrid 100 mm up into the 300 mm thick base provided superior performance to placing the same geogrid at the interface. These results suggest that the improvement seen by moving geogrid A 100 mm up into the base was superior to placing the stiffer geogrid B at the interface. In light of the statistical analysis performed in Section 3.5, it is believed that section CS5 would have performed as good and most likely better than CS7 had the AC air voids in CS5 been equivalent to CS7. Nevertheless, placement position and geosynthetic stiffness both appear to be important parameters.

Figure 5.1.3 shows that maximum TBR values for sections CS5, CS6, CS7 and CS11 ranged from 8 to 56. Figure 5.1.1 shows that section CS6 initially developed permanent deformation similarly to the unreinforced sections (CS2 and CS8) and began to perform better than the control sections at a rut depth of approximately 6-7 mm. Figure 5.1.3 also shows this where it is seen that TBR is less than or equal to one up to a rut depth of 6 mm. In contrast, the geogrid reinforced sections perform similarly up to a rut depth of 5 mm. TBR values for the

geogrid reinforced sections are in the range of 7 to 25 for the first 1 mm of permanent rut development, illustrating that the effect of reinforcement is immediate and that in general, excessive rutting of the roadway is not required to mobilize reinforcement.

A comparison of CS9 and CS10 in Figure 5.1.2 also shows a significant improvement due to reinforcement, although not quite as great as with the thinner base course layer. Figure 5.1.4 further illustrates this point where a maximum TBR of 14 is seen. This may imply that with a thicker base and with the geosynthetic further away from the applied load, additional rutting is required to mobilize the reinforcement and that the effects of reinforcement diminish as the base thickness increases over some threshold value. Additional rutting needed to mobilize reinforcement results from a downward progression of shear flow in the base that is necessary before base aggregate begins to interact with the geogrid and does not imply that higher deformations are needed to mobilize a membrane type of reinforcement function. These results also suggest that moving the geogrid up higher in the base would have provided better performance in this situation.

Closer examination of Figure 5.1.1 for rut depths less than 5 mm shows that while initial rut development is relatively rapid, the majority of the initial rut development does not take place within the first several load cycles. For instance, the two control sections reached a rut depth of 5 mm in 110 cycles, while sections CS6, CS11, CS5 and CS7 reached a rut depth of 5 mm in 200, 3570, 4570 and 5760 cycles, respectively. This indicates that the rate of initial rutting is significantly influenced by reinforcement. It should also be noted that sections CS2, CS8, CS6 and CS11 had the lowest AC air voids. This further supports the statement that reinforcement is responsible for the reduced rate of rutting in the beginning of these tests. It will be shown later in this section that this initial rutting is due to deformation of all layers and not only by compression of air voids in the AC.

Section CS9, which was an unreinforced section with a 375 mm base, is compared to CS2 in Figure 5.1.3 in terms of TBR to illustrate the benefits of an additional 75 mm of base material. In this figure it is seen that an additional 75 mm of base aggregate results in a peak TBR of 3.2. All reinforced sections provide a higher TBR than the addition of 75 mm of base material, indicating that each reinforcement product is equivalent to at least 75 mm of base aggregate. Benefits associated with the addition of 75 mm of base aggregate are further explored in Section 5.1.5.

An examination of the profile of pavement surface deformation, or the deflection bowl, also illustrates reinforcement features. Figures 5.1.5 – 5.1.8 illustrate permanent deflection bowls for initial stages of loading (cycle 1) and later stages of loading for sections with a 300 and 375 mm base course layer. Figures 5.1.6 and 5.1.8 were prepared for 40,000 cycles and 125,000 cycles, respectively. These cycle numbers were chosen because the control sections had reached 25 mm of permanent deformation. Figure 5.1.5 reinforces the argument that initial pavement deformation occurs at a rapid rate, but is very different between the reinforced sections and the control sections. Deformation bowls for the geogrid reinforced sections are clustered together, while the bowl for the geotextile section is more closely comparable to the two control sections. Figure 5.1.7 shows that for the thicker base course sections (CS9, CS10) the reinforced section exhibited a higher level of deformation than the control section for the first load cycle. This is consistent with earlier comments suggesting that more base aggregate shear flow was necessary to mobilize the reinforcement and that optimal performance may have been observed by moving the geogrid up into the base layer. After 40,000 cycles of load, Figure 5.1.6 shows a distinct difference between the control sections and the reinforced sections. The observed consistency between the control sections indicates good quality control in construction.

Figures 5.1.9 and 5.1.10 present results showing dynamic surface deformation for early and later stages of loading. These figures tend to convey the same information as those for permanent deformation, but not to the same degree. This tends to suggest problems with using single-cycle dynamic response as a predictive tool for long-term rutting behavior. Figures 5.1.11 and 5.1.12 show dynamic surface deformation beneath the load plate versus load cycle and reinforce the points made immediately above.

Despite significant differences in the asphalt surface deformation measures just described, the results from the asphalt strain gages placed within the asphalt layer did not yield significant differences between the sections in terms of tensile strains. At this time, it is not clear if these results are a product of poor instrument performance, instrument placement techniques, or that fatigue cracking, as described by tensile strains in the AC layer, was relatively unaffected by the inclusion of reinforcement.

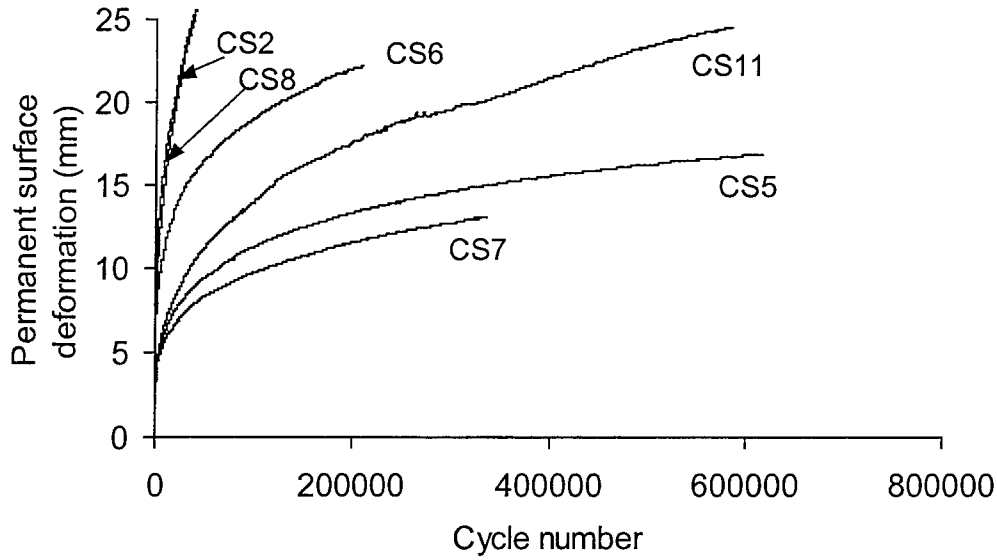

Figure 5.1.1 Permanent surface deformation versus load cycle (CS2-CS11).

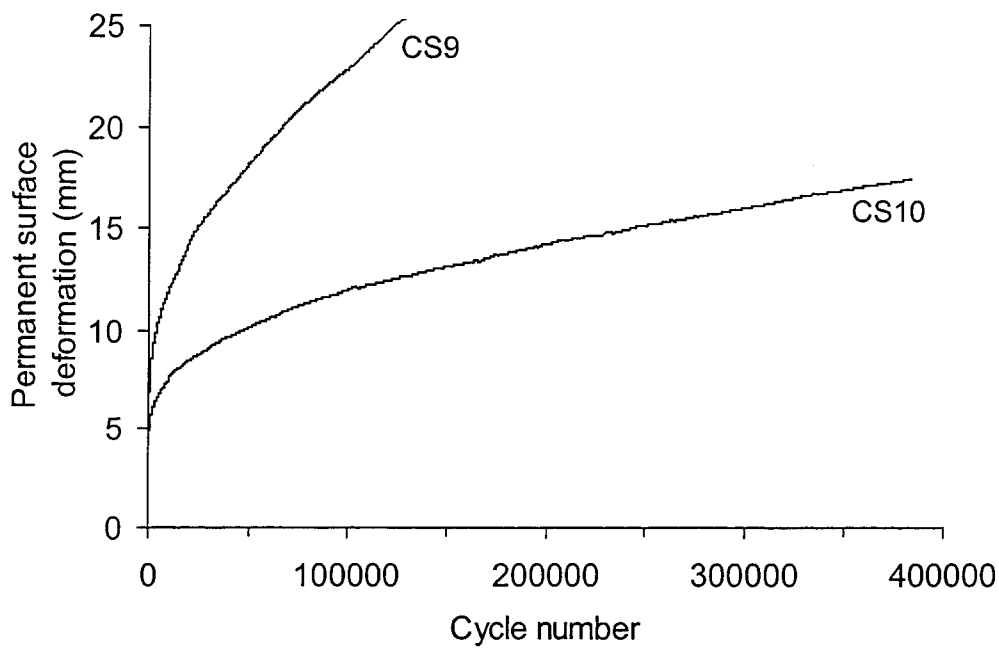

Figure 5.1.2 Permanent surface deformation versus load cycle (CS9, CS10).

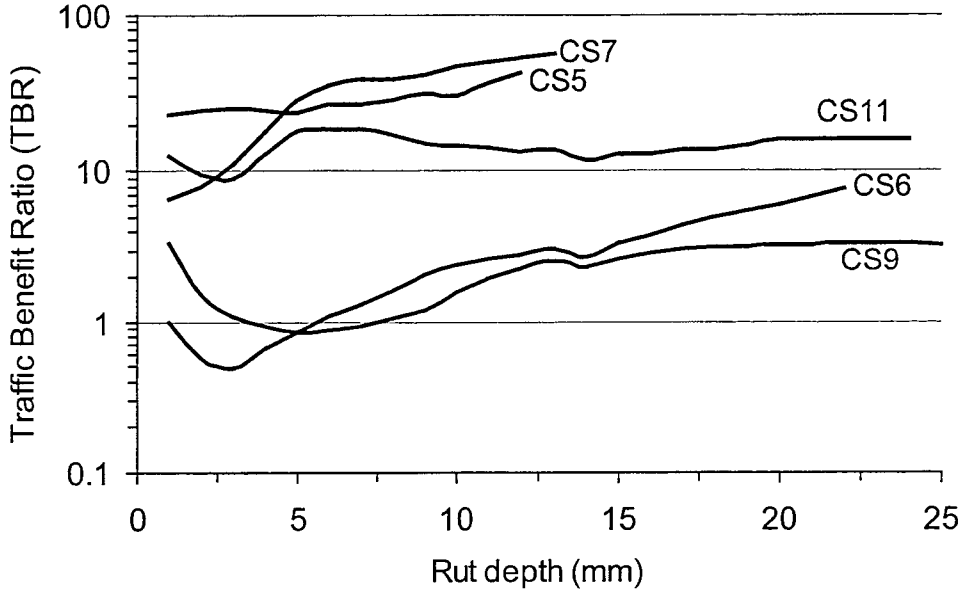

Figure 5.1.3 TBR for sections CS5, 6, 7, 9 and 11 relative to CS2.

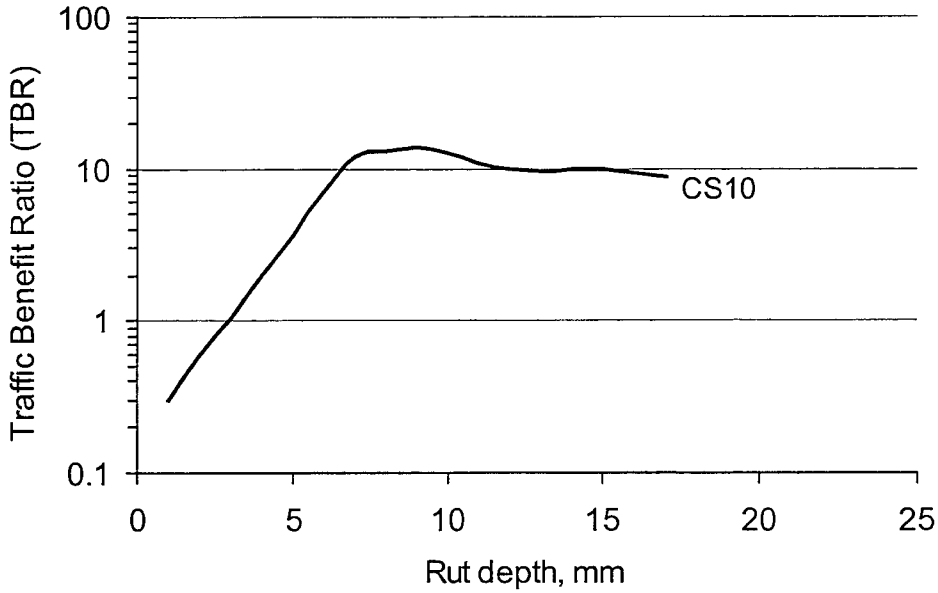

Figure 5.1.4 TBR for section CS10 relative to CS9.

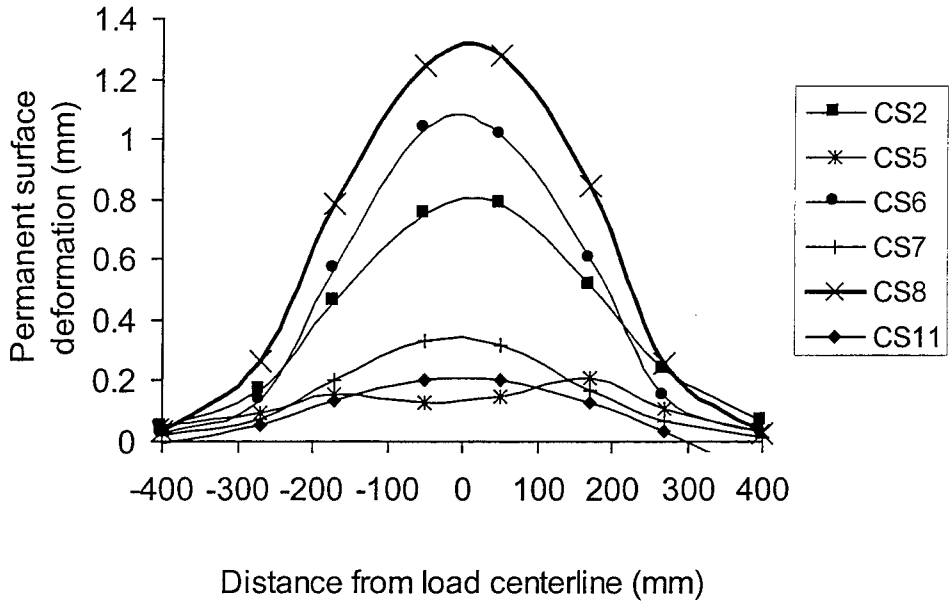

Figure 5.1.5 Permanent surface deformation bowls for cycle 1 (CS2-CS11).

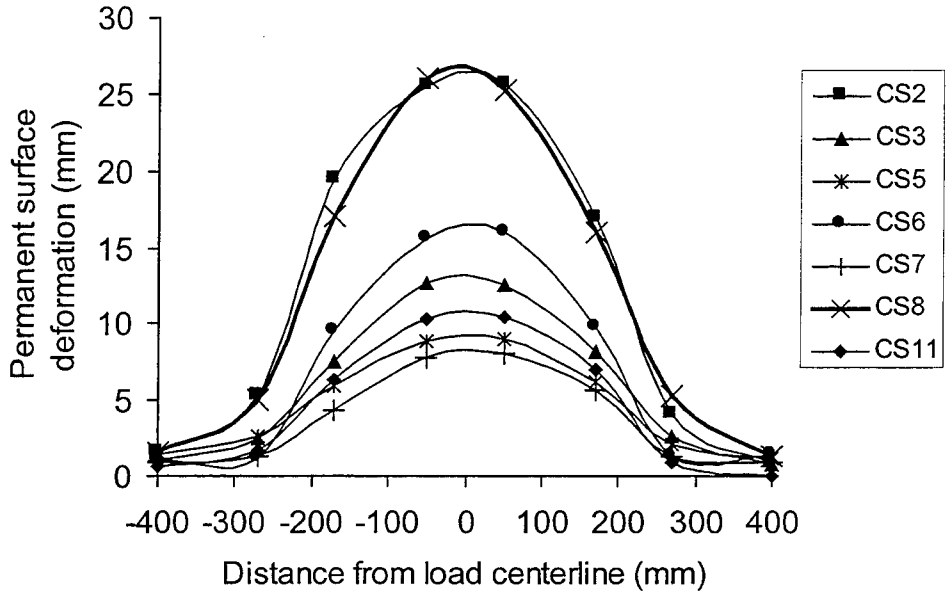

Figure 5.1.6 Permanent surface deformation bowls at cycle 40,000 (CS2-CS11).

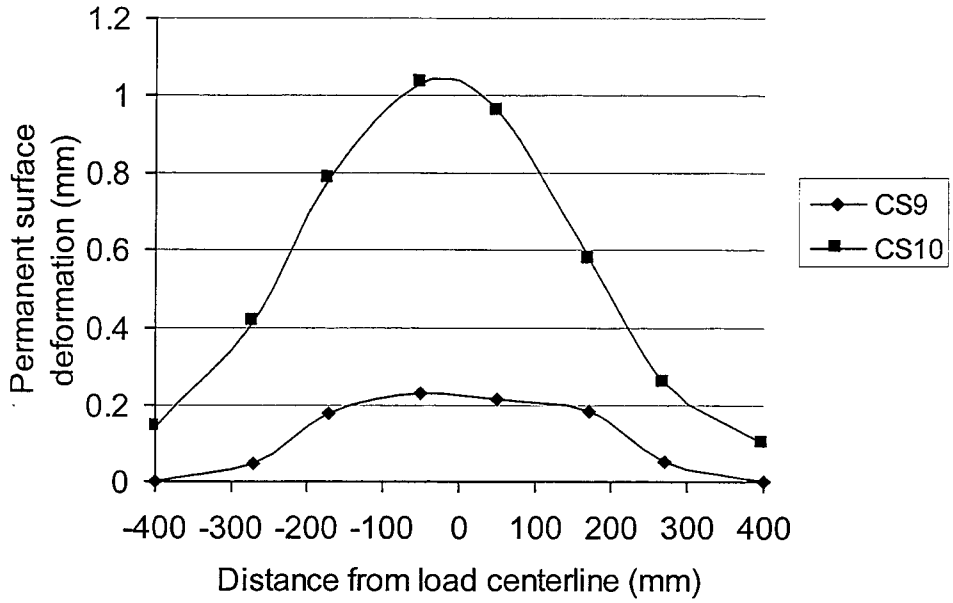

Figure 5.1.7 Permanent surface deformation bowls for cycle 1 (CS9, CS10).

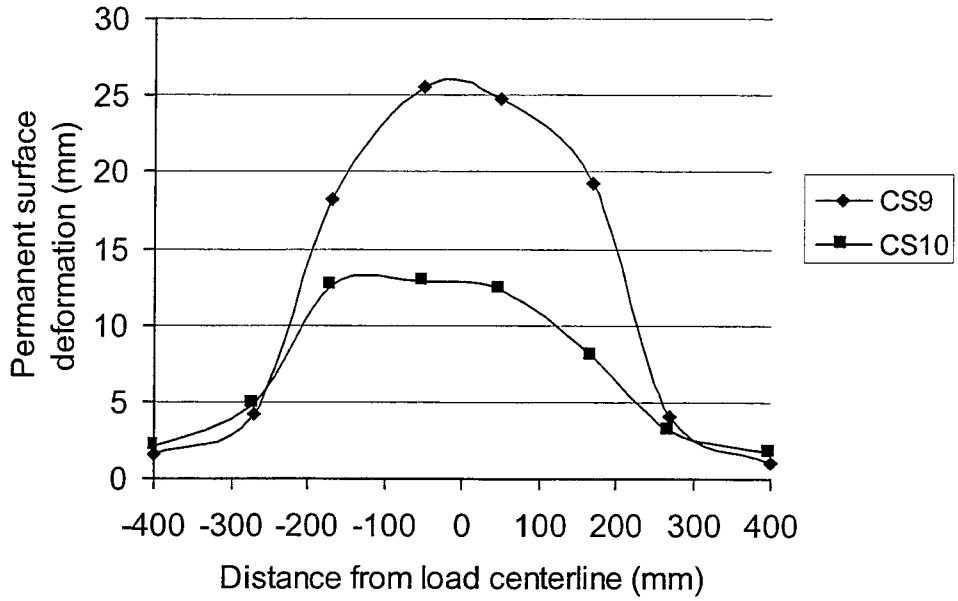

Figure 5.1.8 Permanent surface deformation bowls at cycle 125,000 (CS9, CS10).

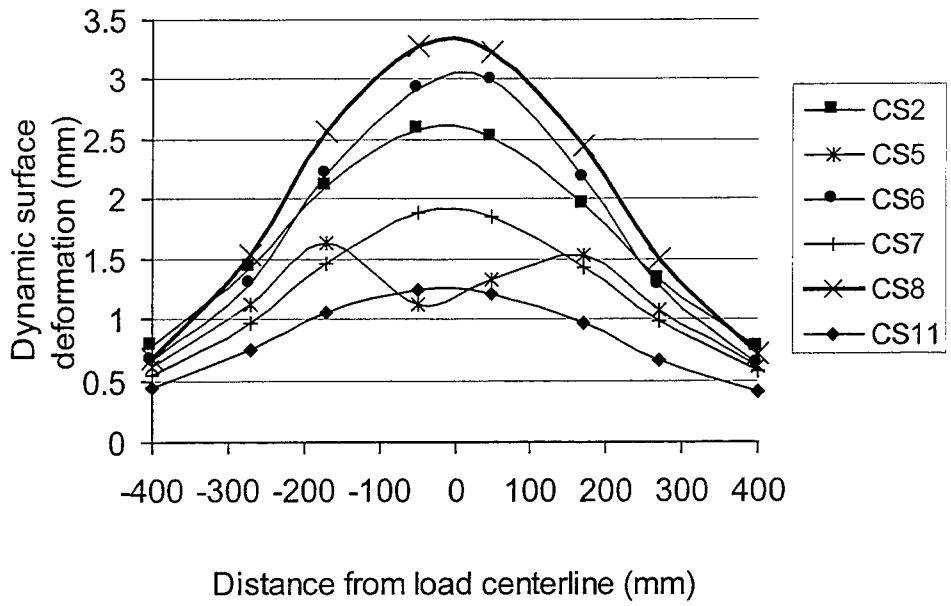

Figure 5.1.9 Dynamic surface deformation bowls for cycle 1 (CS2-CS11).

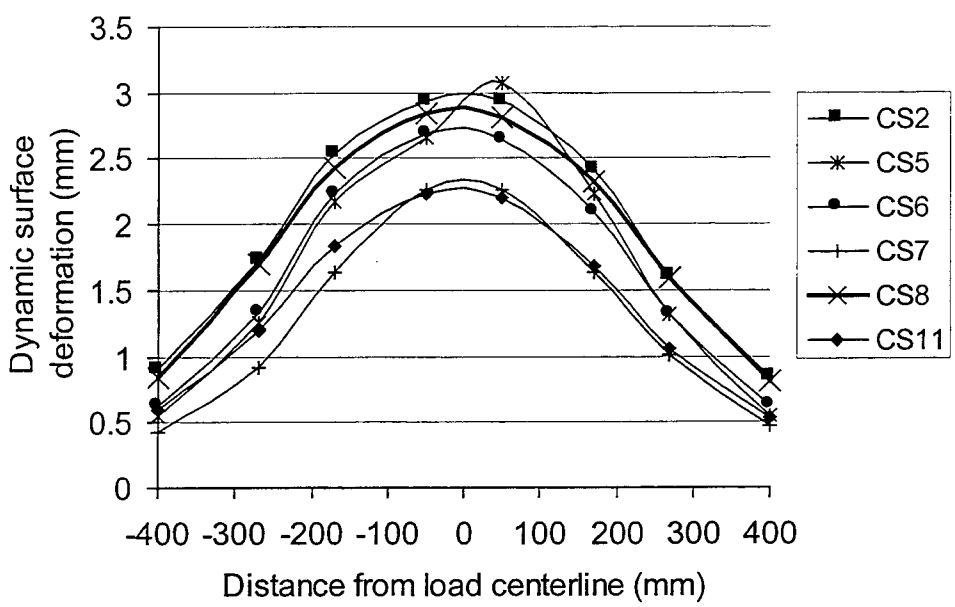

Figure 5.1.10 Dynamic surface deformation bowls at 12.5 mm permanent deformation (CS2-CS11).

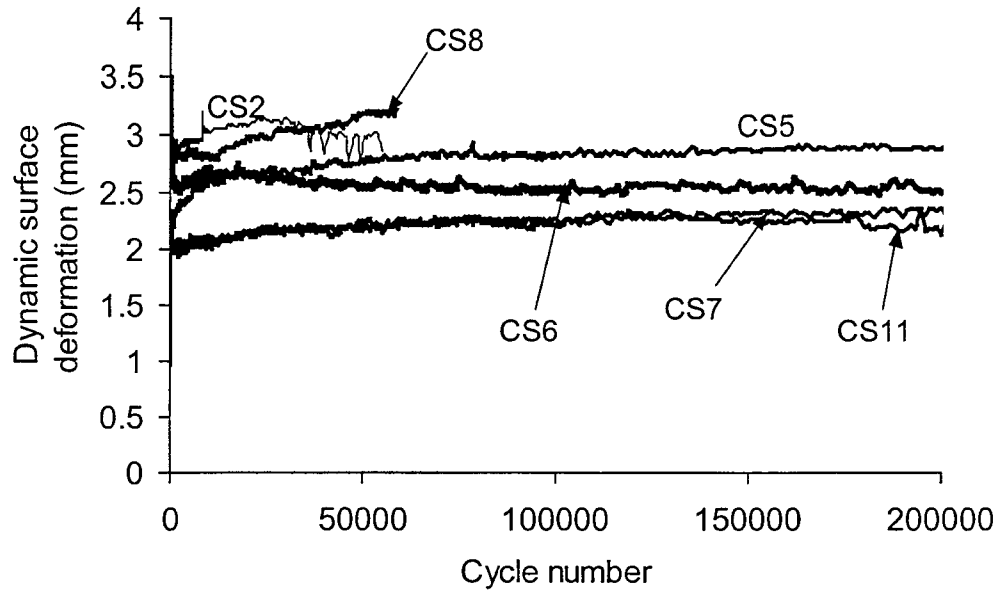

Figure 5.1.11 Dynamic surface deformation versus load cycle (CS2-CS11).

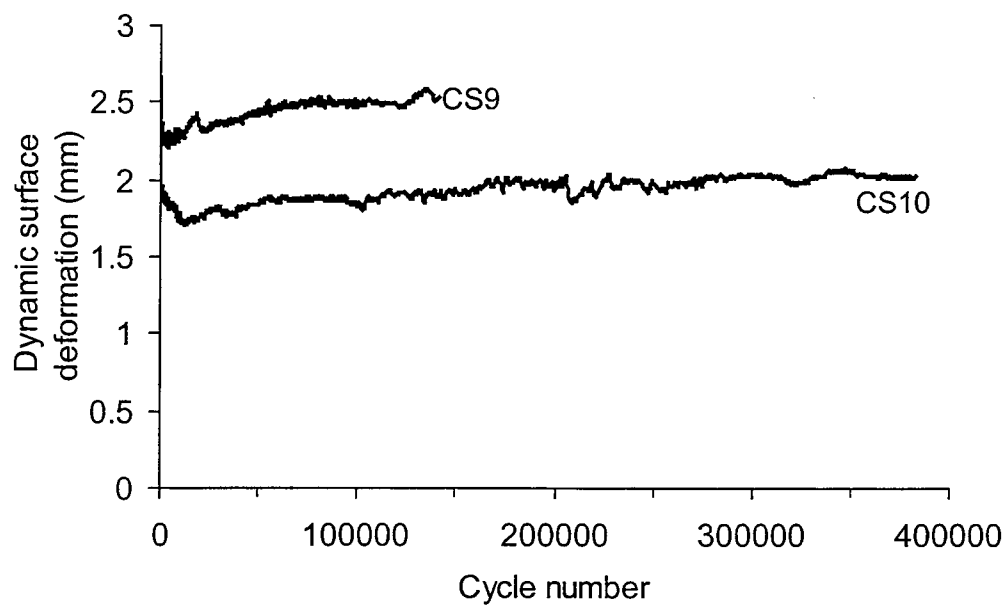

Figure 5.1.12 Dynamic surface deformation versus load cycle (CS9, CS10).

5.1.2 Lateral Base Course Restraint

In Section 2, a possible reinforcement mechanism described was the prevention of lateral movement of the base course aggregate though the development of shearing resistance with the geosynthetic. In this section, data is presented to support the existence of this mechanism. Figures 5.1.13 and 5.1.14 show the permanent radial strain developed in the bottom of the base approximately 50 mm above the geosynthetic. It is seen in Figure 5.1.13 that all sections develop tensile strain at a radius of 100 mm, with the unreinforced sections (CS2 and CS8) exhibiting considerably more strain than the reinforced sections. Radial strain development in the reinforced sections is similar, suggesting that adequate shear-interaction is developed between the base aggregate and the geosynthetics. CS6 exhibits initially greater lateral strain comparable to the control sections, but only for the first 7-8 load cycles. This suggests that the overall difference in rutting behavior between CS6 and the other sections is not due to differences in this reinforcement mechanism.

At 200 mm from the load centerline, Figure 5.1.14 illustrates that the control sections CS2 and CS8 show compressional strains, while the reinforced sections show extensional strains. Reinforced sections are closely grouped in this figure. Figures 5.1.15 and 5.1.16 further illustrate changes in radial strain development in the bottom of the base between reinforced and control sections. The data shows that the reinforcement allows the base at this level to remain in extension for effectively all radii and prevents the large gradient between extension and compression from developing as seen in the unreinforced sections. Figure 5.1.15 also shows that this effect is immediate upon the first application of load. These figures clearly illustrate the ability of the geosynthetic to prevent lateral movement of the base aggregate. Figure 5.1.16 also suggests that the ranking of this effect correlates with overall performance of the test sections.

Figures 5.1.17 and 5.1.18 illustrate a similar reinforcement effect for the 375 mm base course sections. Figure 5.1.19 shows that the lateral base course restraint is also exhibited by the measure of dynamic radial strain. The dynamic radial strains appear to correlate reasonably well to long-term rutting behavior of the sections, however the relationship is not exact.

A manifestation of lateral base restraint is the development of significant tensile strain in the geosynthetics. Figures 5.1.20 and 5.1.21 show significant development of permanent strain directly beneath the load in the machine and cross-machine directions of the geosynthetics. The magnitude of permanent strain in the geosynthetic does not necessarily correlate with long-term

performance of the sections. This is to be expected since the development of permanent strain in the geosynthetic is dependent on material properties of the geosynthetic along with soil-geosynthetic interaction properties. Figure 5.1.22 illustrates a profile of permanent strain in the geosynthetics versus radial distance in the machine direction at 7500 cycles of load. This load cycle level was chosen since after this level, some foil gages become inoperable. These results illustrate a pattern of strain development that is similar to that proposed and shown in Figure 2.1. The data shows that significant permanent strain is developed in the area beneath the load plate where greatest lateral movement of the base occurs.

Figures 5.1.23 and 5.1.24 show that permanent strain accumulates under relatively constant dynamic strain for each load cycle. Figures 5.1.25 and 5.1.26 show profiles of dynamic strain in the radial direction of the reinforcement for one cycle of load and after 7500 cycles of load. Constant dynamic strain in the geosynthetics implies that the dynamic load induced in the geosynthetics is also nearly constant. Figure 5.1.25 also shows that strain is induced immediately in the geosynthetic indicating that reinforcement is also immediate.

The accumulation of permanent strain under nearly constant dynamic strain or load has several implications for material modeling. This data may imply that incremental creep strain develops under this loading condition. On the other hand, the geosynthetic may be responding to the incremental permanent strain developed in the base course adjacent to the geosynthetic.

The dynamic strains seen in Figures 5.1.23 and 5.1.24 can be used to compute dynamic load induced in the geosynthetic. Elastic moduli for geogrid A and the geotextile were determined from the uniaxial tension tests described in Section 3.2.2. Multiplying these moduli by the dynamic strains seen in Figures 5.1.23 and 5.1.24 gives the loads listed in Table 5.1.1. It is shown that line loads of up to 2.6 kN/m are developed in section CS11 and that loads up to 1.4 kN/m were developed in the geotextile. The development of loads of this magnitude indicate that significant load is transferred from the soil to the geosynthetic.

Figure 5.1.27 shows that the lateral base course restraint mechanisms described in this section results in a reduction of permanent vertical strain in the base layer. Additionally, with the exception of CS5, the reinforced sections are grouped closely, indicating that although greater differences existed with lateral strains, the impact on the differences in vertical base strain is much less significant. It is noted that section CS6 is not much different from other sections and that base movement is apparently not the cause of the decreased performance.

Table 5.1.1 Dynamic load induced in the geosynthetics.

Section	Direction	Elastic Moduli (kN/m)	Dynamic Strain (%)	Dynamic Load (kN/m)
CS7	MD	600	0.3	1.8
	XMD	645	0.2	1.3
CS11	MD	600	0.43	2.6
	XMD	645	0.35	2.3
CS6	MD	239	0.15	0.4
	XMD	960	0.15	1.4

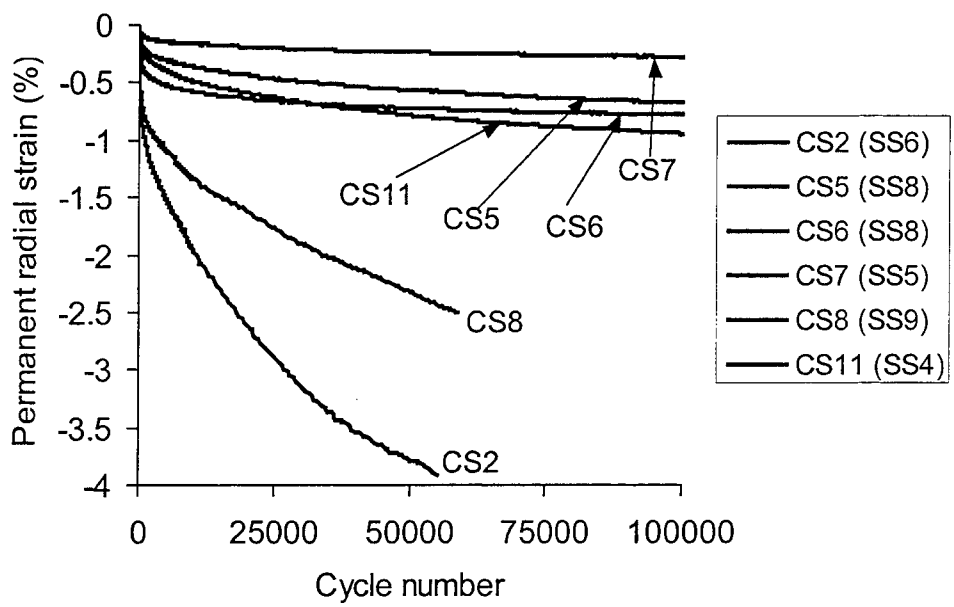

Figure 5.1.13 Permanent radial strain in the base versus load cycle (CS2-CS11, R=100 mm, Z=325 mm).

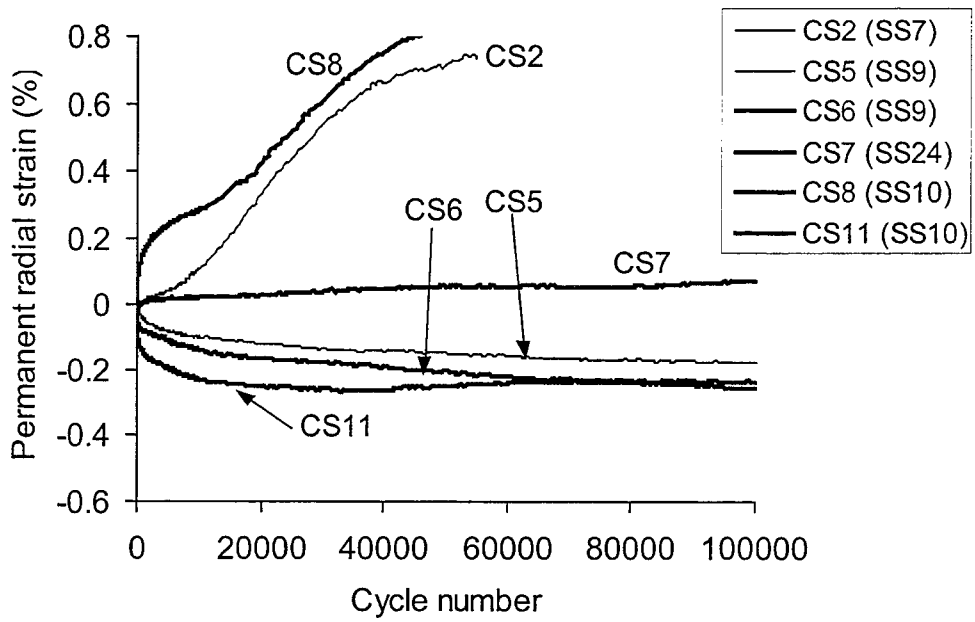

Figure 5.1.14 Permanent radial strain in the base versus load cycle (CS2-CS11, R=200 mm, Z=325 mm).

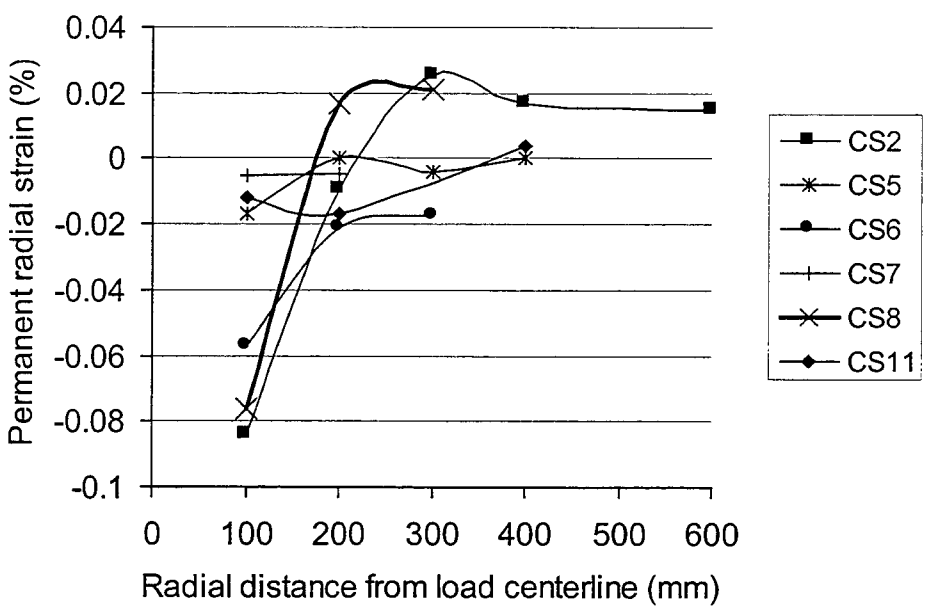

Figure 5.1.15 Permanent radial strain in the base versus radial distance for cycle 1 (CS2-CS11, Z=325 mm).

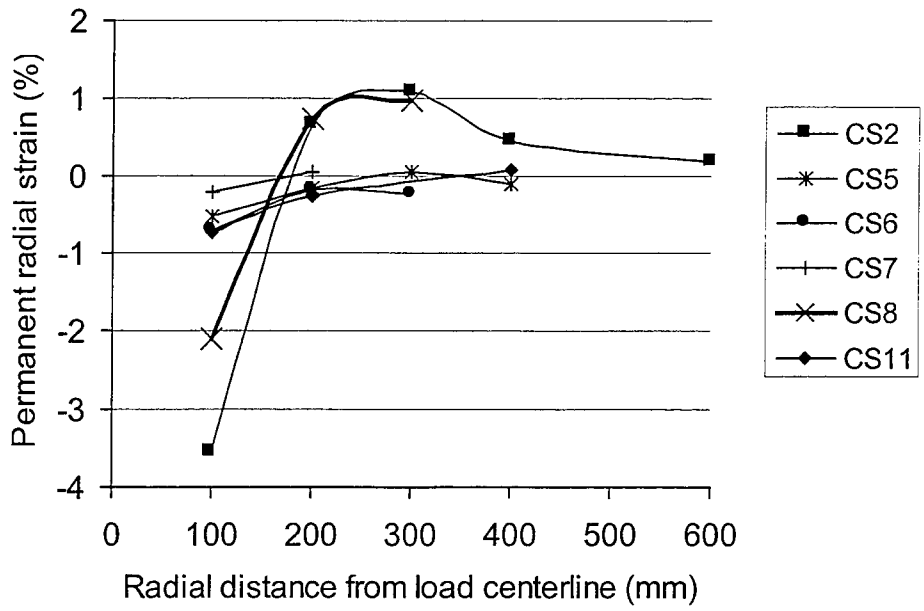

Figure 5.1.16 Permanent radial strain in the base versus radial distance at cycle 40,000 (CS2-CS11, Z=325 mm).

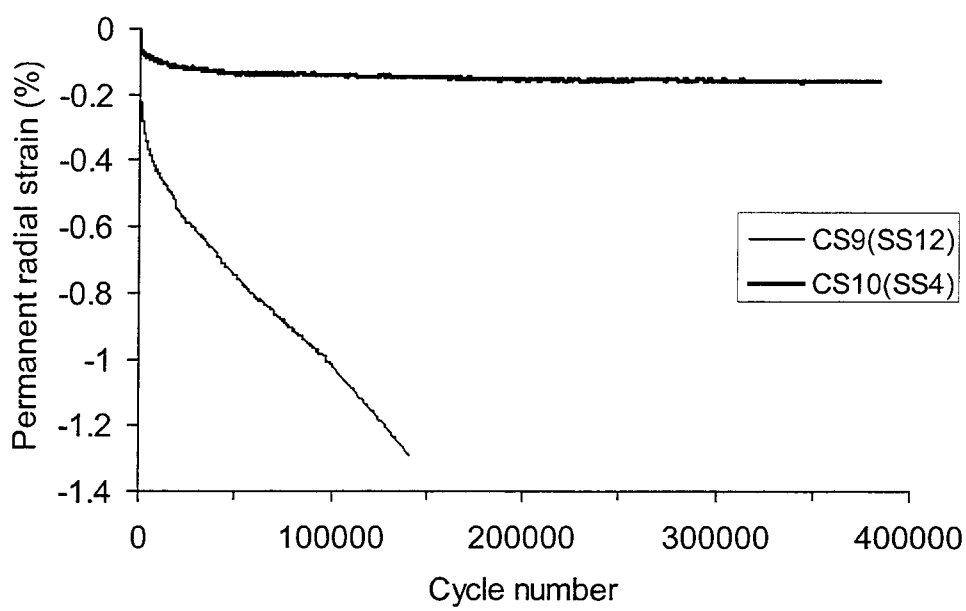

Figure 5.1.17 Permanent radial strain in the base versus load cycle (CS9, CS10, R=100 mm, Z=400 mm).

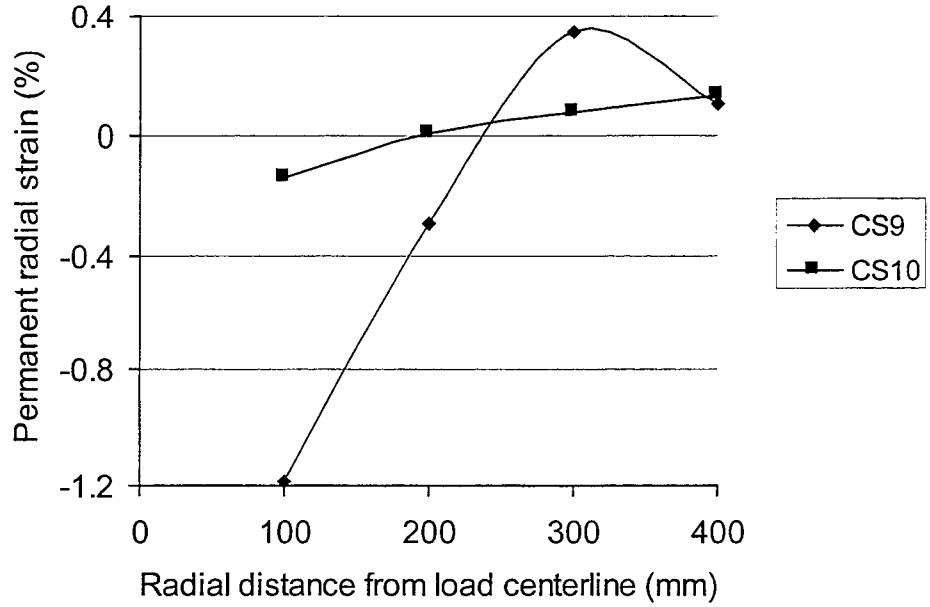

Figure 5.1.18 Permanent radial strain in the base versus radial distance at cycle 125,000 (CS9, CS10, Z=400 mm).

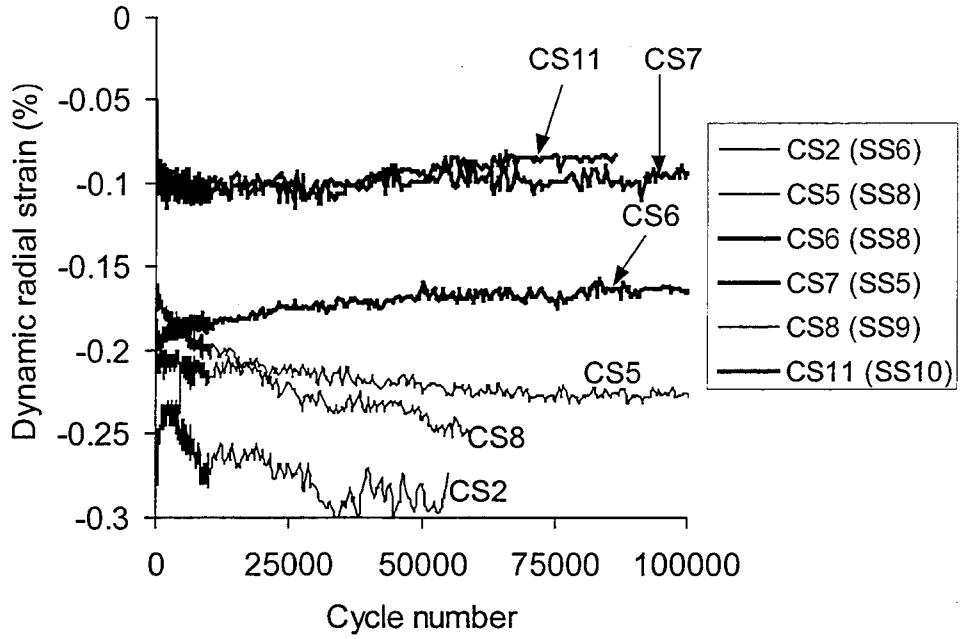

Figure 5.1.19 Dynamic radial strain in the base versus load cycle (CS2-CS11, R=100 mm, Z=325 mm).

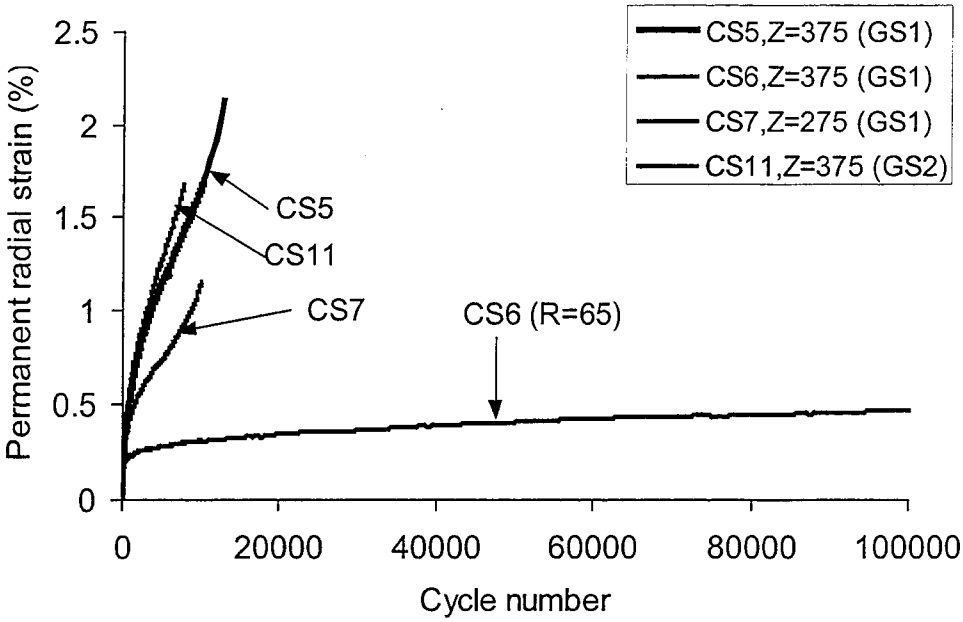

Figure 5.1.20 Permanent radial strain in the geosynthetics (M) versus load cycle (CS5-CS11, R=15 mm).

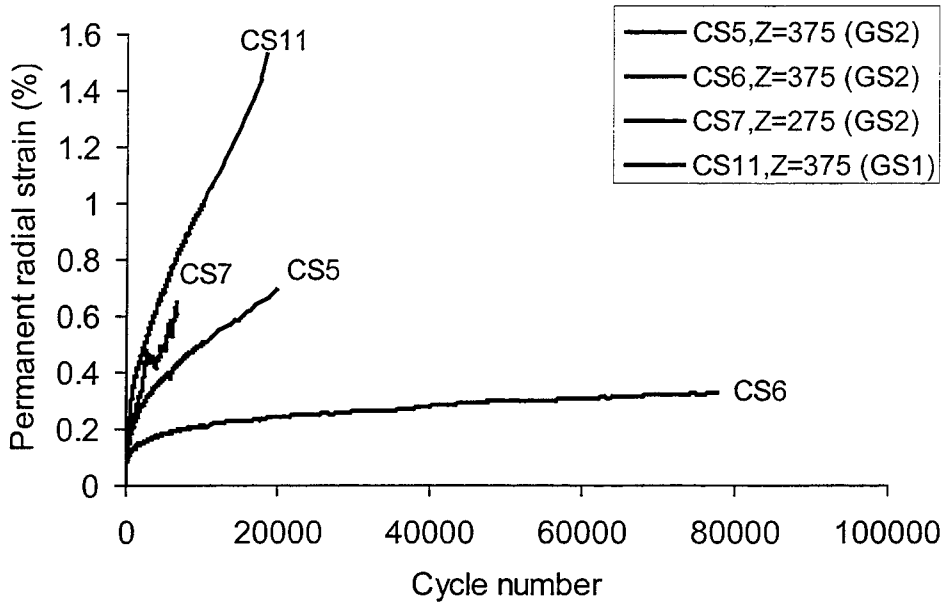

Figure 5.1.21 Permanent radial strain in the geosynthetics (XM) versus load cycle (CS5-CS11, R=20 mm).

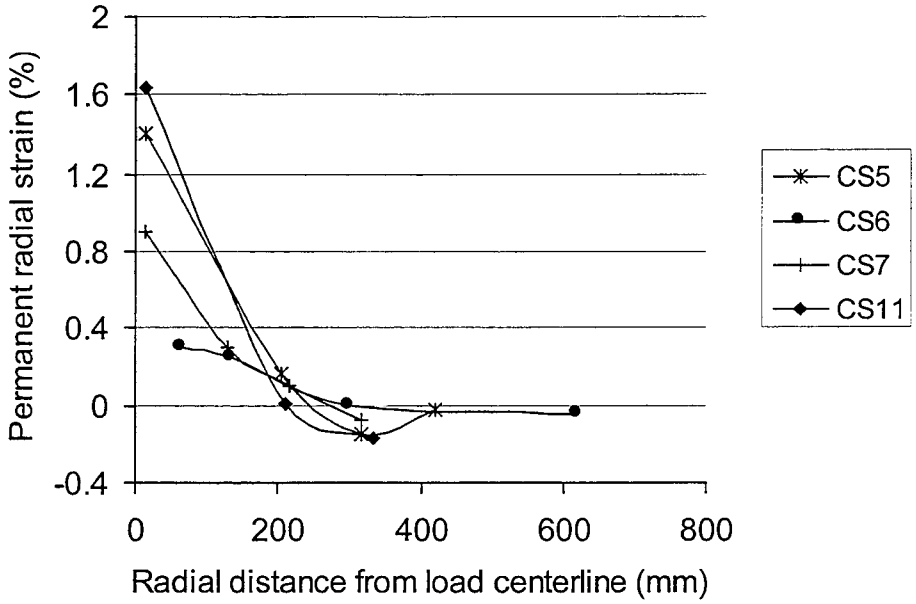

Figure 5.1.22 Permanent radial strain in the geosynthetics (M) versus radial distance at cycle 7500 (CS5-CS11).

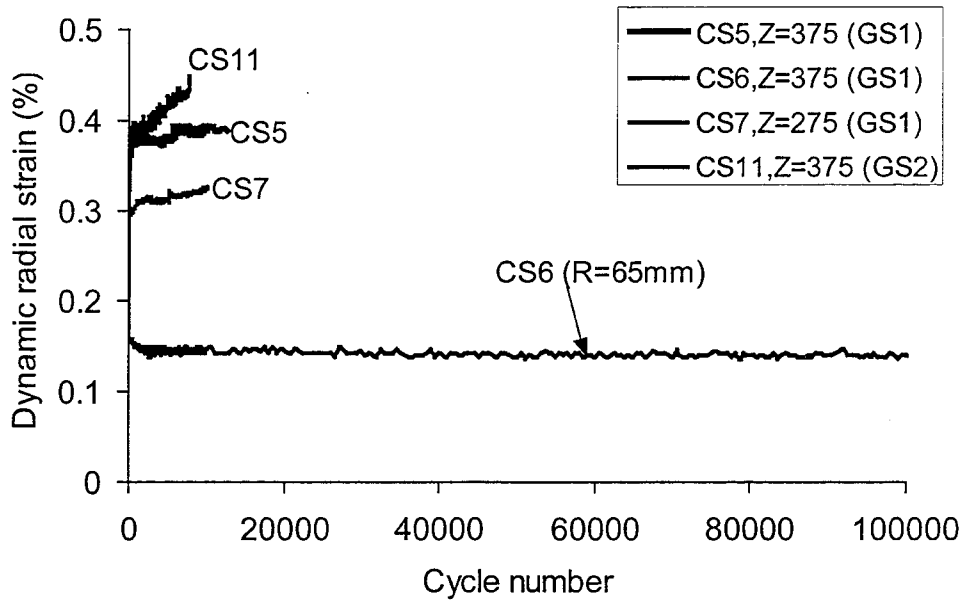

Figure 5.1.23 Dynamic radial strain in the geosynthetics (M) versus load cycle (CS5-CS11, R=15 mm).

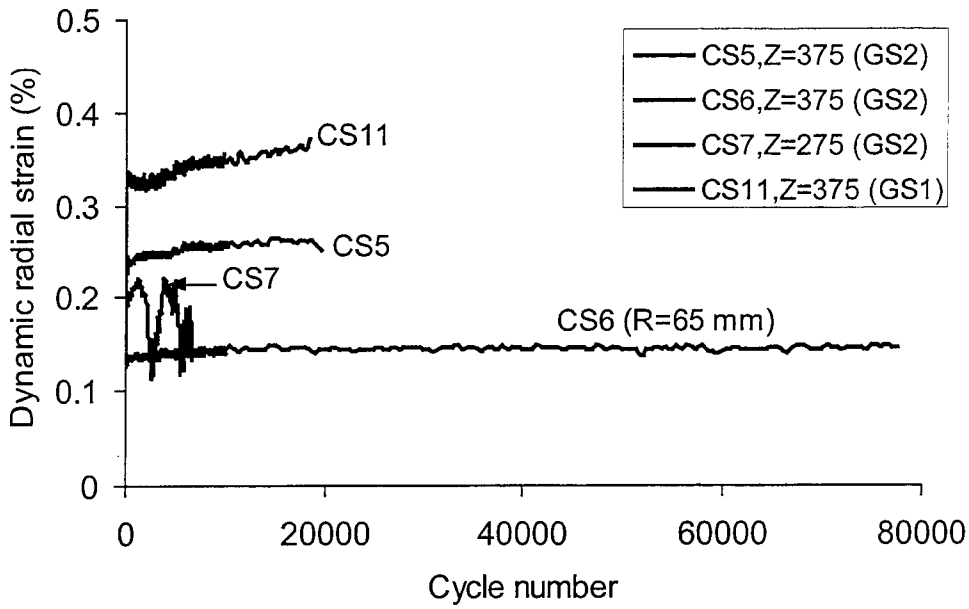

Figure 5.1.24 Dynamic radial strain in the geosynthetics (XM) versus load cycle (CS5-CS11, R=20 mm).

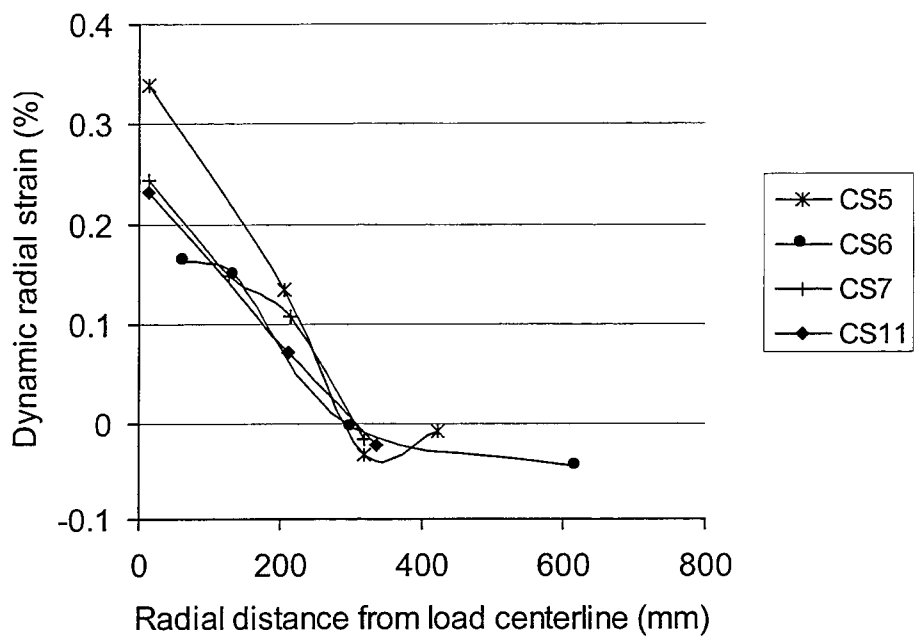

Figure 5.1.25 Dynamic radial strain in the geosynthetics (M) versus radial distance for cycle 1 (CS5-CS11).

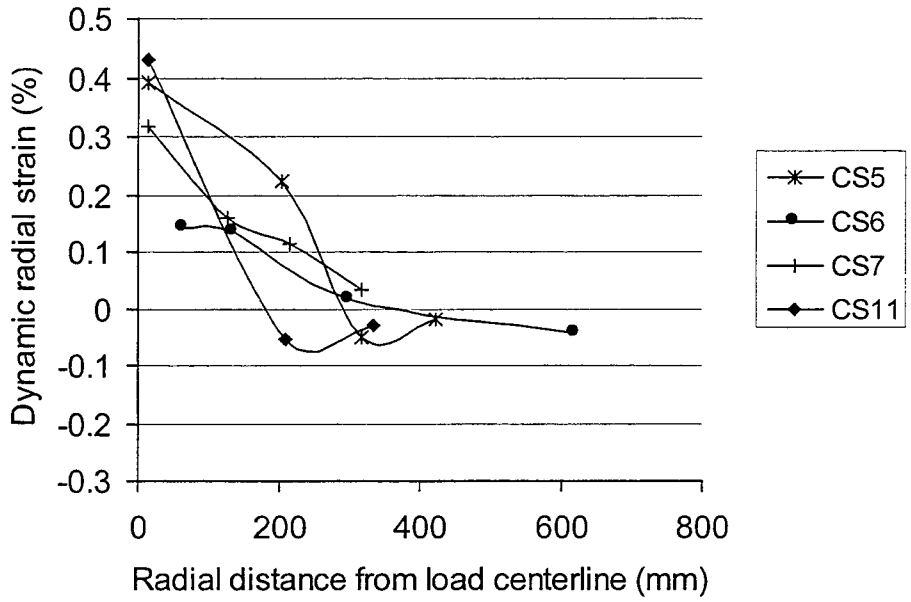

Figure 5.1.26 Dynamic radial strain in the geosynthetics (M) versus radial distance at cycle 7500 (CS5-CS11).

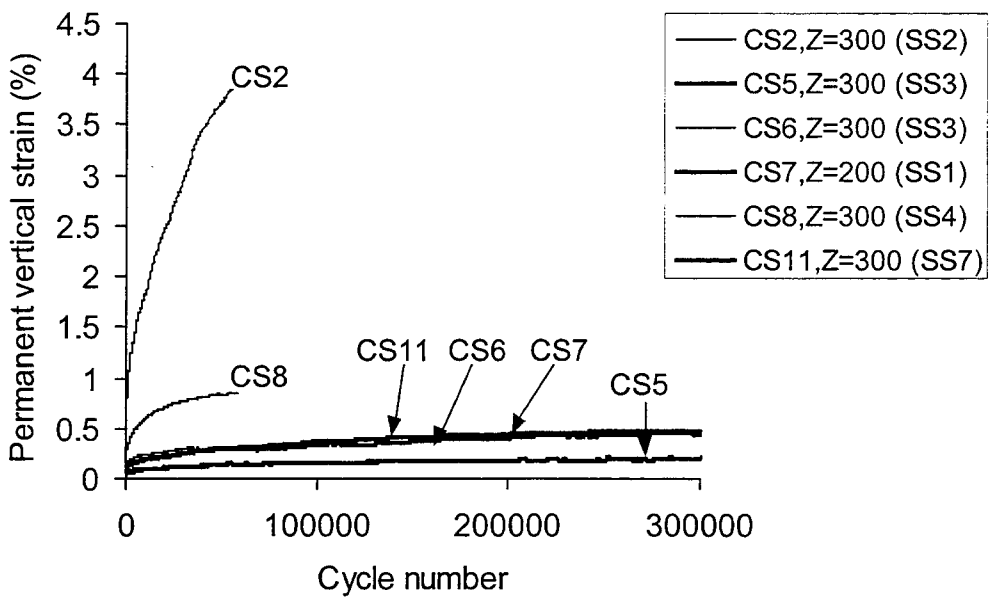

Figure 5.1.27 Permanent vertical strain in the base versus load cycle (CS2-CS11, R=65 mm).

5.1.3 Improved Subgrade Vertical Stress Distribution

Figures 5.1.28 - 5.1.31 show the dynamic vertical stress induced at four levels in the subgrade directly beneath the load plate centerline. The reinforced sections are seen to have a lower dynamic vertical stress at all levels except the bottom most level where the dynamic stresses are on the order of 20 kPa. This data indicates that the greatest improvement in vertical stress for this pavement configuration occurs in approximately the top 300 mm of the subgrade. Figure 5.1.28 also shows that the section with the geotextile (CS6) shows a greater vertical stress than the other reinforced sections.

Figure 5.1.32 shows a distribution of vertical stress across the top of the subgrade after 40,000 load cycles. Improved load spreading is seen with the reinforced sections, while the section with the geotextile reinforcement did not provide the same level of improvement in load spreading as the other sections reinforced with the two geogrids. As with other reinforcement effects, improved load spreading was seen to occur immediately upon load application.

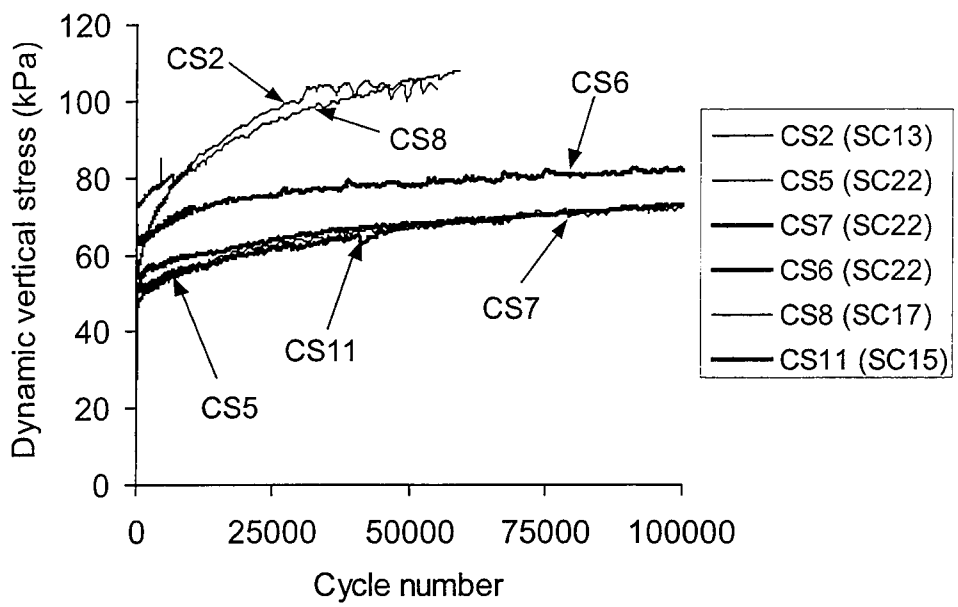

Figure 5.1.28 Dynamic vertical stress in the subgrade versus load cycle (CS2-CS11, R=0, Z=450 mm).

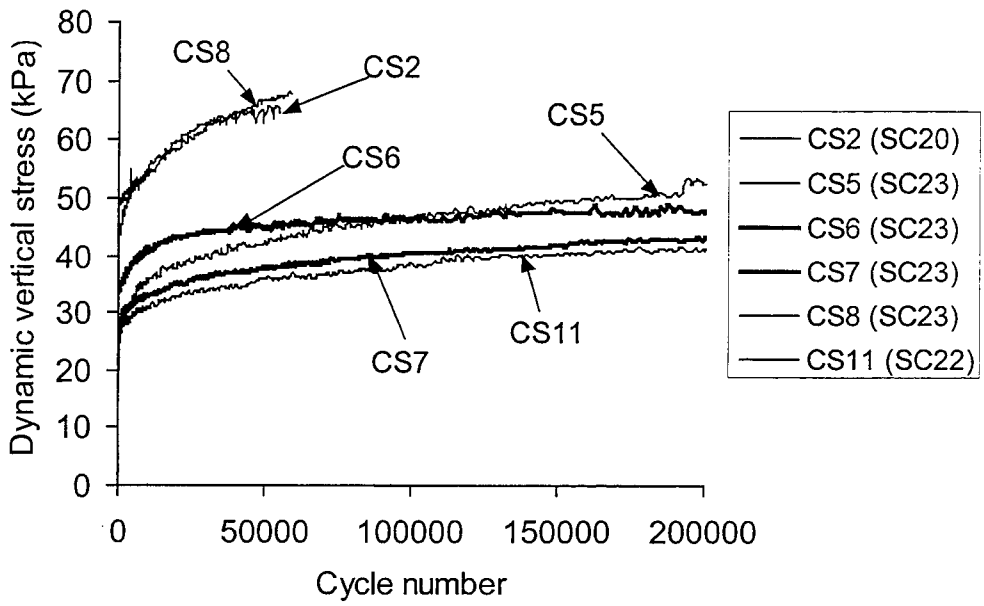

Figure 5.1.29 Dynamic vertical stress in the subgrade versus load cycle (CS2-CS11, R=0, Z=625 mm).

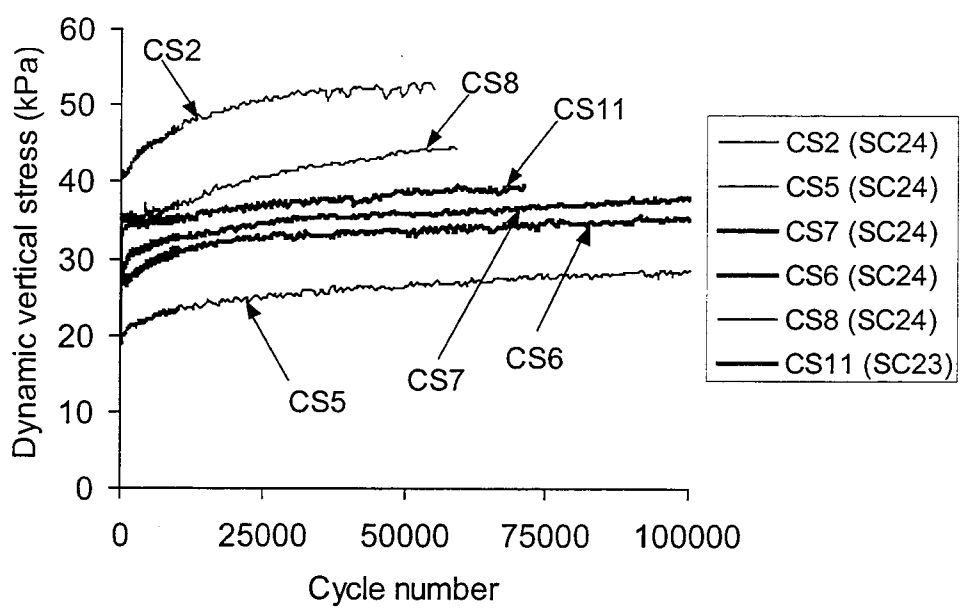

Figure 5.1.30 Dynamic vertical stress in the subgrade versus load cycle (CS2-CS11, R=0, Z=775 mm).

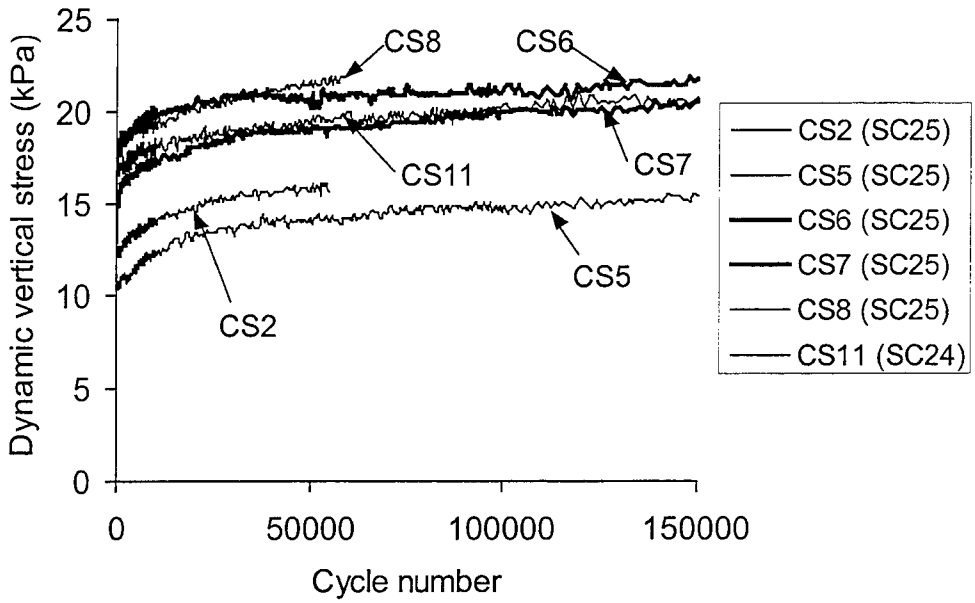

Figure 5.1.31 Dynamic vertical stress in the subgrade versus load cycle (CS2-CS11, R=0, Z=1075 mm).

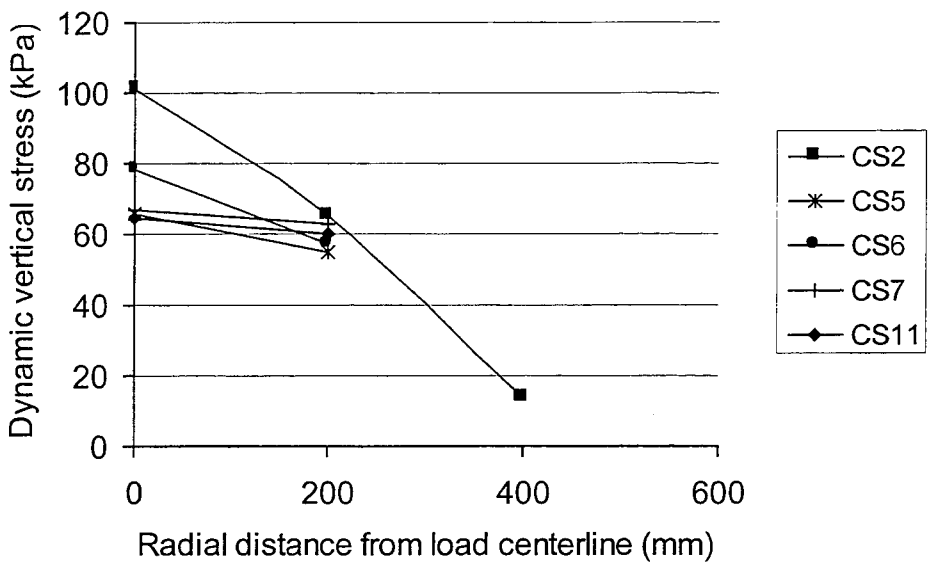

Figure 5.1.32 Dynamic vertical stress in the subgrade versus radial distance at cycle 40,000 (CS2-CS11, Z=450 mm).

5.1.4 Reduced Lateral Spreading of Subgrade

In Section 2, it was speculated that a layer of geosynthetic reinforcement would reduce the shear stress transmitted from the base layer to the subgrade. Shear stress created in the bottom of the base layer is intercepted and carried by the geosynthetic as interface friction develops between the two materials. As a result, less shear stress is experienced in the materials below the geosynthetic. A reduction in shear stress results in a less severe loading condition and as a result, less vertical strain will be developed. The instrumentation used in this study is not able to measure shear stresses in the soil layers. It is expected, however, that reduced shear stress will result in less shear strain which in turn will result in lower radial strain.

Figures 5.1.33 and 5.1.34 show a profile of radial strain in the top of the subgrade versus radial distance for load cycles 1 and 40,000, respectively. These results show a pattern of radial strain in the unreinforced sections that is similar to that developed in the bottom of the base. The presence of reinforcement significantly reduces both extensional and compressional strains. No clear differences between the reinforced sections is exhibited by this data. Similar to other findings, Figure 5.1.33 shows that this effect is also immediate. Figure 5.1.35 shows a similar level of improvement for the thicker base course sections and also shows that radial strains in the top of the subgrade are less than those in the unreinforced sections with the thinner base layer. Figure 5.1.36 shows a measure of dynamic radial stress in the top of the subgrade for the thicker base course sections where it is seen that radial stress is less for the reinforced section. This result indicates that less shoving is taking place in the top of the subgrade when reinforcement is included. Other radial strain measurements were not taken deeper in the subgrade, making it impossible to comment on how deep into the subgrade this effect extends.

The result of an improved vertical stress distribution on the subgrade and reduced radial strain and stress in the top of the subgrade is a reduction of permanent vertical strain. Figures 5.1.37 and 5.1.38 show the permanent vertical strain developed in the top of the subgrade beneath the load plate centerline for the 300 mm and 375 mm base course sections, respectively. The reinforced sections show considerably less vertical strain than the unreinforced sections. In addition, section CS6 shows more vertical strain than the other sections reinforced with geogrids. Given that the data for radial strain in the top of the subgrade shows similar effects between the geogrid and geotextile sections, the difference in vertical strain is most likely due to differences seen in the load spreading characteristics of these materials.

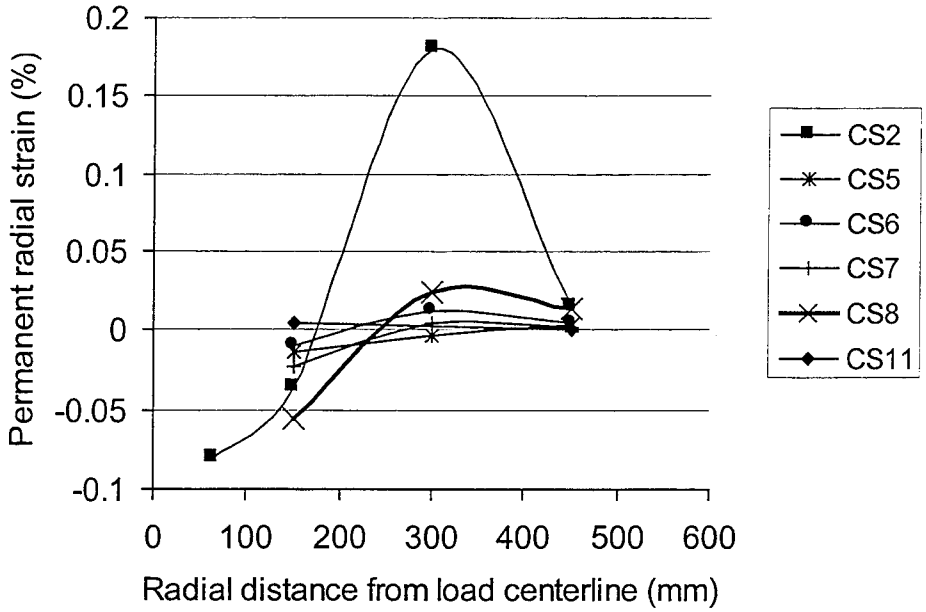

Figure 5.1.33 Permanent radial strain in the subgrade versus radial distance for cycle 1 (CS2-CS11, Z=415 mm).

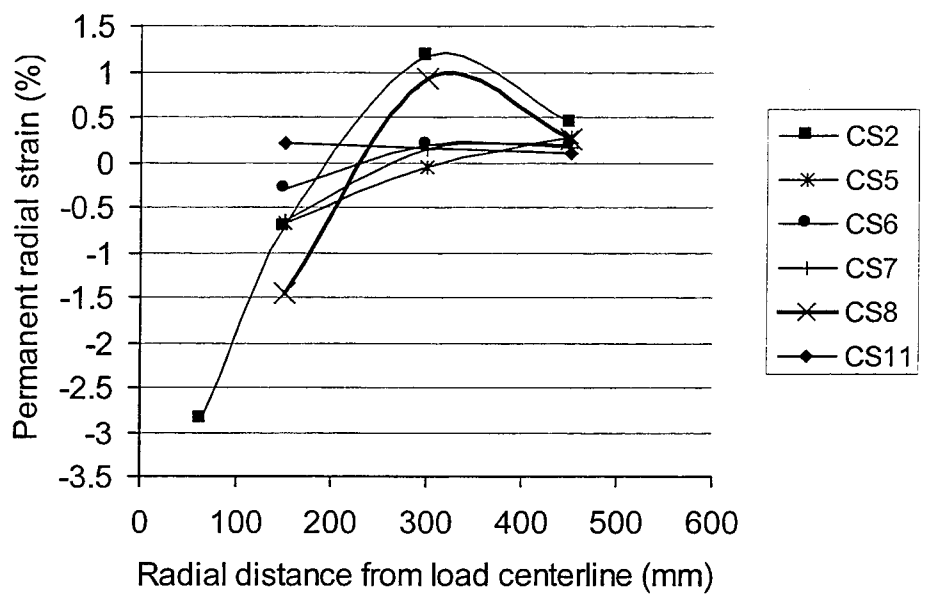

Figure 5.1.34 Permanent radial strain in the subgrade versus radial distance at cycle 40,000 (CS2-CS11, Z=415 mm).

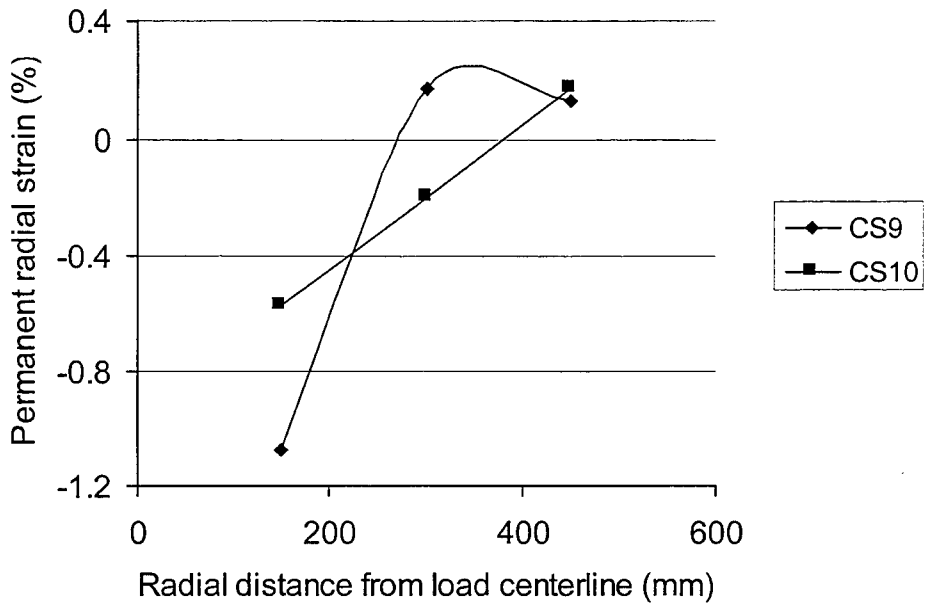

Figure 5.1.35 Permanent radial strain in the subgrade versus radial distance at cycle 125,000 (CS9, CS10, Z=490 mm).

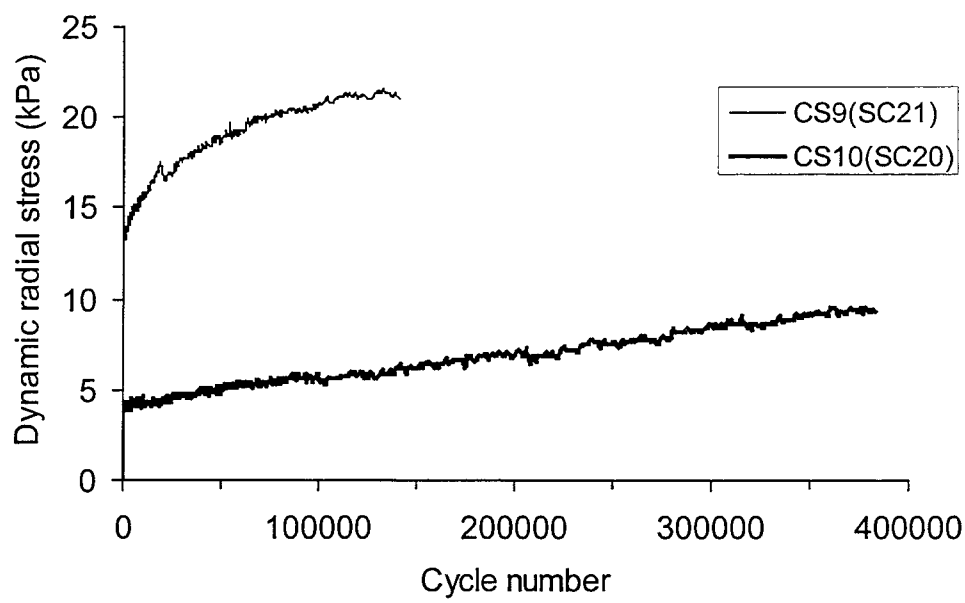

Figure 5.1.36 Dynamic radial stress in the subgrade versus load cycle (CS9, CS10, R=250 mm, Z=525 mm).

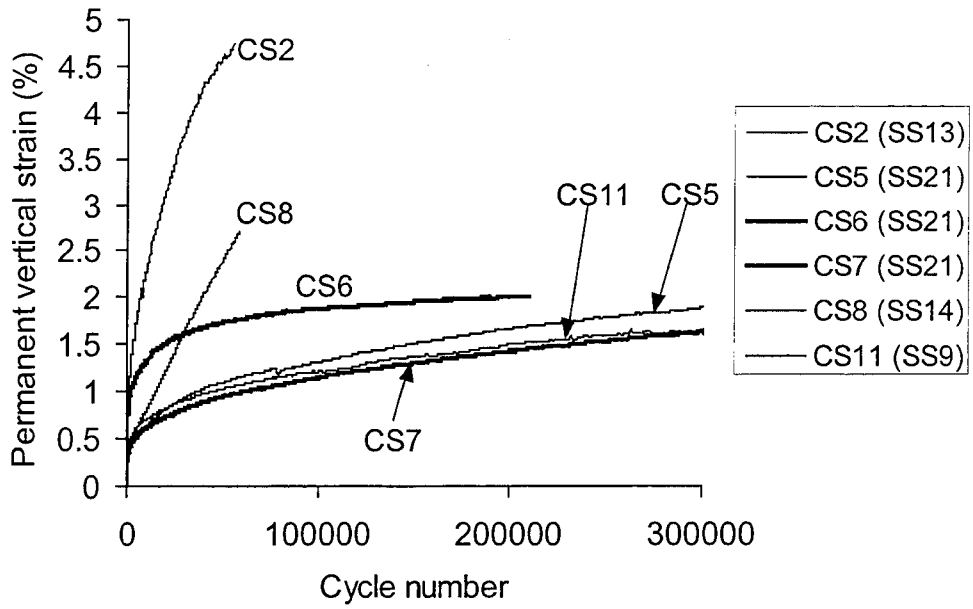

Figure 5.1.37 Permanent vertical strain in the subgrade versus load cycle (CS2-CS11, R=65 mm, Z=450 mm).

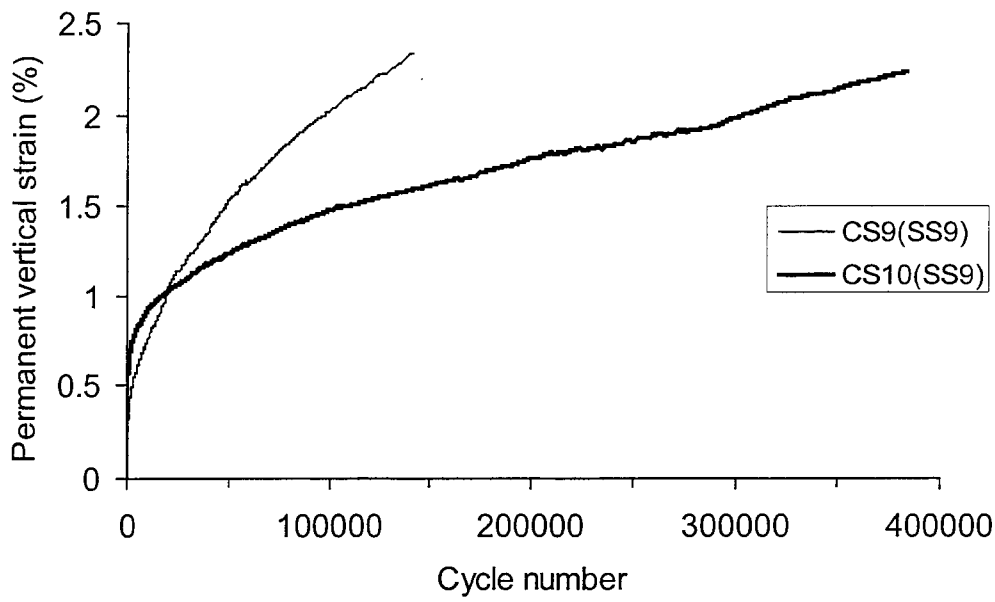

Figure 5.1.38 Permanent vertical strain in the subgrade versus load cycle (CS9, CS10, R=65 mm, Z=525 mm).

5.1.5 Mechanisms of Increased Base Course Thickness

The effect of 75 mm of additional base aggregate is described by comparing the unreinforced sections with the thinner 300 mm base (CS2 and CS8) to the thicker 375 mm base section (CS9). It is noted for the following comparisons that due to the different thickness of base, the depth of the instruments that are being compared is different between the sections. The measures are common, however, with respect to the distance above or below the base/subgrade interface. Figure 5.1.39 shows that an additional 75 mm of base has the effect of reducing lateral strain in the base layer similar to the effects of adding reinforcement. The 375 mm base section exhibits a better load distribution on the top of the subgrade in terms of applied dynamic vertical stress as shown in Figure 5.1.40. A similar effect is shown with a reduction in radial strain in the top of the subgrade as seen in Figure 5.1.41. The effect of the addition of 75 mm of base on permanent vertical strain in the subgrade is shown in Figure 5.1.42. The effects illustrated in Figures 5.1.39-5.1.42 are very similar to the effects associated with reinforcement discussed previously. This data indicates that the structural contribution of geosynthetic reinforcement is quite similar to that of additional base course material.

In terms of rutting performance, the reinforced sections with the 300 mm thick base performed better than the unreinforced 375 mm thick base section. It appears that geosynthetic reinforcement was providing a greater contribution to overall performance (rut depth development) than the addition of 75 mm of base.

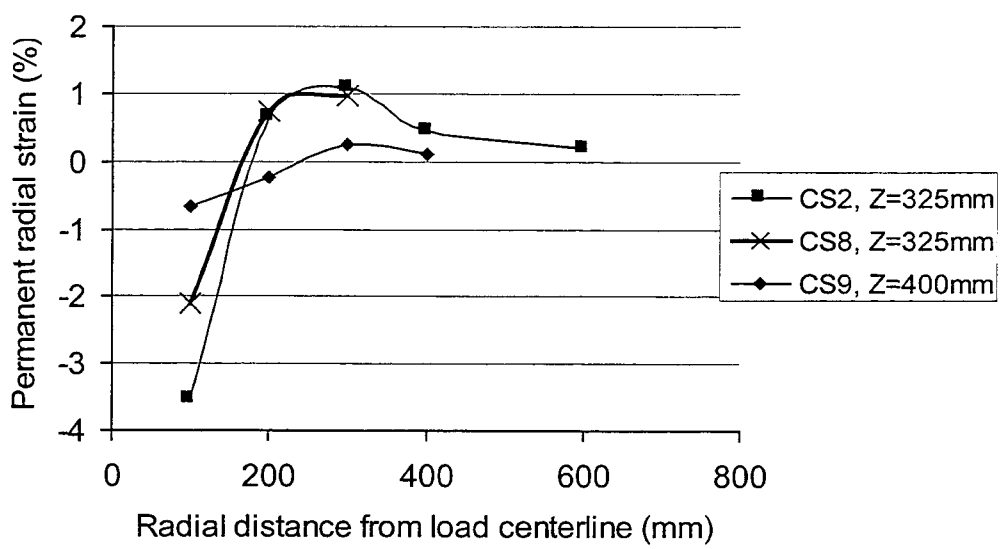

Figure 5.1.39 Permanent radial strain in the base versus radial distance at cycle 40,000 (CS2, CS8, CS9).

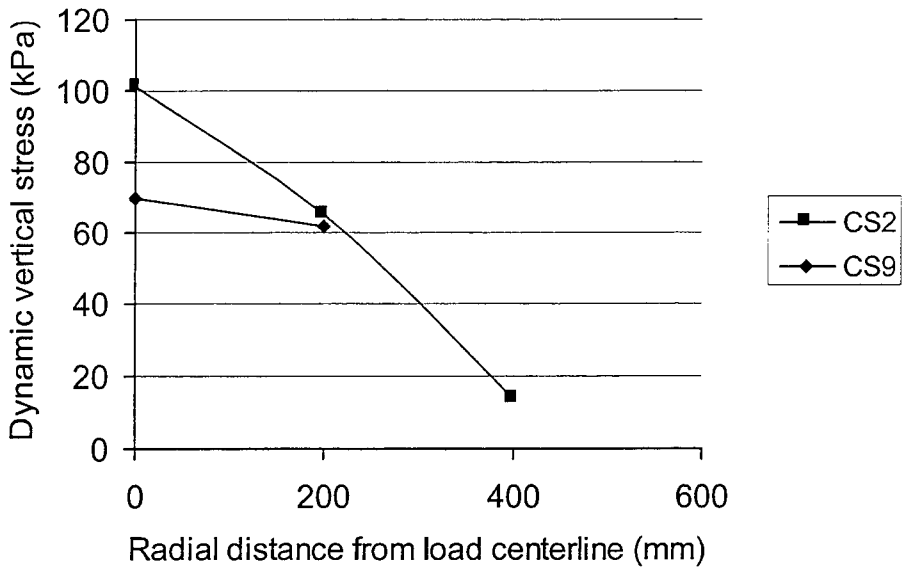

Figure 5.1.40 Dynamic vertical stress in the subgrade versus radial distance at cycle 40,000 (CS2, CS9).

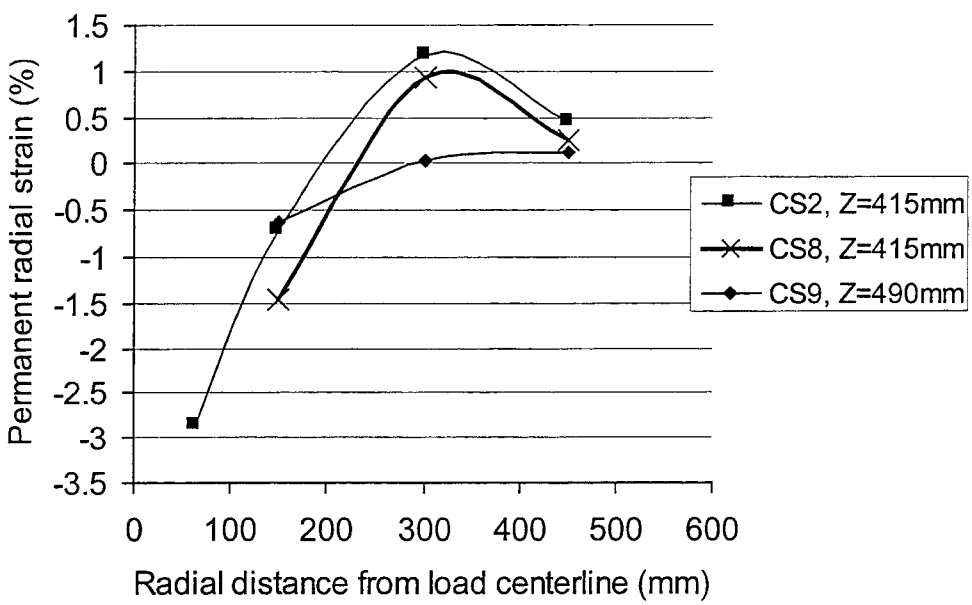

Figure 5.1.41 Permanent radial strain in the subgrade versus radial distance at cycle 40,000 (CS2, CS8, CS9).

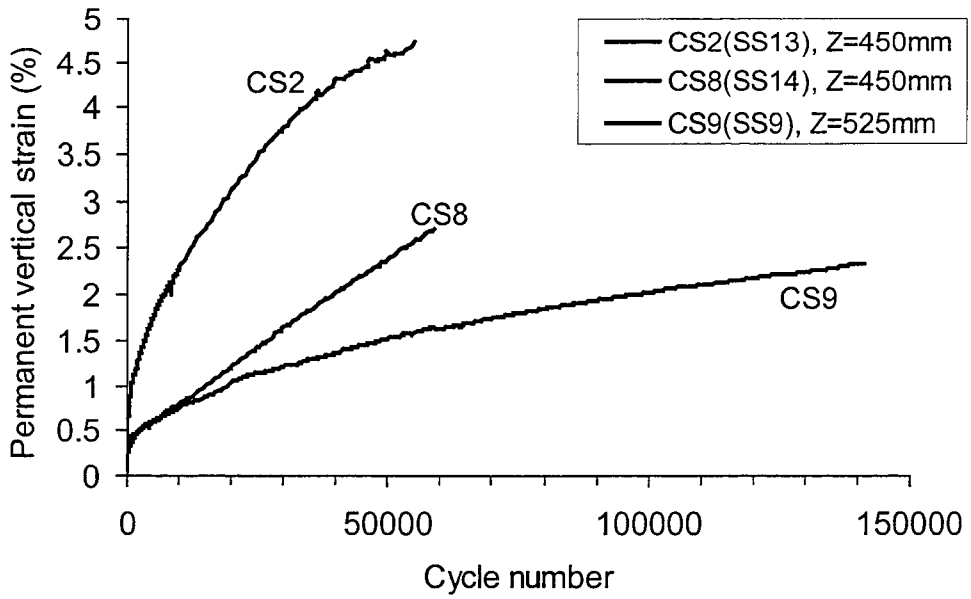

Figure 5.1.42 Permanent vertical strain in the subgrade versus load cycle (CS2, CS9).

5.2 Silty Sand Subgrade Sections

5.2.1 Rutting Behavior

As discussed in Section 3.5, a statistical comparison of test sections SSS1-SSS4 indicated that asphalt air voids in sections SSS1 and SSS4 (unreinforced sections) are statistically different from sections SSS2 and SSS3 (geogrid and geotextile reinforced), while each group is statistically comparable amongst themselves. Thus, direct comparisons are difficult between the two groups of sections. Comparisons between the sections will be made however, in a modeling effort that is on-going at the time of this report. Modeling will be able to incorporate differences in asphalt properties and equivalent sections may be modeled to gain a better understanding of the reinforcement benefits. Additionally, sections SSS5-SSS9, which used cold-mix as the surfacing material, did not yield consistent results due to problems with compaction of the cold-mix AC. Results from sections SSS5-SSS9 will be used, however, to illustrate some compatibility issues between the geosynthetics and the surrounding soil.

Figure 5.2.1 illustrates the permanent rutting performance of the four sections SSS1-SSS4. At the time of this report, it is believed that the performance differences between groups of sections is most likely due to AC property differences. Further illustrating this difference between the groups of sections is Figure 5.2.2, which shows significantly higher radial strain in the AC developed in sections SSS2 and SSS3, than in sections SSS1 and SSS4, mostly likely due

to a less-stiff AC material. Between SSS2 and SSS3 in Figure 5.2.1, the geogrid section appears to perform slightly better than the geotextile section, although not significantly better. Figure 5.2.1 also demonstrates consistency between the construction of SSS1 and SSS4, which are identical control sections.

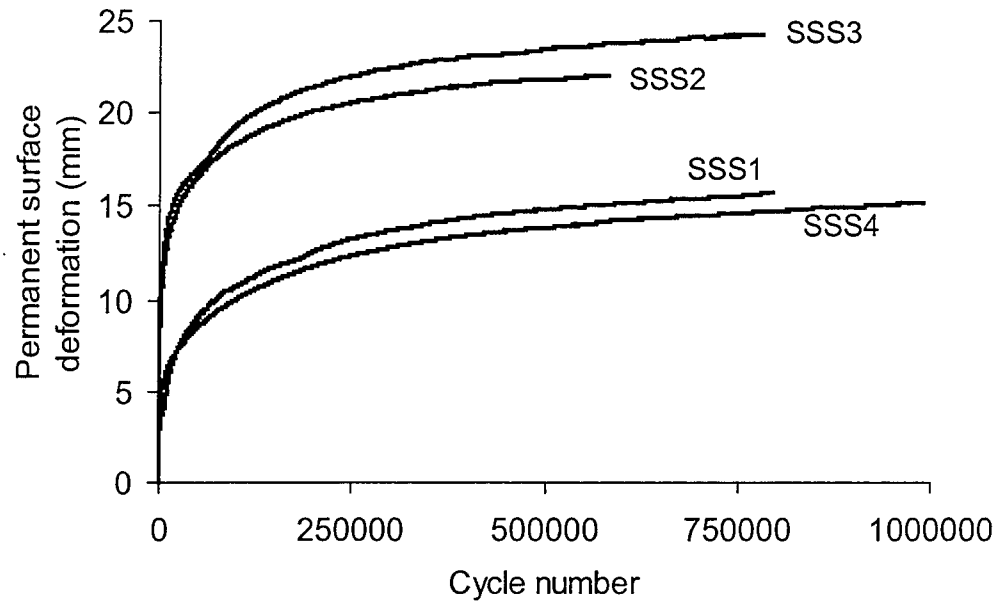

Figure 5.2.1 Permanent surface deformation versus load cycle (SSS1-SSS4).

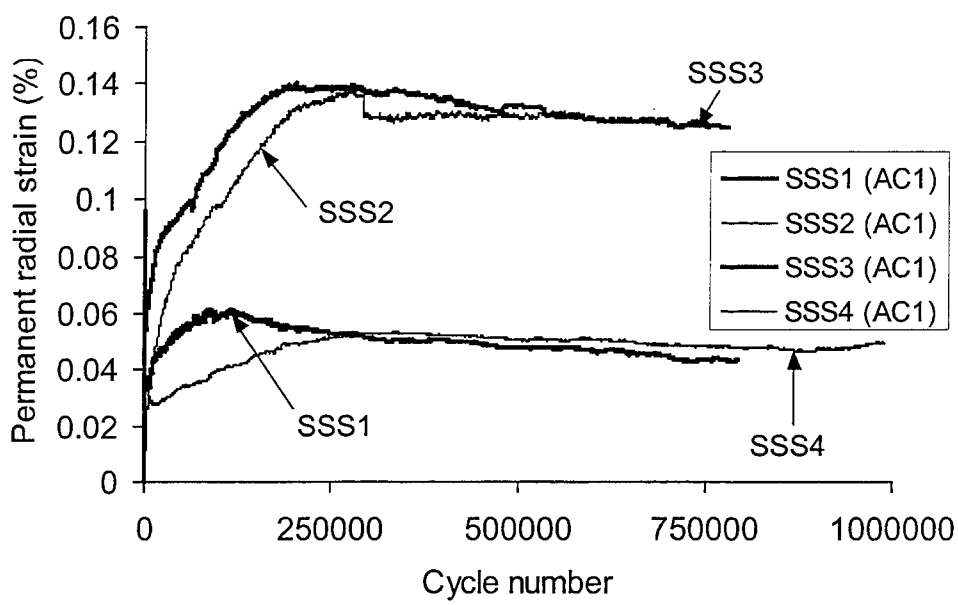

Figure 5.2.2 Permanent radial strain in the asphalt concrete versus load cycle (SSS1-SSS4, R=0, Z=67 mm).

5.2.2 Lateral Base Course Restraint

Figure 5.2.3 shows a greater amount of lateral spreading of the base in the geotextile reinforced section than in the geogrid reinforced section. Also illustrated in Figure 5.2.3 is the consistency of the two control sections, SSS1 and SSS4. Figure 5.2.4 illustrates a profile of radial strain in the base after 500,000 cycles of load where the geogrid reinforced section is seen to exhibit a modest improvement in the development of radial strain as compared to the geotextile section. These three figures indicate that the lower AC air voids (leading to a greater stiffness) in sections SSS1 and SSS4 leads to significantly improved lateral spreading of the base layer, indicating the importance of this parameter on performance. A result of the reduced lateral spreading in the base layer is a reduction of vertical strain in the base layer. Figure 5.2.5 illustrates a reduction in vertical strain directly beneath the load center for the geogrid reinforced section compared with the geotextile reinforced section.

Figures 5.2.6 and 5.2.7 illustrate that despite the lack of improvement in rutting behavior seen with the reinforced sections, relatively significant tensile radial strain is developed in the geosynthetics. Given the data presented earlier for the clay subgrade sections, it would be expected that strain development in the geosynthetics would lead to improvements in lateral spreading of the base and in turn influence rutting behavior. It is possible that had the AC in the reinforced and unreinforced sections been more comparable, then the shear interaction exhibited by the development of strain in the geosynthetics would have lead to an improvement in rutting behavior. It is difficult to say whether this improvement would have been significant. Given that the strains developed in the geosynthetics in the SSS sections are less than those in the CS sections, it would be expected that improvement in the SSS sections would not be as great as that seen in the CS sections. These results suggest that subgrade strength plays an important role in determining the amount of reinforcement benefit derived from geosynthetics.

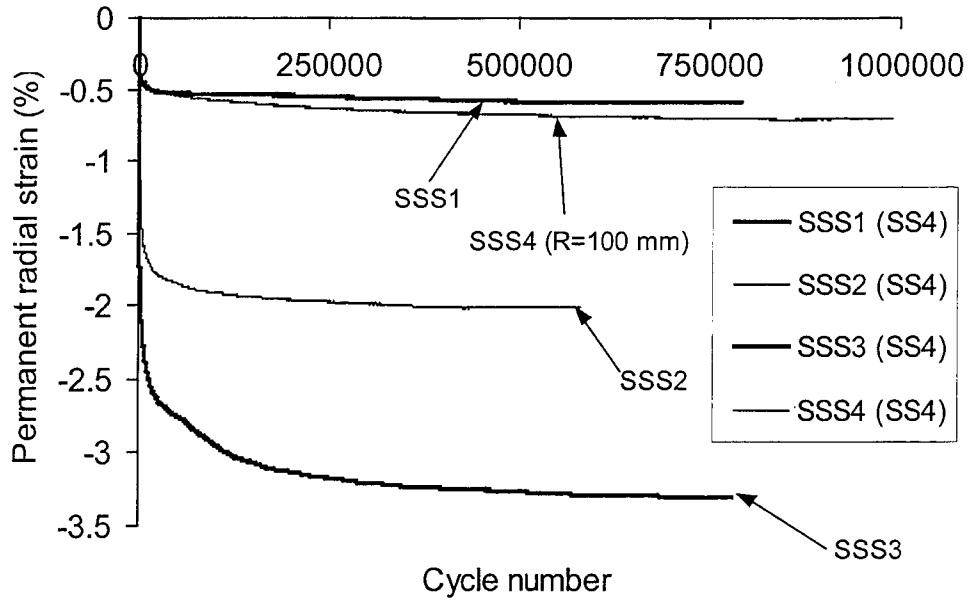

Figure 5.2.3 Permanent radial strain in the base versus load cycle (SSS1-SSS4, R=150 mm, Z=215 mm).

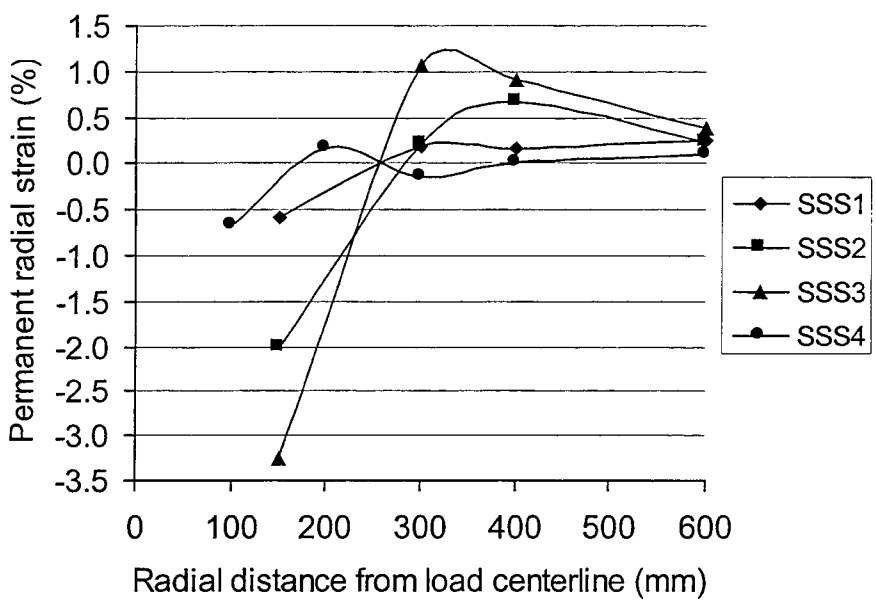

Figure 5.2.4 Permanent radial strain in the base versus radial distance at cycle 500,000 (SSS1-SSS4, Z=215 mm).

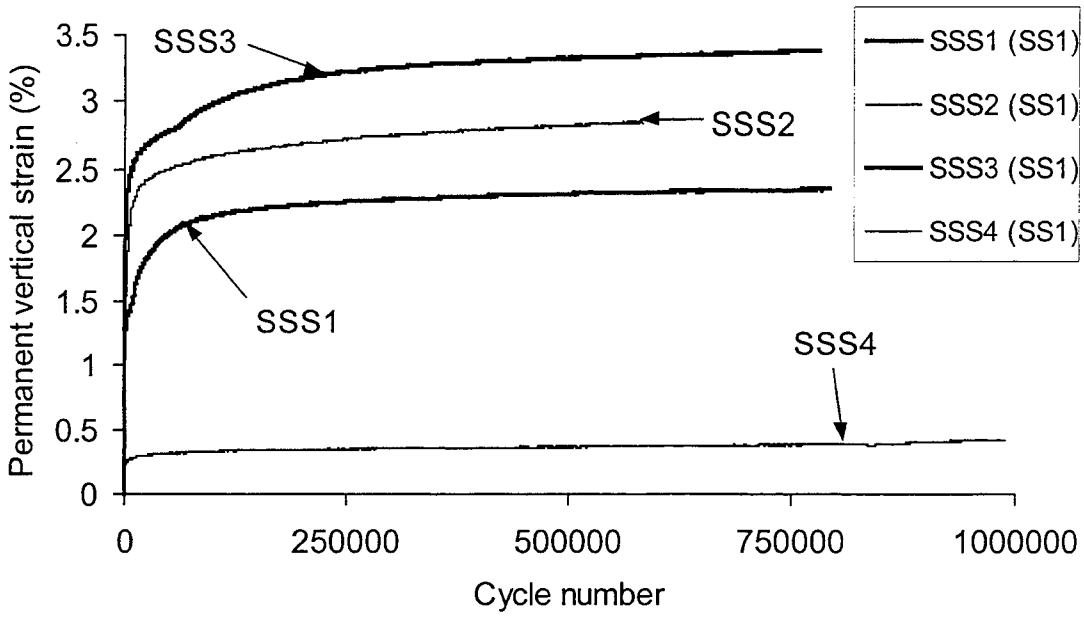

Figure 5.2.5 Permanent vertical strain in the base versus load cycle (SSS1-SSS4, R=60 mm, Z=160 mm).

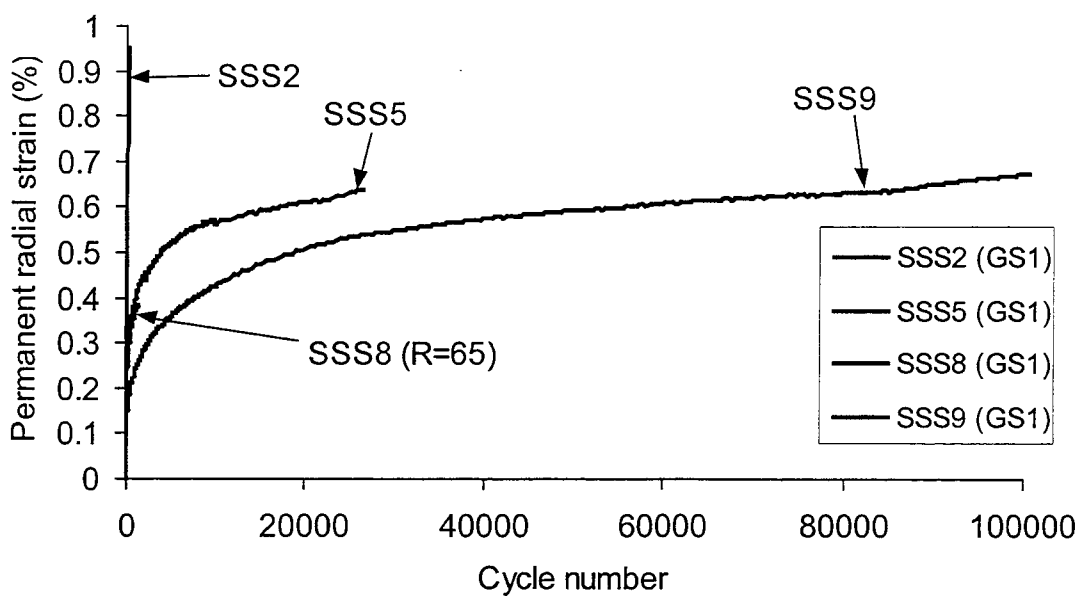

Figure 5.2.6 Permanent radial strain in the geosynthetics (M) versus load cycle (SSS2-SSS9, R=15 mm).

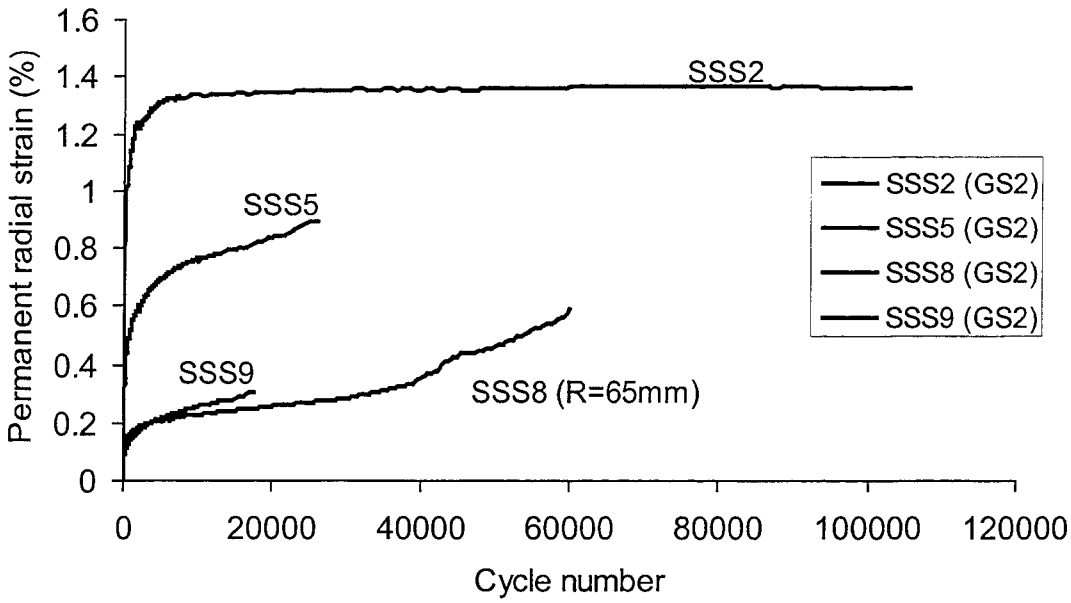

Figure 5.2.7 Permanent radial strain in the geosynthetics (XM) versus load cycle (SSS2-SSS9, R=23 mm).

5.2.3 Soil-Geosynthetic Compatibility

Results from sections SSS2, SSS5, and SSS8 can be used to illustrate the influence of geosynthetic type on compatibility of strain between the geosynthetic and the base course aggregate. Compatibility of strains is an indication of the amount of relative slip of the base across the geosynthetic and illustrates the effectiveness of the geosynthetic in resisting shear of the base. Figures 5.2.8 and 5.2.9 show profiles of permanent radial and tangential strain, respectively, in the base aggregate and on the geogrid in section SSS5. Reasonable compatibility between the geogrid and the base soil is illustrated in these figures. Figures 5.2.10 and 5.2.11 provide similar information for section SSS8 where a geotextile was used. These figures illustrate less compatibility between the geotextile and the base aggregate, illustrating that greater slip appears to occur with the geotextile for this particular pavement system configuration.

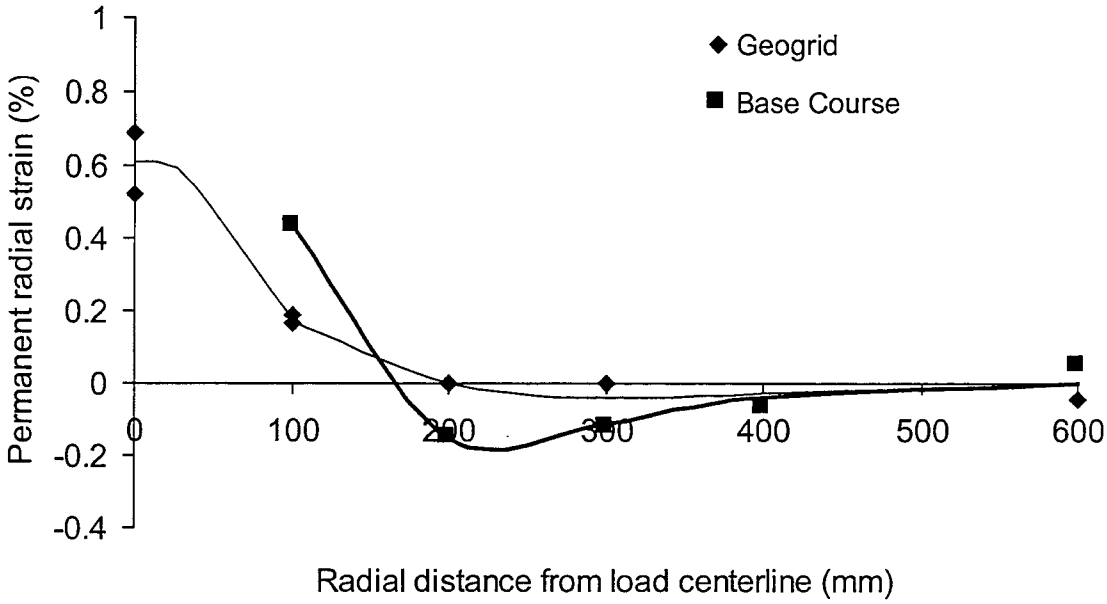

Figure 5.2.8 Permanent radial strain in geogrid A and base versus radial distance at cycle 5000 (SSS5).

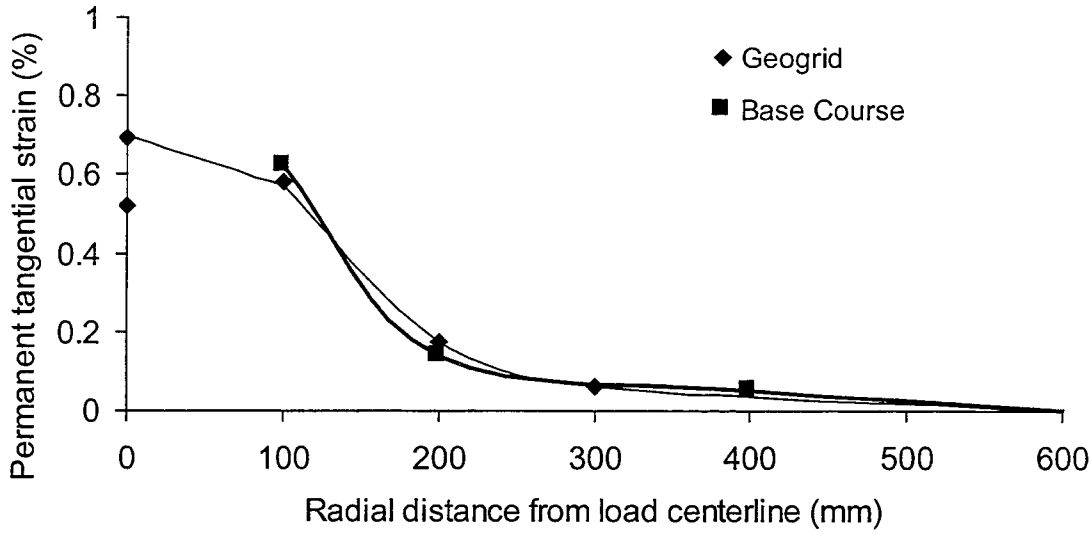

Figure 5.2.9 Permanent tangential strain in geogrid A and base versus radial distance at cycle 5000 (SSS5).

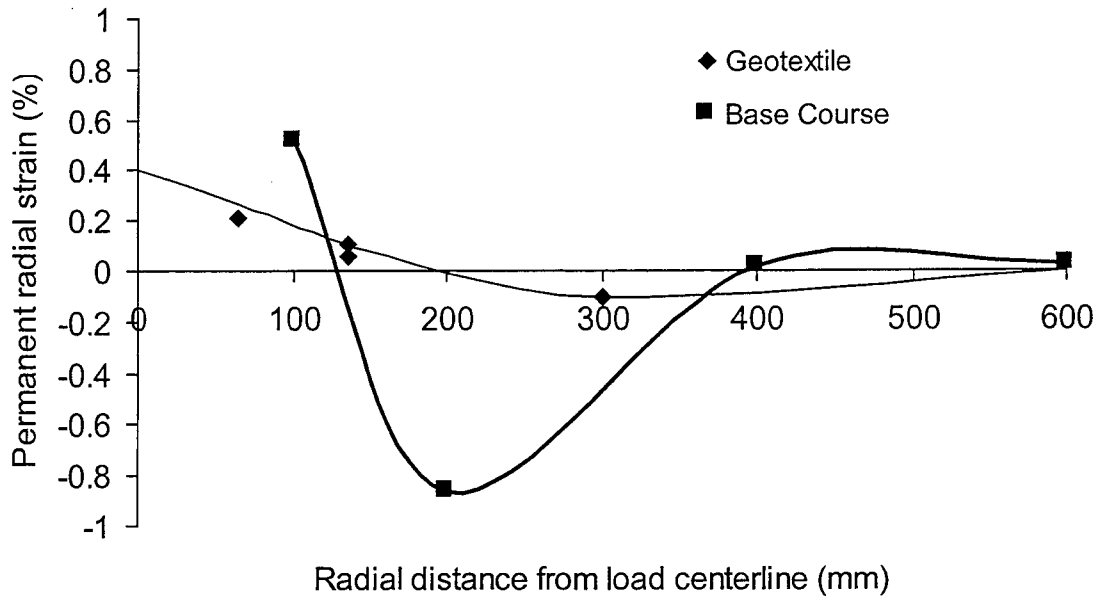

Figure 5.2.10 Permanent radial strain in geotextile and base versus radial distance at cycle 5000 (SSS8).

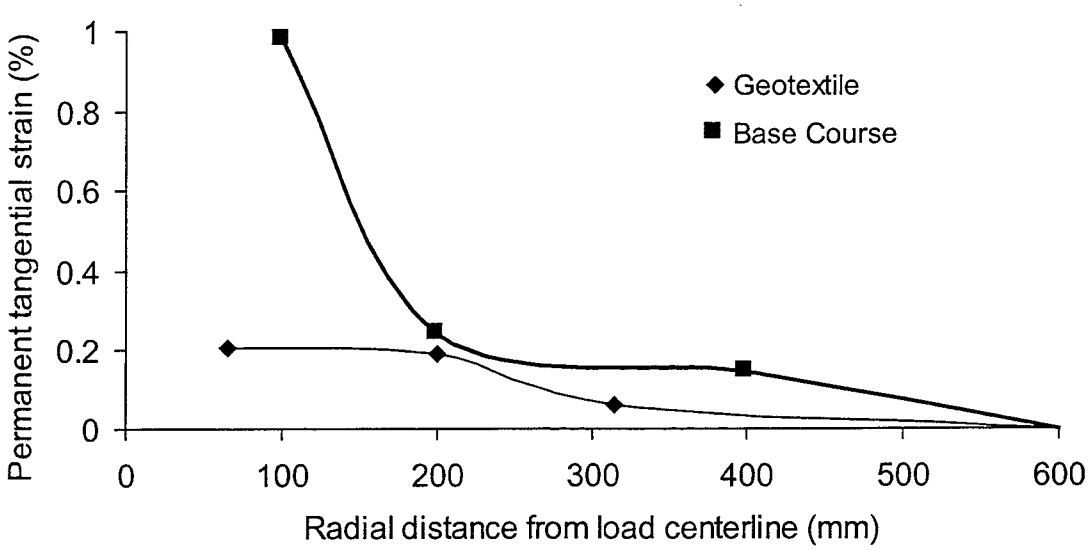

Figure 5.2.11 Permanent tangential strain in geotextile and base versus radial distance at cycle 5000 (SSS8).

5.2.4 Subgrade Effects

Figures 5.2.12 and 5.2.13 illustrate the dynamic vertical stress observed in the top of the subgrade. Both figures show very little difference between the two reinforced sections which are also seen to have higher stresses than the unreinforced sections. As described earlier, this latter effect is believed to be due to the higher air voids in the AC of the reinforced sections. An examination of the radial strain (indicative of lateral spreading) in the top of the subgrade also yielded no conclusive differences between the two reinforced sections. Permanent vertical strain developed in the subgrade was, on the average, similar between the two reinforced sections.

5.3 Discussion

The results presented in Section 5 have been presented to illustrate reinforcement mechanisms described in Section 2. For the test sections using the soft clay subgrade, results clearly showed a significant influence of reinforcement on the lateral strain developed in the bottom of the base and resulting vertical strain developed in the base. An improved vertical stress distribution on the top of the subgrade was seen in the reinforced sections. Less lateral strain was also developed in the top of the subgrade of the reinforced sections, indicating that less shear stress was transferred to the subgrade. The mechanism described in Section 2 regarding the effect of an increase in radial stress in the bottom of the base due to lateral confinement of the base by the geosynthetic could not be demonstrated. The stress cells measuring radial stress were typically placed 75 mm above the geosynthetic. The sensors measuring strain were located 50 mm above the geosynthetic. It is possible that any influence of the geosynthetic on lateral confinement and subsequent increase in radial stress occurs within a layer of base adjacent to the geosynthetic that is less than 75 mm in thickness.

The data presented in Section 5.1.3 showed that reinforcement improves the vertical stress distribution on the subgrade. Given that the geosynthetic has no bending stiffness, stiffness in another layer of material must be increasing for this effect to be seen. If this increase in stiffness occurs in the base as a result of an increase in confinement, then it is most likely occurring for a layer of base adjacent to the geosynthetic that could not be monitored by the stress cells used in this work.

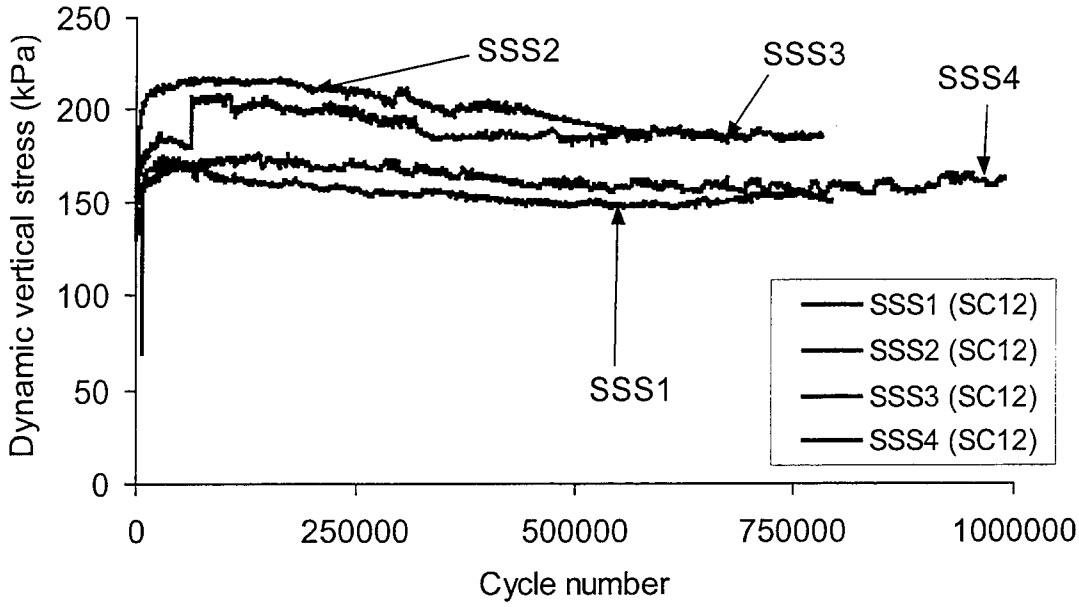

Figure 5.2.12 Dynamic vertical stress in the subgrade versus load cycle (SSS1-SSS4, R=0, Z=350 mm).

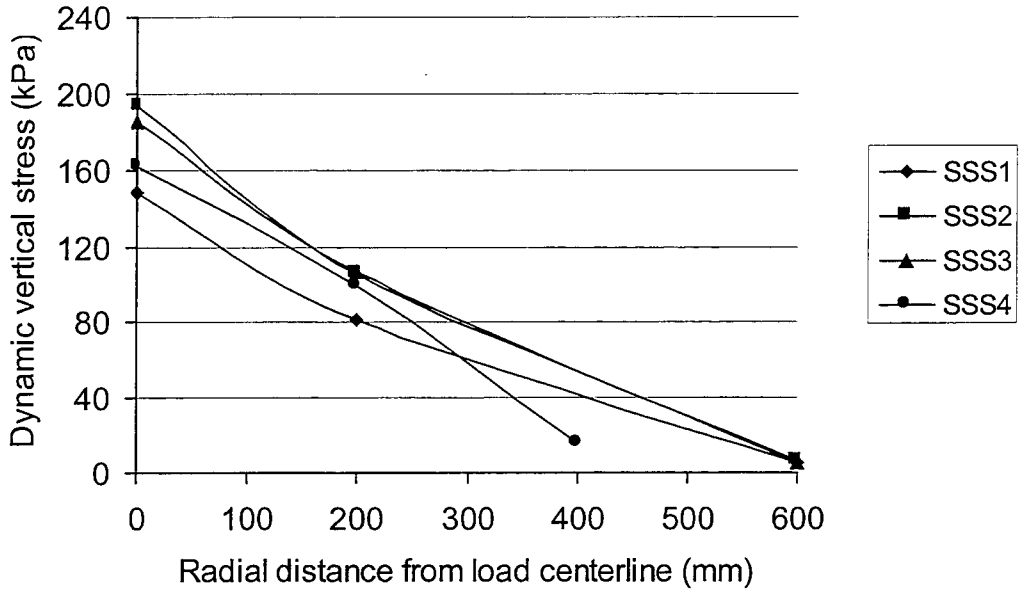

Figure 5.2.13 Dynamic vertical stress in the subgrade versus radial distance at cycle 5000 (SSS1-SSS4, Z=350 mm).

An improvement in vertical stress distribution on the subgrade is expected to be accompanied by a similar improvement in the base layer. Measurements of vertical stress in the bottom of the base did not necessarily show this effect. Figure 5.3.1 shows results of dynamic vertical stress versus radial distance for load cycle 40,000 for sections CS2, 5, 6 and 8. The two reinforced sections show lower vertical stresses at R=0 as compared to R=150 mm. Integration under these curves with respect to radius and rotation about R=0 must produce a constant equal to the applied surface load. Assuming that the values shown in Figure 5.3.1 are correct, it becomes clear that sufficient data points are not available to define variations in these curves.

This data suggests that a stress-arching effect may be taking place which could be responsible for an improved vertical stress distribution on the subgrade. Shear interaction along the geosynthetic interface creates shear forces acting on the base aggregate that are directed toward the load centerline. This may be responsible for the development of an arching effect in the base that causes vertical stress to be reduced directly beneath the load plate and increased at the periphery of the arch. If this effect occurs, variations in the curves shown in Figure 5.3.1 would be expected to be dramatic. For example, it is possible that between a radius of 0 and 150 mm, the curves reach a peak well above 250 kPa, corresponding to a radius at the periphery of the stress arch. A considerably more detailed instrumentation plan would be needed to illustrate this effect.

The better performance seen with the geogrid materials as compared to the geotextile used appears to be related to a better vertical stress distribution on the top of the subgrade. An examination of radial and vertical strains in the base showed little differences between these sections. Radial strain in the top of the subgrade also appeared to be approximately the same. Excavation of the geotextile reinforced section showed that a dimpling pattern had occurred as larger aggregate stones had caused the geotextile to penetrate slightly into the subgrade. It is believed that the majority of this dimpling occurred during load application as base aggregate moved down and along the geotextile surface. Repeated load applications were most likely necessary to create this pattern, which explains why the geotextile section initially deformed like the unreinforced sections. As a result of this dimpling pattern, a pseudo-interlocking effect occurred between the base aggregate and the geotextile. This condition indicates complications associated with using shear-interaction tests (i.e. pullout or direct shear tests) for the purpose of defining shear-interaction mechanical properties.

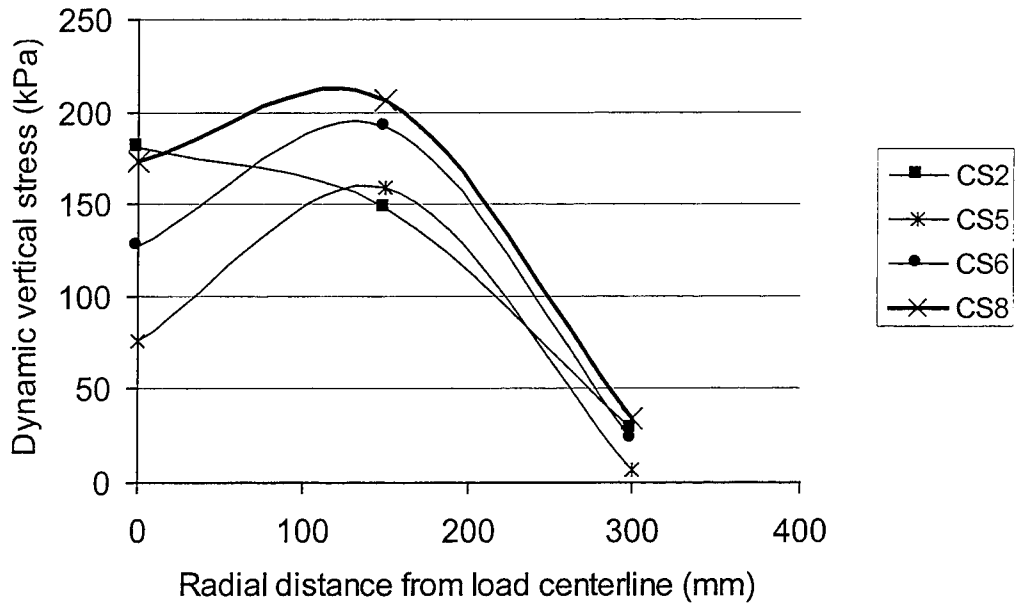

Figure 5.3.1 Dynamic vertical stress in the base versus radial distance at cycle 40,000 (Z=300 mm).

6.0 SUMMARY AND CONCLUSIONS

A pavement test facility has been developed for the purpose of examining the mechanical behavior of geosynthetic-reinforced pavement systems. In an ongoing study, the data provided from these sections will be compared to predictions made from a finite element model currently under development. The model will contain features necessary to describe the reinforcement mechanisms illustrated in this study. Results from the finite element model will be used to develop a design methodology that can be readily adopted by State DOT's.

The pavement test facility consists of a large concrete box in which field-scale subgrade, base, geosynthetic and asphalt concrete layers can be placed. Pavement system performance has been assessed by applying a cyclic, non-translating, 40 kN load to a circular plate resting on the pavement surface. Pavement distress results from the development of permanent deformation of the pavement surface.

Variables included in the 20 test sections constructed are subgrade type, strength and stiffness, geosynthetic type and placement position in the base layer and base layer thickness. An array of sensors to measure stress, strain, displacement, load, temperature and moisture content has been included in the test sections. A test section specifically constructed to illustrate the

consistency of response from these sensors has shown good consistency in these measures. This test section was also used to establish trends in stress and strain response in the pavement layers for a single dynamic load application. Comparison of response from duplicated control sections has shown good consistency of instrument response and overall rutting behavior.

Extensive measures were taken to provide for quality control during construction of the test sections. A statistical analysis of constructed pavement layer properties has shown that the only statistically significant property that varied between sections that also had a significant influence on pavement performance was the asphalt concrete air voids achieved during compaction. Two test sections with statistically different air voids (CS1 and CS3) illustrated poor performance in comparison to duplicated test sections with an AC air voids more comparable to the control sections. The remaining sections for the clay subgrade type were shown to have reasonably comparable air voids and are believed to be comparable for the purpose of illustrating geosynthetic reinforcement mechanisms and benefits. For the test sections using the more competent silty-sand subgrade, the reinforced sections and control sections had statistically different air voids and could not be directly compared.

Overall results from the test sections have demonstrated that significant improvement in pavement performance, as defined by surface rutting, results from the inclusion of geosynthetic reinforcement. Substantial improvement was seen when a soft clay subgrade having a CBR of 1.5 was used. For the stronger subgrade, having a CBR of approximately 20, direct comparison of reinforced and unreinforced sections was difficult because of differences in the air voids of the AC, however it appears that little to no improvement occurred under these conditions. For all test sections, mixing of the subgrade and base course aggregate was not observed, indicating that any improvement in pavement performance was due to reinforcement functions.

With the geogrid products used, the stiffer geogrid (geogrid B) provided for better pavement performance as compared to geogrid A. Geogrid A and B were identical in terms of composition and size and differed only by the strength and stiffness of the material. The importance of placement position of the geosynthetic was seen by comparing two sections with geogrid A placed at the subgrade-base course interface and 100 mm up in a base layer having a thickness of 300 mm. Significantly better performance was observed when the geogrid was elevated in the base. Additionally, when geogrid A was placed at the bottom of a thicker base (375 mm), improvement as compared to a similar unreinforced section was not as great as the

same reinforcement configuration for a base layer having a thickness of 300 mm. This also indicates that placement position of the geosynthetic in proximity to the applied load is an important design consideration.

Test sections with the two geogrids used in this study performed better than the sections using the geotextile product, while improvement seen with the geotextile was still appreciable. An examination of stress and strain measures in the pavement layers showed that the greatest difference in response was the vertical stress distribution in the top of the subgrade that lead to greater vertical strain in the subgrade. The geotextile section was also seen to deform more like the unreinforced sections during the early portion of loading. The differences between the geogrid and geotextile sections is believed to be due primarily to the differences in shear-interaction properties of the material with the surrounding base aggregate and to intrinsic load-strain properties of the material.

Relatively high Traffic Benefit Ratios (TBR) were seen for the reinforced sections. For the geogrid reinforced sections, significant TBR values were seen for the first 1 mm of permanent deformation, indicating that benefits due to reinforcement were realized immediately upon load application. Examination of stress and strain measures in the pavement materials also showed that reinforcement mechanisms occurred immediately upon load application. Additionally, the high rate of rutting at the beginning of each test was reduced by the reinforcement. Deformations corresponding to this stage of the test were seen in all pavement layers and were reduced by the presence of reinforcement.

Comparison of reinforced sections with a 300 mm base to an unreinforced section with a 375 mm base showed better performance with the reinforced sections, indicating that the reinforcement allows for at least a 20 % reduction in base thickness. Given the substantially better performance of the reinforced sections as compared to this unreinforced section, this number is certainly greater than 20 %. Comparison of two unreinforced sections with a 300 and 375 mm base thickness showed that improvements due to a thicker base section, as described by stress and strain measures in the pavement layers, were similar to those seen by the addition of reinforcement.

An examination of stress and strain measures in the pavement layers illustrates several reinforcement mechanisms taking place in this application. On the clay subgrade, reinforcement has the effect of considerably reducing the radial strain developed in the bottom of the base,

which leads to a reduction of vertical strain in the base. In conjunction with this effect is the development of significant tensile strains in the geosynthetics. Dynamic strains were used to show that dynamic loads as great as 2.6 kN/m were developed in the geogrid materials. Incremental permanent strains were developed in the geosynthetics indicating that advanced material modeling accounting for creep related ratcheting effects will be required to fully describe reinforcement.

In the subgrade layer, reinforcement has the effect of improving the vertical stress distribution on the top of the subgrade, which leads to a reduction of vertical strain. Although stress instrumentation in the base could not confirm this effect, it is believed that an improved vertical stress distribution is due to an increase in radial stress in the bottom of the base which leads to a layer of stiffer base aggregate. An improved vertical stress distribution in the subgrade may also be due to stress arching in the base as a result of restoring shear stresses acting on the base via interaction with the geosynthetic.

Similar to the pattern of radial strain in the base, reinforcement had the effect of reducing radial strain in the top of the subgrade. This is believed to be an indication of less shear stress reaching the top of the subgrade due to shear transfer to the geosynthetic. Similar to the result of an improved vertical stress distribution, less radial strain results in less vertical strain in the subgrade.

For the stronger subgrade, a slight improvement was seen with the geogrid section as compared to the geotextile reinforced section. Examination of stress and strain measures in the pavement layers showed that little improvement effects were seen in the subgrade while lateral strain in the base was less in the geogrid section. An examination of strain compatability between the geosynthetics and the base aggregate showed that greater compatability, or bonding, occurred with the geogrid. For the geogrid section, relatively significant tensile strains were developed in the geogrid material, suggesting that reinforcement functions were occurring. Comparison to a similar unreinforced section was not possible, however, because of dissimilarities between the asphalt layer air voids content.

An examination of dynamic surface deformations and dynamic stress and strain measures in the pavement layers illustrates problems with correlating dynamic response to long-term rutting behavior. In general, single pulse dynamic response rarely provided a good correlation to long-term performance.

7.0 REFERENCES

Al-Qadi, I.L., Brandon, T.L., Valentine, R.J., Lacina, B.A. and Smith, T.E. (1994), "Laboratory Evaluation of Geosynthetic Reinforced Pavement Sections", *Transportation Research Record* 1439, Washington DC., USA, pp. 25-31.

Al-Qadi, I.L. Coree, B.J., Brandon, T.L., Bhutta, S.A. and Appea, A.K. (1998), "Quantifying the Separation Characteristic of Geosynthetics in Flexible Pavements", *Proceedings of the Sixth International Conference on Geosynthetics*", Atlanta, GA, USA, Vol. 2, pp. 945-950.

AMOCO (1996) Personal Fax Communication, 6-12-1996.

Anderson, P. and Killeavy, M. (1989), "Geotextiles and Geogrids: Cost Effective Alternate Materials for Pavement Design and Construction", *Proceedings of the Conference Geosynthetics '89,* San Diego, CA, USA, pp. 353-360.

Askegaard, V., Brink, A. and Ullidtz, P. (1997), "Pressure Cell Calibration Tests", *Transportation Research Board Annual Meeting Preprint*, Paper No. 970158.

Barksdale, R. D., Brown, S. F. and Chan, F. (1989), "Potential Benefits of Geosynthetics in Flexible Pavement Systems", *National Cooperative Highway Research Program Report No. 315,* Transportation Research Board, National Research Council, Washington DC, USA, 56p.

Bender, D.A. and Barenberg, E.J. (1978), "Design and Behavior of Soil-Fabric-Aggregate Systems", *Transportation Research Record 671*, TRB, National Research Council, Washington, DC, USA, pp. 64-75.

Brown, S.F., Jones, C.P.D. and Brodrick, B.V. (1982), "Use of Non-Woven Fabrics in Permanent Road Pavements", *Proceedings of the Institution of Civil Engineers,* London, UK, Part 2, Vol. 73, pp. 541-563.

Cancelli, A., Montanelli, F., Rimoldi, P. and Zhao, A. (1996), "Full Scale Laboratory Testing on Geosynthetics Reinforced Paved Roads", *Proceedings of the International Symposium on Earth Reinforcement,* Fukuoka/Kyushu, Japan, November, Balkema, pp. 573-578.

Collin, J. G., Kinney, T. C. and Fu, X. (1996), "Full Scale Highway Load Test of Flexible Pavement Systems With Geogrid Reinforced Base Courses", *Geosynthetics Intentional,* Vol. 3, No. 4, pp. 537-549.

Cuelho, E.V. (1998), *Determination of Geosynthetic Constitutive Parameters and Soil/Geosynthetic Interaction by In-Air and In-Soil Experiments*, M.S. Thesis, Montana State University – Bozeman, 227 p.

Fogelsong, M.L. (1998), *Evaluation of Full-Scale Laboratory Models of Geosynthetic Reinforced Pavement Systems*, M.S. Thesis, Montana State University – Bozeman, 236 p.

Geotechnical Fabrics Report (1994), *1995 Specifier's Guide*, Vol. 12, No. 9, pg. 169.

Geotechnical Fabrics Report (1997), *1998 Specifier's Guide*, Vol. 15, No. 9, pg. 74.

Haas R., Wall, J., and Carroll, R.G. (1988), "Geogrid Reinforcement of Granular Bases in Flexible Pavements," *Transportation Research Record 1188*, Washington DC, USA, pp. 19 - 27.

Halliday, A.R. and Potter, J.F. (1984), "The Performance of a Flexible Pavement Constructed on a Strong Fabric", *Transport and Road Research Laboratory, Report 1123,* Crowthorne, Berkshire, UK, 15 p.

Kinney, T.C. and Barenberg, E.J. (1982), "The Strengthening Effect of Geotextiles on Soil-Geotextile-Aggregate Systems", *Proceedings of the Second International Conference on Geotextiles*, Las Vegas, NV, USA, Vol. 2, pp. 347-352.

Kinney, T.C., Stone, D.K. and Schuler, J. (1998a), "Using Geogrids for Base Reinforcement as Measured by Falling Weight Deflectometer in Full-Scale Laboratory Study", *Transportation Research Record 1611*, Washington DC, USA, pp. 70 - 77.

Kinney, T.C., Abbott, J. and Schuler, J. (1998b), "Benefits of Using Geogrids for Base Reinforcement with Regard to Rutting", *Transportation Research Record 1611*, Washington DC, USA, pp. 86-96.

Miura, N., Sakai, A., Taesiri, Y., Yamanouchi, T. and Yasuhara, K. (1990), "Polymer Grid Reinforced Pavement on Soft Clay Grounds", *Geotextiles and Geomembranes,* Vol. 9, pp. 99-123.

MnRoad (1993), "User Guide to the Dynamic Cone Penetrometer", Office of Minnesota Road Research, Minnesota Department of Transportation, 18 p.

Moghaddas-Nejad, F. and Small, J.C. (1996), "Effect of Geogrid Reinforcement in Model Track Tests on Pavements", *Journal of Transportation Engineering*, ASCE, Vol. 122, No. 6, pp. 468-474.

Perkins, S.W. and Ismeik, M. (1997a), "A Synthesis and Evaluation of Geosynthetic Reinforced Base Course Layers in Flexible Pavements: Part I Experimental Work", *Geosynthetics International,* Vol. 4, No. 6, pp. 549-604.

Perkins, S.W. and Ismeik, M. (1997b), "A Synthesis and Evaluation of Geosynthetic Reinforced Base Course Layers in Flexible Pavements: Part II Analytical Work", *Geosynthetics International,* Vol. 4, No. 6, pp. 605-621.

Petersen, R.G. (1985), *Design and Analysis of Experiments*, Marcel Dekker, Inc., New York, 429 pp.

Ruddock, E.C., Potter, J.F. and McAvoy, A.R. (1982), "A Full-Scale Experiment on Granular and Bituminous Road Pavements Laid on Fabrics", *Proceedings of the Second International Conference on Geotextiles,* Las Vegas, Nevada, USA, Vol. 2, pp. 365-370.

Selig, E.T., Zhang, J. and Ebersöhn, W. (1997), "Evaluation of Dynamic Earth Pressure Cells for Subgrade", *Transportation Research Record 1596*, Washington DC, USA, pp. 1 - 6.

Sellmeijer, J.B. (1990), "Design of Geotextile Reinforced Paved Roads and Parking Areas", *Proceedings of the Fourth International Conference on Geotextiles, Geomembranes and Related Products*, Balkema, Vol. 1, The Hague, The Netherlands, pp.177-182.

Ullidtz, P., Askegaard, V. and Sjolin, F.O. (1996), "Normal Stresses in a Granular Material Under FWD Loading", *Transportation Research Board Annual Meeting Preprint*, Paper No. 960024.

Webster, S. L. (1993), "Geogrid Reinforced Base Courses For Flexible Pavements For Light Aircraft, Test Section Construction, Behavior Under Traffic, Laboratory Tests, and Design Criteria", *Technical Report GL-93-6,* USAE Waterways Experiment Sta., Vicksburg, MS, USA, 86 p.

APPENDIX A: INSTRUMENT LOCATIONS

Table A1 Instrument locations for test section PCS1

Sensor	Name	Pavement Layer	Orientation	Location (mm)		
				x	y	z
Load Cell	LC	Surface	Vertical	0	0	0
Surface Deform. (LVDT)	SD1	Surface	Vertical	400	0	0
	SD2	Surface	Vertical	270	0	0
	SD3	Surface	Vertical	170	0	0
	SD4	Surface	Vertical	50	0	0
	SD5	Surface	Vertical	-50	0	0
	SD6	Surface	Vertical	-170	0	0
	SD7	Surface	Vertical	-270	0	0
	SD8	Surface	Vertical	-400	0	0
Stress Cell	SC8	Base -1	Radial	0	-300	225
	SC9	Base - 2	Tangential	600	0	300
	SC10	Base - 2	Radial	400	0	300
	SC11	Base - 2	Vertical	200	0	300
	SC12	Base - 2	Vertical	-200	0	300
	SC13	Base - 2	Radial	-400	0	300
	SC14	Base - 2	Tangential	-600	0	300
	SC15	Subgrade - 2	Tangential	600	0	450
	SC16	Subgrade - 2	Radial	400	0	450
	SC17	Subgrade - 2	Vertical	200	0	450
	SC18	Subgrade - 2	Vertical	-200	0	450
	SC19	Subgrade - 2	Radial	-400	0	450
	SC20	Subgrade - 2	Tangential	-600	0	450
	SC21	Subgrade - 3	Tangential	600	0	675
	SC22	Subgrade - 3	Radial	400	0	675
	SC23	Subgrade - 3	Vertical	200	0	675
	SC24	Subgrade - 3	Vertical	-200	0	675
	SC25	Subgrade - 3	Tangential	-400	0	675
AC Strain Gages	AC1	AC	Center	0	0	67

Table A1 Continued.

Soil Strain (LVDT)	SS10	Base - 1	Center	0	0	225
	SS11	Base - 3	Tangential	0	600	355
	SS12	Base - 3	Radial	0	400	355
	SS13	Base - 2	Vertical	0	200	300
	SS14	Base - 2	Vertical	0	-200	300
	SS15	Base - 3	Radial	0	-400	355
	SS16	Base - 3	Tangential	0	-600	355
	SS17	Subgrade - 1	Tangential	0	600	415
	SS18	Subgrade - 1	Radial	0	400	415
	SS19	Subgrade - 2	Vertical	0	200	450
	SS20	Subgrade - 2	Vertical	0	-200	450
	SS21	Subgrade - 1	Radial	0	-400	415
	SS22	Subgrade - 1	Tangential	0	-600	415
	SS23	Subgrade - 3	Vertical	0	200	675
	SS24	Subgrade - 3	Center	0	0	675
	SS25	Subgrade - 3	Vertical	0	-200	675

Table A2 Instrument locations for test section CS2

Sensor	Name	Pavement Layer	Orientation	Location (mm)		
				x	y	z
Load Cell	LC	Surface	Vertical	0	0	0
Surface Deform. (LVDT)	SD1	Surface	Vertical	400	0	0
	SD2	Surface	Vertical	270	0	0
	SD3	Surface	Vertical	170	0	0
	SD4	Surface	Vertical	50	0	0
	SD5	Surface	Vertical	-50	0	0
	SD6	Surface	Vertical	-170	0	0
	SD7	Surface	Vertical	-270	0	0
	SD8	Surface	Vertical	-400	0	0
Stress Cell	SC1	Base -1	Radial	-151	0	225
	SC2	Base - 2	Vertical	0	0	300
	SC9	Base - 2	Vertical	0	300	300
	SC4	Base - 2	Vertical	106	107	300
	SC5	Base - 2	Radial	-340	0	300
	SC6	Base - 2	Radial	-71	71	300
	SC7	Base - 2	Radial	145	-141	300
	SC8	Base - 2	Radial	0	-300	300
	SC3	Base - 2	Radial	0	-600	300
	SC10	Base - 2	Tangential	-100	0	300
	SC11	Base - 2	Tangential	0	205	300
	SC12	Base - 2	Tangential	-283	-283	300
	SC13	Subgrade - 1	Vertical	0	0	450
	SC14	Subgrade - 1	Vertical	0	-401	450
	SC15	Subgrade - 1	Vertical	200	0	450
	SC16	Subgrade - 1	Radial	-649	0	450
	SC17	Subgrade - 1	Radial	0	150	450
	SC18	Subgrade - 1	Radial	0	252	450
	SC19	Subgrade - 1	Radial	-318	319	450
	SC20	Subgrade - 2	Vertical	0	-1	625
	SC21	Subgrade - 2	Vertical	-295	0	625
	SC22	Subgrade - 2	Radial	0	150	625
	SC23	Subgrade - 2	Radial	0	-600	625
	SC24	Subgrade - 3	Vertical	0	0	775
	SC25	Subgrade - 4	Vertical	0	0	1075
AC Strain Gages	AC1	AC	Radial	-150	0	67

Table A2 Continued.

Soil Strain (LVDT)	SS1	Base -1	Center -x-	0	0	225
	SS2	Base - 2	Vertical	0	66	300
	SS3	Base - 2	Vertical	-212	212	300
	SS4	Base - 2	Vertical	0	-150	300
	SS10	Base - 2	Radial	0	400	325
	SS6	Base - 2	Radial	-71	-72	325
	SS7	Base - 2	Radial	-200	0	325
	SS8	Base - 2	Radial	212	212	325
	SS9	Base - 2	Radial	-600	0	325
	SS5	Base - 2	Tangential	99	0	325
	SS11	Base - 2	Tangential	200	0	325
	SS12	Base - 2	Tangential	0	-401	325
	SS13	Subgrade - 1	Vertical	-65	0	450
	SS14	Subgrade - 1	Vertical	1	450	450
	SS15	Subgrade - 1	Vertical	-200	0	450
	SS16	Subgrade - 1	Radial	65	0	415
	SS17	Subgrade - 1	Radial	0	-150	415
	SS18	Subgrade - 1	Radial	0	-300	415
	SS19	Subgrade - 1	Radial	-450	0	415
	SS20	Subgrade - 2	Vertical	65	0	625
	SS21	Subgrade - 2	Vertical	0	297	625
	SS22	Subgrade - 2	Radial	0	-155	625
	SS23	Subgrade - 2	Radial	0	-355	625
	SS24	Subgrade - 3	Vertical	0	65	775
	SS25	Subgrade - 4	Vertical	0	60	1075
TDR Probes	MC1	Subgrade	Radial	0	550	625
	MC2	Subgrade	Radial	0	550	775
Temp. Probes	TP1	Base -1	NA	0	100	225
	TP4	Base -2	NA	-300	0	300
	TP6	Base - 2	NA	0	-500	300
	TP7	Subgrade 1	NA	-300	0	450
	TP8	Subgrade 2	NA	0	300	625
	TP9	Subgrade-3	NA	0	-100	775
	TP10	Subgrade-4	NA	0	-100	1075

Table A3 Instrument locations for test section CS5

Sensor	Name	Pavement Layer	Orientation	Location (mm)		
				x	y	z
Load Cell	LC	Surface	Vertical	0	0	0
Surface Deform. (LVDT)	SD1	Surface	Vertical	400	0	0
	SD2	Surface	Vertical	270	0	0
	SD3	Surface	Vertical	170	0	0
	SD4	Surface	Vertical	50	0	0
	SD5	Surface	Vertical	-50	0	0
	SD6	Surface	Vertical	-170	0	0
	SD7	Surface	Vertical	-270	0	0
	SD8	Surface	Vertical	-400	0	0
Stress Cell	SC1	Base -1	Radial	0	150	225
	SC2	Base - 2	Vertical	0	0	300
	SC7	Base - 2	Vertical	106	106	300
	SC5	Base - 2	Vertical	0	300	300
	SC11	Base - 2	Radial	141	-141	300
	SC12	Base - 2	Radial	0	-300	300
	SC9	Base - 2	Radial	-400	0	300
	SC13	Base - 2	Radial	0	-600	300
	SC22	Subgrade - 1	Vertical	0	0	450
	SC17	Subgrade - 1	Vertical	200	0	450
	SC19	Subgrade - 1	Radial	-106	106	450
	SC15	Subgrade - 1	Radial	106	106	450
	SC20	Subgrade - 1	Radial	0	250	450
	SC18	Subgrade - 1	Radial	0	400	450
	SC23	Subgrade - 2	Vertical	0	0	625
	SC24	Subgrade - 3	Vertical	0	0	775
	SC25	Subgrade - 4	Vertical	0	0	1075
AC Strain Gages	AC1	AC	Radial	-150	0	67

Table A3 Continued.

Geosyn. Strain	GS1	Geogrid	Radial-M	15	0	375
	GS2	Geogrid	Radial-T	0	20	375
	GS3	Geogrid	Radial-M	-318	0	375
	GS4	Geogrid	Radial-M	122	0	375
	GS5	Geogrid	Radial-M	422	0	375
	GS6	Geogrid	Radial-T	0	137	375
	GS7	Geogrid	Radial-M	-205	0	375
Soil Strain (LVDT)	SS1	Base –1	Center -x-	0	0	225
	SS2	Base –1	Radial	0	-150	225
	SS3	Base – 2	Vertical	0	65	300
	SS15	Base – 2	Vertical	0	-150	300
	SS4	Base – 2	Vertical	-212	212	300
	SS8	Base – 2	Radial	-71	-71	325
	SS9	Base – 2	Radial	-200	0	325
	SS11	Base – 2	Radial	212	212	325
	SS7	Base – 2	Radial	0	400	325
	SS13	Base – 2	Tangential	100	0	325
	SS5	Base – 2	Tangential	0	200	325
	SS21	Subgrade - 1	Vertical	-65	0	450
	SS17	Subgrade - 1	Vertical	-200	0	450
	SS14	Subgrade - 1	Vertical	0	-300	450
	SS12	Subgrade - 1	Vertical	283	283	450
	SS16	Subgrade - 1	Radial	-106	-106	415
	SS22	Subgrade - 1	Radial	212	-212	415
	SS19	Subgrade - 1	Radial	-318	318	415
	SS23	Subgrade - 2	Vertical	-65	0	625
	SS24	Subgrade - 3	Vertical	-65	0	775
	SS25	Subgrade - 4	Vertical	-65	0	1075

Table A4 Instrument locations for test section CS6

Sensor	Name	Pavement Layer	Orientation	Location (mm)		
				x	y	z
Load Cell	LC	Surface	Vertical	0	0	0
Surface Deform. (LVDT)	SD1	Surface	Vertical	400	0	0
	SD2	Surface	Vertical	270	0	0
	SD3	Surface	Vertical	170	0	0
	SD4	Surface	Vertical	50	0	0
	SD5	Surface	Vertical	-50	0	0
	SD6	Surface	Vertical	-170	0	0
	SD7	Surface	Vertical	-270	0	0
	SD8	Surface	Vertical	-400	0	0
Stress Cell	SC2	Base -1	Radial	0	150	225
	SC1	Base - 2	Vertical	30	0	300
	SC5	Base - 2	Vertical	0	300	300
	SC14	Base - 2	Vertical	106	106	300
	SC16	Base - 2	Radial	-400	0	300
	SC11	Base - 2	Radial	141	-141	300
	SC21	Base - 2	Radial	0	-300	300
	SC13	Base - 2	Radial	0	-600	300
	SC15	Subgrade - 1	Radial	106	106	450
	SC18	Subgrade - 1	Radial	0	400	450
	SC17	Subgrade - 1	Radial	0	260	450
	SC20	Subgrade - 1	Vertical	200	0	450
	SC22	Subgrade - 1	Vertical	0	0	450
	SC23	Subgrade - 2	Vertical	0	0	625
	SC24	Subgrade - 3	Vertical	0	0	775
	SC25	Subgrade - 4	Vertical	0	0	1075
AC Strain Gages	AC1	AC	Radial	-150	0	67

Table A4 Continued.

Geosyn. Strain	GS1	Geotextile	Radial-M	0	-65	375
	GS2	Geotextile	Radial-T	-65	0	375
	GS3	Geotextile	Tangential-M	0	-200	375
	GS4	Geotextile	Radial-M	135	0	375
	GS5	Geotextile	Tangential-T	-200	0	375
	GS6	Geotextile	Radial-T	0	135	375
	GS7	Geotextile	Radial-M	-300	0	375
	GS8	Geotextile	Tangential-T	270	0	375
	GS9	Geotextile	Tangential-M	0	315	375
	GS10	Geotextile	Radial-T	0	-330	375
	GS12	Geotextile	Radial-M	620	0	375
Soil Strain (LVDT)	SS1	Base –1	Center -x-	0	0	225
	SS2	Base –1	Radial	0	-150	225
	SS15	Base – 2	Vertical	0	-150	300
	SS3	Base – 2	Vertical	0	65	300
	SS4	Base – 2	Vertical	-212	212	300
	SS10	Base – 2	Tangential	0	200	325
	SS7	Base – 2	Radial	0	400	325
	SS8	Base – 2	Radial	-71	-71	325
	SS9	Base – 2	Radial	-200	0	325
	SS11	Base – 2	Radial	212	212	325
	SS18	Base – 2	Tangential	100	0	325
	SS16	Subgrade - 1	Radial	-106	-106	415
	SS19	Subgrade - 1	Radial	-318	318	415
	SS22	Subgrade - 1	Radial	212	-212	415
	SS12	Subgrade - 1	Vertical	-283	-283	450
	SS14	Subgrade - 1	Vertical	-10	-305	450
	SS17	Subgrade - 1	Vertical	-200	0	450
	SS21	Subgrade - 1	Vertical	-65	0	450

Table A5 Instrument locations for test section CS7

Sensor	Name	Pavement Layer	Orientation	Location (mm)		
				x	y	z
Load Cell	LC	Surface	Vertical	0	0	0
Surface Deform. (LVDT)	SD1	Surface	Vertical	400	0	0
	SD2	Surface	Vertical	270	0	0
	SD3	Surface	Vertical	170	0	0
	SD4	Surface	Vertical	50	0	0
	SD5	Surface	Vertical	-50	0	0
	SD6	Surface	Vertical	-170	0	0
	SD7	Surface	Vertical	-270	0	0
	SD8	Surface	Vertical	-400	0	0
Stress Cell	SC1	Base -1	Vertical	0	0	200
	SC11	Base - 1	Vertical	150	0	200
	SC6	Base - 1	Radial	141	141	200
	SC2	Base - 1	Radial	-400	0	200
	SC13	Base - 2	Vertical	0	0	325
	SC16	Base - 2	Vertical	150	0	325
	SC14	Base - 2	Radial	141	141	325
	SC15	Base - 2	Radial	-400	0	325
	SC22	Subgrade - 1	Vertical	0	0	450
	SC21	Subgrade - 1	Vertical	200	0	450
	SC17	Subgrade - 1	Radial	106	106	450
	SC20	Subgrade - 1	Radial	0	250	450
	SC18	Subgrade - 1	Radial	0	400	450
	SC23	Subgrade - 2	Vertical	0	0	625
	SC24	Subgrade - 3	Vertical	0	0	775
	SC25	Subgrade - 4	Vertical	0	0	1075
AC Strain Gages	AC1	AC	Radial	-150	0	67

Table A5 Continued.

Geosyn. Strain	GS1	Geogrid	Radial-M	-15	0	275
	GS2	Geogrid	Radial-T	0	-21	275
	GS3	Geogrid	Radial-M	128	0	275
	GS4	Geogrid	Radial-T	0	-142	275
	GS5	Geogrid	Radial-M	-215	0	275
	GS6	Geogrid	Radial-M	318	0	275
	GS7	Geogrid	Radial-T	0	420	275
Soil Strain (LVDT)	SS11	Base – 1	Vertical	0	65	200
	SS2	Base – 1	Vertical	0	-150	200
	SS3	Base – 1	Radial	-200	0	225
	SS10	Base – 1	Radial	-212	-212	225
	SS4	Base – 1	Radial	0	400	225
	SS8	Base – 2	Vertical	0	65	325
	SS9	Base – 2	Vertical	15	-140	325
	SS5	Base – 2	Radial	-71	-71	325
	SS24	Base – 2	Radial	-200	0	325
	SS15	Base – 2	Radial	-212	212	325
	SS7	Base – 2	Radial	0	400	325
	SS21	Subgrade - 1	Vertical	-65	0	450
	SS17	Subgrade - 1	Vertical	-200	0	450
	SS14	Subgrade - 1	Vertical	0	-300	450
	SS12	Subgrade - 1	Vertical	-283	-283	450
	SS16	Subgrade - 1	Radial	-106	-106	415
	SS19	Subgrade - 1	Radial	-318	318	415
	SS22	Subgrade - 1	Radial	212	-212	415
	SS23	Subgrade - 2	Vertical	-60	0	625
	SS20	Subgrade - 3	Vertical	-65	0	775
	SS25	Subgrade - 4	Vertical	-65	0	1075

Table A6 Instrument locations for test section CS8

Sensor	Name	Pavement Layer	Orientation	Location (mm)		
				x	y	z
Load Cell	LC	Surface	Vertical	0	0	0
Surface Deform. (LVDT)	SD1	Surface	Vertical	400	0	0
	SD2	Surface	Vertical	270	0	0
	SD3	Surface	Vertical	170	0	0
	SD4	Surface	Vertical	50	0	0
	SD5	Surface	Vertical	-50	0	0
	SD6	Surface	Vertical	-170	0	0
	SD7	Surface	Vertical	-270	0	0
	SD8	Surface	Vertical	-400	0	0
Stress Cell	SC2	Base -1	Radial	0	150	225
	SC1	Base - 2	Vertical	0	0	300
	SC6	Base - 2	Vertical	106	106	300
	SC7	Base - 2	Vertical	0	300	300
	SC13	Base - 2	Radial	141	-141	300
	SC14	Base - 2	Radial	0	-300	300
	SC15	Base - 2	Radial	-400	0	300
	SC16	Base - 2	Radial	0	-600	300
	SC17	Subgrade - 1	Vertical	0	0	450
	SC18	Subgrade - 1	Vertical	200	0	450
	SC20	Subgrade - 1	Radial	106	106	450
	SC21	Subgrade - 1	Radial	0	250	450
	SC22	Subgrade - 1	Radial	0	400	450
	SC23	Subgrade - 2	Vertical	0	0	625
	SC24	Subgrade - 3	Vertical	0	0	775
	SC25	Subgrade - 4	Vertical	0	0	1075
AC Strain Gages	AC1	AC	Radial	-150	0	67

Table A6 Continued.

Soil Strain (LVDT)	SS2	Base –1	Center -x-	0	0	225
	SS3	Base –1	Radial	0	-150	225
	SS4	Base – 2	Vertical	0	65	300
	SS7	Base – 2	Vertical	0	-150	300
	SS8	Base – 2	Vertical	-212	212	300
	SS9	Base – 2	Radial	-71	-71	325
	SS10	Base – 2	Radial	-200	0	325
	SS11	Base – 2	Radial	212	212	325
	SS12	Base – 2	Radial	0	400	325
	SS5	Base – 2	Tangential	100	0	325
	SS17	Base – 2	Tangential	0	200	325
	SS20	Subgrade - 1	Radial	-106	-106	415
	SS21	Subgrade - 1	Radial	212	-212	415
	SS23	Subgrade - 1	Radial	-318	318	415
	SS14	Subgrade - 1	Vertical	-65	0	450
	SS16	Subgrade - 1	Vertical	-200	0	450
	SS15	Subgrade - 1	Vertical	0	-300	450
	SS19	Subgrade - 1	Vertical	283	283	450
	SS22	Subgrade - 2	Vertical	-65	0	625
	SS24	Subgrade - 3	Vertical	-65	0	775
	SS25	Subgrade - 4	Vertical	-65	0	1075

Table A7 Instrument locations for test section CS9

Sensor	Name	Pavement Layer	Orientation	Location (mm)		
				x	y	z
Load Cell	LC	Surface	Vertical	0	0	0
Surface Deform. (LVDT)	SD1	Surface	Vertical	400	0	0
	SD2	Surface	Vertical	270	0	0
	SD3	Surface	Vertical	170	0	0
	SD4	Surface	Vertical	50	0	0
	SD5	Surface	Vertical	-50	0	0
	SD6	Surface	Vertical	-170	0	0
	SD7	Surface	Vertical	-270	0	0
	SD8	Surface	Vertical	-400	0	0
Stress Cell	SC4	Base -1	Radial	0	150	263
	SC1	Base -1	Vertical	0	0	263
	SC2	Base - 2	Vertical	0	0	375
	SC5	Base - 2	Vertical	106	106	375
	SC6	Base - 2	Vertical	0	300	375
	SC7	Base - 2	Radial	141	-141	375
	SC12	Base - 2	Radial	0	-300	375
	SC13	Base - 2	Radial	-400	0	375
	SC14	Base - 2	Radial	0	-600	375
	SC15	Subgrade - 1	Vertical	0	0	525
	SC17	Subgrade - 1	Vertical	200	0	525
	SC20	Subgrade - 1	Radial	106	106	525
	SC21	Subgrade - 1	Radial	0	250	525
	SC22	Subgrade - 1	Radial	0	400	525
	SC23	Subgrade - 2	Vertical	0	0	700
	SC24	Subgrade - 3	Vertical	0	0	850
	SC25	Subgrade - 4	Vertical	0	0	1150
AC Strain Gages	AC1	AC	Radial	-150	0	67

Table A7 Continued.

Soil Strain (LVDT)	SS2	Base –1	Radial	0	300	263
	SS3	Base –1	Radial	-150	0	263
	SS17	Base – 1	Vertical	65	0	263
	SS8	Base – 1	Vertical	0	-150	215
	SS4	Base – 2	Vertical	0	65	375
	SS7	Base – 2	Vertical	0	-150	375
	SS15	Base – 2	Vertical	-212	212	375
	SS12	Base – 2	Radial	-71	-71	400
	SS10	Base – 2	Radial	-200	0	400
	SS11	Base – 2	Radial	212	212	400
	SS14	Base – 2	Radial	0	400	400
	SS20	Subgrade - 1	Radial	-106	-106	490
	SS21	Subgrade - 1	Radial	212	-212	490
	SS5	Subgrade - 1	Radial	-318	318	490
	SS9	Subgrade - 1	Vertical	-65	0	525
	SS16	Subgrade - 1	Vertical	-200	0	525
	SS23	Subgrade - 1	Vertical	0	-300	525
	SS19	Subgrade - 1	Vertical	283	283	525
	SS22	Subgrade - 2	Vertical	-65	0	700
	SS24	Subgrade - 3	Vertical	-65	0	850
	SS25	Subgrade - 4	Vertical	-65	0	1150

Table A8 Instrument locations for test section CS10

Sensor	Name	Pavement Layer	Orientation	Location (mm)		
				x	y	z
Load Cell	LC	Surface	Vertical	0	0	0
Surface Deform. (LVDT)	SD1	Surface	Vertical	400	0	0
	SD2	Surface	Vertical	270	0	0
	SD3	Surface	Vertical	170	0	0
	SD4	Surface	Vertical	50	0	0
	SD5	Surface	Vertical	-50	0	0
	SD6	Surface	Vertical	-170	0	0
	SD7	Surface	Vertical	-270	0	0
	SD8	Surface	Vertical	-400	0	0
Stress Cell	SC4	Base -1	Radial	0	150	263
	SC1	Base -1	Vertical	0	0	263
	SC2	Base - 2	Vertical	0	0	375
	SC5	Base - 2	Vertical	106	106	375
	SC11	Base - 2	Vertical	0	300	375
	SC12	Base - 2	Radial	141	-141	375
	SC13	Base - 2	Radial	0	-300	375
	SC14	Base - 2	Radial	-400	0	375
	SC15	Base - 2	Radial	0	-600	375
	SC16	Subgrade - 1	Vertical	0	0	525
	SC17	Subgrade - 1	Vertical	200	0	525
	SC19	Subgrade - 1	Radial	106	106	525
	SC20	Subgrade - 1	Radial	0	250	525
	SC21	Subgrade - 1	Radial	0	400	525
	SC22	Subgrade - 2	Vertical	0	0	700
	SC23	Subgrade - 3	Vertical	0	0	850
	SC24	Subgrade - 4	Vertical	0	0	1150
AC Strain Gages	AC1	AC	Radial	-150	0	67

Table A8 Continued.

Geosyn. Strain	GS1	Geogrid	Radial-T	0	20	450
	GS2	Geogrid	Radial-M	-15	0	450
	GS3	Geogrid	Radial-M	125	0	450
	GS4	Geogrid	Radial-T	0	135	450
	GS5	Geogrid	Radial-M	-210	0	450
	GS6	Geogrid	Radial-M	335	0	450
	GS7	Geogrid	Radial-T	0	-412	450
Soil Strain (LVDT)	SS2	Base –1	Radial	0	300	263
	SS3	Base –1	Radial	-150	0	263
	SS12	Base – 1	Vertical	65	0	263
	SS8	Base – 1	Vertical	0	-150	263
	SS14	Base – 2	Vertical	0	65	375
	SS7	Base – 2	Vertical	0	-150	375
	SS15	Base – 2	Vertical	-212	212	375
	SS4	Base – 2	Radial	-71	-71	400
	SS10	Base – 2	Radial	-200	0	400
	SS11	Base – 2	Radial	212	212	400
	SS17	Base – 2	Radial	0	400	400
	SS20	Subgrade - 1	Radial	-106	-106	490
	SS21	Subgrade - 1	Radial	212	-212	490
	SS5	Subgrade - 1	Radial	-318	318	490
	SS9	Subgrade - 1	Vertical	-65	0	525
	SS16	Subgrade - 1	Vertical	-200	0	525
	SS22	Subgrade - 1	Vertical	0	-300	525
	SS19	Subgrade - 1	Vertical	283	283	525
	SS23	Subgrade - 2	Vertical	-65	0	700
	SS24	Subgrade - 3	Vertical	-65	0	850
	SS25	Subgrade - 4	Vertical	-65	0	1150

Table A9 Instrument locations for test section CS11

Sensor	Name	Pavement Layer	Orientation	Location (mm)		
				x	y	z
Load Cell	LC	Surface	Vertical	0	0	0
Surface Deform. (LVDT)	SD1	Surface	Vertical	400	0	0
	SD2	Surface	Vertical	270	0	0
	SD3	Surface	Vertical	170	0	0
	SD4	Surface	Vertical	50	0	0
	SD5	Surface	Vertical	-50	0	0
	SD6	Surface	Vertical	-170	0	0
	SD7	Surface	Vertical	-270	0	0
	SD8	Surface	Vertical	-400	0	0
Stress Cell	SC1	Base -1	Radial	0	150	225
	SC2	Base - 2	Vertical	0	0	300
	SC4	Base - 2	Vertical	106	106	300
	SC6	Base - 2	Vertical	0	300	300
	SC7	Base - 2	Radial	141	-141	300
	SC12	Base - 2	Radial	0	-300	300
	SC11	Base - 2	Radial	-400	0	300
	SC13	Base - 2	Radial	0	-600	300
	SC15	Subgrade - 1	Vertical	0	0	450
	SC17	Subgrade - 1	Vertical	200	0	450
	SC19	Subgrade - 1	Radial	106	106	450
	SC20	Subgrade - 1	Radial	0	250	450
	SC21	Subgrade - 1	Radial	0	400	450
	SC22	Subgrade - 2	Vertical	0	0	625
	SC23	Subgrade - 3	Vertical	0	0	775
	SC24	Subgrade - 4	Vertical	0	0	1075
AC Strain Gages	AC1	AC	Radial	-150	0	67

Table A9 Continued.

Geosyn. Strain	GS1	Geogrid	Radial-T	0	20	375
	GS2	Geogrid	Radial-M	-15	0	375
	GS3	Geogrid	Radial-M	125	0	375
	GS4	Geogrid	Radial-T	0	-135	375
	GS5	Geogrid	Radial-M	-210	0	375
	GS6	Geogrid	Radial-M	335	0	375
	GS7	Geogrid	Radial-T	0	-412	375
Soil Strain (LVDT)	SS2	Base –1	Center -x-	0	0	225
	SS3	Base –1	Radial	0	-150	225
	SS7	Base – 2	Vertical	0	65	300
	SS8	Base – 2	Vertical	0	-150	300
	SS14	Base – 2	Vertical	-212	212	300
	SS4	Base – 2	Radial	-71	-71	325
	SS10	Base – 2	Radial	-200	0	325
	SS11	Base – 2	Radial	212	212	325
	SS17	Base – 2	Radial	0	400	325
	SS12	Base – 2	Tangential	100	0	325
	SS15	Base – 2	Tangential	0	200	325
	SS20	Subgrade - 1	Radial	-106	-106	415
	SS21	Subgrade - 1	Radial	212	-212	415
	SS5	Subgrade - 1	Radial	-318	318	415
	SS9	Subgrade - 1	Vertical	-65	0	450
	SS16	Subgrade - 1	Vertical	-200	0	450
	SS22	Subgrade - 1	Vertical	0	-300	450
	SS19	Subgrade - 1	Vertical	283	283	450
	SS23	Subgrade - 2	Vertical	-65	0	625
	SS24	Subgrade - 3	Vertical	-65	0	775
	SS25	Subgrade - 4	Vertical	-65	0	1075

Table A10 Instrument locations for test section SSS1

Sensor	Name	Pavement Layer	Orientation	Location (mm)		
				x	y	z
Load Cell	LC	Surface	Vertical	0	0	0
Surface Deform. (LVDT)	SD1	Surface	Vertical	400	0	0
	SD2	Surface	Vertical	270	0	0
	SD3	Surface	Vertical	170	0	0
	SD4	Surface	Vertical	50	0	0
	SD5	Surface	Vertical	-50	0	0
	SD6	Surface	Vertical	-170	0	0
	SD7	Surface	Vertical	-270	0	0
	SD8	Surface	Vertical	-400	0	0
Stress Cell	SC1	Base	Vertical	0	0	175
	SC2	Base	Vertical	148	145	175
	SC3	Base	Vertical	284	285	175
	SC4	Base	Radial	-157	5	161
	SC5	Base	Radial	315	0	158
	SC6	Base	Radial	-300	7	158
	SC7	Base	Radial	280	-283	158
	SC8	Base	Radial	610	20	158
	SC9	Base	Tangential	-71	70	158
	SC10	Base	Tangential	140	-143	167
	SC11	Base	Tangential	289	289	158
	SC12	Subgrade - 1	Vertical	3	0	350
	SC13	Subgrade - 1	Vertical	145	147	350
	SC14	Subgrade - 1	Vertical	-425	-430	350
	SC15	Subgrade - 1	Radial	-210	4	350
	SC16	Subgrade - 1	Radial	453	5	350
	SC17	Subgrade - 1	Tangential	0	147	350
	SC18	Subgrade - 1	Tangential	295	-5	350
	SC19	Subgrade - 2	Vertical	0	0	575
	SC20	Subgrade - 2	Vertical	210	210	581
	SC21	Subgrade - 2	Vertical	-566	-566	575
	SC22	Subgrade - 2	Radial	-340	0	578
	SC23	Subgrade - 2	Tangential	0	210	578
	SC24	Subgrade - 3	Vertical	0	-15	825
	SC25	Subgrade - 4	Vertical	0	0	1075
AC Strain Gages	AC1	AC	Horizontal	0	0	67
	AC2	AC	Radial	152	0	67
	AC3	AC	Tangential	0	150	67
	AC4	AC	Tangential	-300	0	67

Table A10 Continued.

Soil Strain (LVDT)	SS1	Base	Vertical	-45	-45	161
	SS2	Base	Vertical	-143	-141	160
	SS3	Base	Vertical	0	400	160
	SS4	Base	Radial	0	-160	215
	SS6	Base	Radial	-212	-212	215
	SS7	Base	Radial	0	-410	215
	SS8	Base	Radial	-600	0	215
	SS9	Base	Tangential	74	74	215
	SS10	Base	Tangential	200	0	215
	SS11	Base	Tangential	-281	-284	215
	SS12	Subgrade - 1	Vertical	-50	-50	350
	SS13	Subgrade - 1	Vertical	-145	-141	354
	SS14	Subgrade - 1	Vertical	415	430	351
	SS15	Subgrade - 1	Radial	0	-212	310
	SS16	Subgrade - 1	Radial	0	-450	310
	SS17	Subgrade - 1	Tangential	150	0	307
	SS18	Subgrade - 1	Tangential	0	300	311
	SS19	Subgrade - 2	Vertical	-36	-48	562
	SS20	Subgrade - 2	Vertical	-209	-210	568
	SS21	Subgrade - 2	Vertical	543	553	574
	SS22	Subgrade - 2	Radial	0	-350	574
	SS24	Subgrade - 3	Vertical	-50	-50	825
	SS25	Subgrade - 4	Vertical	-45	-45	1075
	MC1	Subgrade 2-3	Radial	0	-550	670
	MC2	Subgrade 3-4	Radial	0	550	920
TDR Probes	TP1	Base	NA	300	560	190
	TP2	Base	NA	300	-100	190
Temp. Probes	TP3	Base	NA	-150	-400	190
	TP4	Base	NA	-210	100	190
	TP5	Subgrade 1-2	NA	300	100	425
	TP6	Subgrade 1-2	NA	70	-70	425
	TP7	Subgrade 1-2	NA	-200	-400	425
	TP8	Subgrade 1-2	NA	-150	150	425
	TP9	Subgrade-3	NA	-70	50	825
	TP10	Subgrade-4	NA	-70	50	1075

Table A11 Instrument locations for test section SSS2

Sensor	Name	Pavement Layer	Orientation	Location (mm)		
				x	y	z
Load Cell	LC	Surface	Vertical	0	0	0
Surface Deform. (LVDT)	SD1	Surface	Vertical	400	0	0
	SD2	Surface	Vertical	270	0	0
	SD3	Surface	Vertical	170	0	0
	SD4	Surface	Vertical	50	0	0
	SD5	Surface	Vertical	-50	0	0
	SD6	Surface	Vertical	-170	0	0
	SD7	Surface	Vertical	-270	0	0
	SD8	Surface	Vertical	-400	0	0
Stress Cell	SC1	Base	Vertical	0	0	160
	SC2	Base	Vertical	143	148	160
	SC3	Base	Vertical	280	283	160
	SC4	Base	Radial	-152	-2	160
	SC5	Base	Radial	304	4	160
	SC6	Base	Radial	-298	0	160
	SC7	Base	Radial	285	-286	160
	SC8	Base	Radial	603	0	160
	SC9	Base	Tangential	-70	70	160
	SC10	Base	Tangential	138	-145	160
	SC11	Base	Tangential	-280	285	160
	SC12	Subgrade - 1	Vertical	0	0	350
	SC13	Subgrade - 1	Vertical	140	145	350
	SC14	Subgrade - 1	Vertical	-420	-425	350
	SC15	Subgrade - 1	Radial	-204	0	350
	SC16	Subgrade - 1	Radial	450	0	350
	SC17	Subgrade - 1	Tangential	2	153	350
	SC18	Subgrade - 1	Tangential	302	4	350
	SC19	Subgrade - 2	Vertical	0	0	575
	SC20	Subgrade - 2	Vertical	215	209	575
	SC21	Subgrade - 2	Vertical	-560	-562	575
	SC22	Subgrade - 2	Radial	-352	0	575
	SC23	Subgrade - 2	Tangential	3	205	575
	SC24	Subgrade - 3	Vertical	0	5	825
	SC25	Subgrade - 4	Vertical	0	0	1075
AC Strain Gages	AC1	AC	Horizontal	0	0	67
	AC2	AC	Radial	217	0	67
	AC3	AC	Tangential	0	150	67
	AC4	AC	Tangential	-300	0	67

Table A11 Continued.

Geosyn. Strain	GS1	Geogrid	Radial-M	15	0	160
	GS2	Geogrid	Radial-T	0	20	160
	GS3	Geogrid	Tangential-M	15	-117	160
	GS4	Geogrid	Radial-M	133	0	160
	GS5	Geogrid	Tangential-T	-117	20	160
	GS6	Geogrid	Radial-T	0	137	160
	GS7	Geogrid	Radial-M	-217	0	160
	GS8	Geogrid	Tangential-T	207	-20	160
	GS9	Geogrid	Tangential-M	-15	313	160
	GS10	Geogrid	Radial-T	0	-330	160
	GS11	Geogrid	Tangential-T	-622	20	160
	GS12	Geogrid	Radial-M	620	0	160
Soil Strain (LVDT)	SS1	Base	Vertical	-45	-45	160
	SS2	Base	Vertical	-146	-142	160
	SS3	Base	Vertical	0	400	160
	SS4	Base	Radial	0	-162	215
	SS5	Base	Radial	-2	303	215
	SS6	Base	Radial	-212	-212	215
	SS7	Base	Radial	0	-405	215
	SS8	Base	Radial	-595	0	215
	SS9	Base	Tangential	73	74	215
	SS10	Base	Tangential	204	0	215
	SS11	Base	Tangential	-283	-284	215
	SS12	Subgrade - 1	Vertical	-45	-45	350
	SS13	Subgrade - 1	Vertical	-142	-144	350
	SS14	Subgrade - 1	Vertical	420	425	350
	SS15	Subgrade - 1	Radial	0	-200	315
	SS16	Subgrade - 1	Radial	0	-453	315
	SS17	Subgrade - 1	Tangential	150	2	315
	SS18	Subgrade - 1	Tangential	0	302	315
	SS19	Subgrade - 2	Vertical	-45	-45	575
	SS20	Subgrade - 2	Vertical	-212	-213	575
	SS21	Subgrade - 2	Vertical	560	562	575
	SS22	Subgrade - 2	Radial	0	-350	575
	SS23	Subgrade - 2	Tangential	202	2	575
	SS25	Subgrade - 3	Vertical	-45	-45	825
	SS24	Subgrade - 4	Vertical	-45	-45	1075
TDR Probes	MC1	Subgrade 2-3	Radial	0	-550	670
	MC2	Subgrade 3-4	Radial	0	550	920
Temp. Probes	TP1	Base	NA	300	560	190
	TP2	Base	NA	300	-100	190
	TP3	Base	NA	-150	-400	190
	TP4	Base	NA	-210	100	190
	TP5	Subgrade 1-2	NA	300	100	425
	TP6	Subgrade 1-2	NA	70	-70	425
	TP7	Subgrade 1-2	NA	-200	-400	425
	TP8	Subgrade 1-2	NA	-150	150	425
	TP9	Subgrade-3	NA	-70	50	825
	TP10	Subgrade-4	NA	-70	50	1075

Table A12 Instrument locations for test section SSS3

Sensor	Name	Pavement Layer	Orientation	Location (mm)		
				x	y	z
Load Cell	LC	Surface	Vertical	0	0	0
Surface Deform. (LVDT)	SD1	Surface	Vertical	400	0	0
	SD2	Surface	Vertical	270	0	0
	SD3	Surface	Vertical	170	0	0
	SD4	Surface	Vertical	50	0	0
	SD5	Surface	Vertical	-50	0	0
	SD6	Surface	Vertical	-170	0	0
	SD7	Surface	Vertical	-270	0	0
	SD8	Surface	Vertical	-400	0	0
Stress Cell	SC1	Base	Vertical	0	0	160
	SC2	Base	Vertical	142	143	160
	SC3	Base	Vertical	283	283	160
	SC4	Base	Radial	-154	0	160
	SC5	Base	Radial	305	-2	160
	SC6	Base	Radial	-300	4	160
	SC7	Base	Radial	280	-281	160
	SC8	Base	Radial	605	0	160
	SC9	Base	Tangential	-71	70	160
	SC10	Base	Tangential	141	-145	160
	SC11	Base	Tangential	-284	285	160
	SC12	Subgrade - 1	Vertical	0	0	350
	SC13	Subgrade - 1	Vertical	142	140	350
	SC14	Subgrade - 1	Vertical	-427	-422	350
	SC15	Subgrade - 1	Radial	-205	-3	350
	SC16	Subgrade - 1	Radial	450	2	350
	SC17	Subgrade - 1	Tangential	0	150	350
	SC18	Subgrade - 1	Tangential	300	5	350
	SC19	Subgrade - 2	Vertical	0	2	575
	SC20	Subgrade - 2	Vertical	212	210	575
	SC21	Subgrade - 2	Vertical	-566	-566	575
	SC22	Subgrade - 2	Radial	-346	3	575
	SC23	Subgrade - 2	Tangential	0	205	575
	SC24	Subgrade - 3	Vertical	0	5	825
	SC25	Subgrade - 4	Vertical	0	0	1075
AC Strain Gages	AC1	AC	Horizontal	0	0	67
	AC2	AC	Radial	217	0	67
	AC3	AC	Tangential	0	150	67
	AC4	AC	Tangential	-300	0	67

Table A12 Continued.

Geosyn. Strain	GS1	Geotextile	Radial-M	-65	0	160
	GS2	Geotextile	Radial-T	0	-65	160
	GS3	Geotextile	Tangential-M	0	-200	160
	GS4	Geotextile	Radial-M	135	0	160
	GS5	Geotextile	Tangential-T	-200	0	160
	GS6	Geotextile	Radial-T	0	135	160
	GS7	Geotextile	Radial-M	-300	0	160
	GS8	Geotextile	Tangential-T	270	0	160
	GS9	Geotextile	Tangential-M	0	315	160
	GS10	Geotextile	Radial-T	0	-330	160
	GS11	Geotextile	Tangential-T	-620	0	160
	GS12	Geotextile	Radial-M	620	0	160
Soil Strain (LVDT)	SS1	Base	Vertical	-45	-45	160
	SS2	Base	Vertical	-140	-143	160
	SS3	Base	Vertical	-2	398	160
	SS4	Base	Radial	0	-154	215
	SS5	Base	Radial	1	297	215
	SS6	Base	Radial	-212	-214	215
	SS7	Base	Radial	3	-402	215
	SS8	Base	Radial	-603	2	215
	SS9	Base	Tangential	70	73	215
	SS10	Base	Tangential	200	0	215
	SS11	Base	Tangential	-286	-280	215
	SS12	Subgrade - 1	Vertical	-45	-45	350
	SS13	Subgrade - 1	Vertical	-143	-140	350
	SS14	Subgrade - 1	Vertical	423	428	350
	SS15	Subgrade - 1	Radial	0	-202	315
	SS5	Subgrade - 1	Radial	3	-454	315
	SS17	Subgrade - 1	Tangential	147	0	315
	SS18	Subgrade - 1	Tangential	5	303	315
	SS19	Subgrade - 2	Vertical	-45	-45	575
	SS20	Subgrade - 2	Vertical	-210	-209	575
	SS21	Subgrade - 2	Vertical	560	560	575
	SS22	Subgrade - 2	Radial	0	-345	575
	SS16	Subgrade - 3	Vertical	-45	-45	825
	SS25	Subgrade - 4	Vertical	-45	-45	1075
TDR Probes	MC1	Subgrade 2-3	Radial	0	-550	670
	MC2	Subgrade 3-4	Radial	0	550	920
Temp. Probes	TP1	Base	NA	300	560	190
	TP2	Base	NA	300	-100	190
	TP3	Base	NA	-150	-400	190
	TP4	Base	NA	-210	100	190
	TP5	Subgrade 1-2	NA	300	100	425
	TP6	Subgrade 1-2	NA	70	-70	425
	TP7	Subgrade 1-2	NA	-200	-400	425
	TP8	Subgrade 1-2	NA	-150	150	425
	TP9	Subgrade-3	NA	-70	50	825
	TP10	Subgrade-4	NA	-70	50	1075

Table A13 Instrument locations for test section SSS4

Sensor	Name	Pavement Layer	Orientation	Location (mm)		
				x	y	z
Load Cell	LC	Surface	Vertical	0	0	0
Surface Deform. (LVDT)	SD1	Surface	Vertical	400	0	0
	SD2	Surface	Vertical	270	0	0
	SD3	Surface	Vertical	170	0	0
	SD4	Surface	Vertical	50	0	0
	SD5	Surface	Vertical	-50	0	0
	SD6	Surface	Vertical	-170	0	0
	SD7	Surface	Vertical	-270	0	0
	SD8	Surface	Vertical	-400	0	0
Stress Cell	SC1	Base	Vertical	0	0	160
	SC2	Base	Vertical	107	107	160
	SC3	Base	Vertical	210	212	160
	SC4	Base	Radial	0	-103	160
	SC5	Base	Radial	-197	0	160
	SC6	Base	Radial	298	0	160
	SC7	Base	Radial	282	-282	160
	SC8	Base	Radial	604	0	160
	SC9	Base	Tangential	-70	70	160
	SC10	Base	Tangential	-140	-142	160
	SC11	Base	Tangential	-280	282	160
	SC12	Subgrade - 1	Vertical	0	0	350
	SC13	Subgrade - 1	Vertical	143	140	350
	SC14	Subgrade - 1	Vertical	-280	-284	350
	SC15	Subgrade - 1	Radial	-145	2	350
	SC16	Subgrade - 1	Radial	0	-298	350
	SC17	Subgrade - 1	Radial	451	-2	350
	SC18	Subgrade - 1	Tangential	-3	152	350
	SC19	Subgrade - 2	Tangential	297	0	575
	SC20	Subgrade - 2	Vertical	0	0	575
	SC21	Subgrade - 2	Vertical	210	215	575
	SC22	Subgrade - 2	Radial	-348	3	575
	SC23	Subgrade - 2	Tangential	2	202	575
	SC24	Subgrade - 3	Vertical	0	0	825
	SC25	Subgrade - 4	Vertical	0	0	1075
AC Strain Gages	AC1	AC	Center	0	0	67
	AC2	AC	Radial	219	0	67
	AC3	AC	Tangential	0	152	67
	AC4	AC	Tangential	-300	0	67

Table A13 Continued.

Soil Strain (LVDT)	SS1	Base	Vertical	-45	-45	160
	SS2	Base	Vertical	-109	-110	160
	SS3	Base	Vertical	0	-300	160
	SS4	Base	Radial	70	-72	215
	SS5	Base	Radial	0	203	215
	SS6	Base	Radial	-210	-210	215
	SS7	Base	Radial	0	-404	215
	SS8	Base	Radial	-604	0	215
	SS9	Base	Tangential	70	72	215
	SS10	Base	Tangential	203	0	215
	SS11	Base	Tangential	-280	-279	215
	SS12	Subgrade - 1	Vertical	-45	-45	350
	SS13	Subgrade - 1	Vertical	-140	-141	350
	SS14	Subgrade - 1	Vertical	280	282	350
	SS15	Subgrade - 1	Radial	-4	-148	315
	SS16	Subgrade - 1	Radial	-298	5	315
	SS17	Subgrade - 1	Radial	-3	-454	315
	SS18	Subgrade - 1	Tangential	152	0	315
	SS19	Subgrade - 2	Tangential	0	304	575
	SS20	Subgrade - 2	Vertical	-45	-45	575
	SS21	Subgrade - 2	Vertical	-210	-213	575
	SS22	Subgrade - 2	Radial	-3	-350	575
	SS23	Subgrade - 2	Tangential	201	-2	575
	SS24	Subgrade - 3	Vertical	-45	-45	825
	SS25	Subgrade - 4	Vertical	-45	-45	1075
TDR Probes	MC1	Subgrade 2-3	Radial	0	-550	675
	MC2	Subgrade 3-4	Radial	0	550	925
Temp. Probes	TP1	Base	NA	180	350	190
	TP2	Base	NA	210	-300	190
	TP3	Base	NA	-150	-420	190
	TP4	Base	NA	-350	220	190
	TP5	Subgrade 1-2	NA	300	100	425
	TP6	Subgrade 1-2	NA	70	-70	425
	TP7	Subgrade 1-2	NA	-200	-400	425
	TP8	Subgrade 1-2	NA	-150	150	425
	TP9	Subgrade-3	NA	-70	50	825
	TP10	Subgrade-4	NA	-70	50	1075

Table A14 Instrument locations for test section SSS5

Sensor	Name	Pavement Layer	Orientation	Location (mm)		
				x	y	z
Load Cell	LC	Surface	Vertical	0	0	0
Surface Deform. (LVDT)	SD1	Surface	Vertical	400	0	0
	SD2	Surface	Vertical	270	0	0
	SD3	Surface	Vertical	170	0	0
	SD4	Surface	Vertical	50	0	0
	SD5	Surface	Vertical	-50	0	0
	SD6	Surface	Vertical	-170	0	0
	SD7	Surface	Vertical	-270	0	0
	SD8	Surface	Vertical	-400	0	0
Stress Cell	SC1	Base	Vertical	0	0	160
	SC2	Base	Vertical	106	110	160
	SC3	Base	Vertical	212	210	160
	SC4	Base	Radial	0	-98	160
	SC5	Base	Radial	-202	3	160
	SC6	Base	Radial	297	4	160
	SC7	Base	Radial	281	-280	160
	SC8	Base	Radial	599	0	160
	SC9	Base	Tangential	-72	72	160
	SC10	Base	Tangential	-139	-140	160
	SC11	Base	Tangential	-282	279	160
	SC12	Subgrade - 1	Vertical	0	0	350
	SC13	Subgrade - 1	Vertical	143	140	350
	SC14	Subgrade - 1	Vertical	-280	-284	350
	SC15	Subgrade - 1	Radial	-145	2	350
	SC16	Subgrade - 1	Radial	0	-298	350
	SC17	Subgrade - 1	Radial	451	-2	350
	SC18	Subgrade - 1	Tangential	-3	152	350
	SC19	Subgrade - 2	Tangential	297	0	575
	SC20	Subgrade - 2	Vertical	0	0	575
	SC21	Subgrade - 2	Vertical	210	215	575
	SC22	Subgrade - 2	Radial	-348	3	575
	SC23	Subgrade - 2	Tangential	2	202	575
	SC24	Subgrade - 3	Vertical	0	0	825
	SC25	Subgrade - 4	Vertical	0	0	1075
AC Strain Gages	AC1	AC	Center	0	0	67

Table A14 Continued.

Geosyn. Strain	GS1	Geogrid	Radial-M	15	0	275
	GS2	Geogrid	Radial-T	0	-20	275
	GS3	Geogrid	Tangential-M	15	-117	275
	GS4	Geogrid	Radial-M	127	0	275
	GS5	Geogrid	Tangential-T	-111	22	275
	GS6	Geogrid	Radial-T	0	135	275
	GS7	Geogrid	Radial-M	-215	0	275
	GS8	Geogrid	Tangential-T	197	-20	275
	GS9	Geogrid	Tangential-M	-15	305	275
	GS10	Geogrid	Radial-T	0	-330	275
	GS11	Geogrid	Tangential-T	-613	20	275
	GS12	Geogrid	Radial-M	597	0	275
Soil Strain (LVDT)	SS1	Base	Vertical	-45	-45	160
	SS2	Base	Vertical	-107	-106	160
	SS3	Base	Vertical	0	-298	160
	SS4	Base	Radial	73	-75	215
	SS5	Base	Radial	0	206	215
	SS6	Base	Radial	-209	-210	215
	SS7	Base	Radial	0	-400	215
	SS8	Base	Radial	-600	3	215
	SS9	Base	Tangential	73	74	215
	SS10	Base	Tangential	201	-3	215
	SS11	Base	Tangential	-283	-284	215
	SS12	Subgrade - 1	Vertical	-45	-45	350
	SS13	Subgrade - 1	Vertical	-140	-141	350
	SS14	Subgrade - 1	Vertical	280	282	350
	SS15	Subgrade - 1	Radial	-4	-148	315
	SS16	Subgrade - 1	Radial	-298	5	315
	SS17	Subgrade - 1	Radial	-3	-454	315
	SS18	Subgrade - 1	Tangential	152	0	315
	SS19	Subgrade - 2	Tangential	0	304	575
	SS20	Subgrade - 2	Vertical	-45	-45	575
	SS21	Subgrade - 2	Vertical	-210	-213	575
	SS22	Subgrade - 2	Radial	-3	-350	575
	SS23	Subgrade - 2	Tangential	201	-2	575
	SS24	Subgrade - 3	Vertical	-45	-45	825
	SS25	Subgrade - 4	Vertical	-45	-45	1075
TDR Probes	MC1	Subgrade 2-3	Radial	0	-550	675
	MC2	Subgrade 3-4	Radial	0	550	925
Temp. Probes	TP1	Base	NA	180	350	190
	TP2	Base	NA	210	-300	190
	TP3	Base	NA	-150	-420	190
	TP4	Base	NA	-350	220	190
	TP5	Subgrade 1-2	NA	300	100	425
	TP6	Subgrade 1-2	NA	70	-70	425
	TP7	Subgrade 1-2	NA	-200	-400	425
	TP8	Subgrade 1-2	NA	-150	150	425
	TP9	Subgrade-3	NA	-70	50	825
	TP10	Subgrade-4	NA	-70	50	1075

Table A15 Instrument locations for test section SSS8

Sensor	Name	Pavement Layer	Orientation	Location (mm)		
				x	y	z
Load Cell	LC	Surface	Vertical	0	0	0
Surface Deform. (LVDT)	SD1	Surface	Vertical	400	0	0
	SD2	Surface	Vertical	270	0	0
	SD3	Surface	Vertical	170	0	0
	SD4	Surface	Vertical	50	0	0
	SD5	Surface	Vertical	-50	0	0
	SD6	Surface	Vertical	-170	0	0
	SD7	Surface	Vertical	-270	0	0
	SD8	Surface	Vertical	-400	0	0
Stress Cell	SC1	Base	Vertical	0	0	160
	SC2	Base	Vertical	108	105	160
	SC3	Base	Vertical	215	215	160
	SC4	Base	Radial	0	-104	160
	SC5	Base	Radial	-198	0	160
	SC6	Base	Radial	304	0	160
	SC7	Base	Radial	284	-284	160
	SC8	Base	Radial	595	0	160
	SC9	Base	Tangential	-73	70	160
	SC10	Base	Tangential	-142	-141	160
	SC11	Base	Tangential	-285	283	160
	SC12	Subgrade - 1	Vertical	0	0	350
	SC13	Subgrade - 1	Vertical	143	140	350
	SC14	Subgrade - 1	Vertical	-280	-284	350
	SC15	Subgrade - 1	Radial	-145	2	350
	SC16	Subgrade - 1	Radial	0	-298	350
	SC17	Subgrade - 1	Radial	451	-2	350
	SC18	Subgrade - 1	Tangential	-3	152	350
	SC19	Subgrade - 2	Tangential	297	0	575
	SC20	Subgrade - 2	Vertical	0	0	575
	SC21	Subgrade - 2	Vertical	210	215	575
	SC22	Subgrade - 2	Radial	-348	3	575
	SC23	Subgrade - 2	Tangential	2	202	575
	SC24	Subgrade - 3	Vertical	0	0	825
	SC25	Subgrade - 4	Vertical	0	0	1075
AC Strain Gages	AC1	AC	Center	0	0	67
	AC2	AC	Radial	219	0	67
	AC3	AC	Tangential	0	152	67
	AC4	AC	Tangential	-300	0	67

Table A15 Continued.

Geosyn. Strain	GS1	Geotextile	Radial-M	-65	0	275
	GS2	Geotextile	Radial-T	0	-65	275
	GS3	Geotextile	Tangential-M	0	-200	275
	GS4	Geotextile	Radial-M	135	0	275
	GS6	Geotextile	Radial-T	0	135	275
	GS7	Geotextile	Radial-M	-300	0	275
	GS9	Geotextile	Tangential-M	0	315	275
	GS11	Geotextile	Tangential-T	-620	0	275
Soil Strain (LVDT)	SS1	Base	Vertical	-45	-45	160
	SS2	Base	Vertical	-108	-108	160
	SS3	Base	Vertical	0	-305	160
	SS4	Base	Radial	70	-70	215
	SS5	Base	Radial	0	200	215
	SS6	Base	Radial	-215	-212	215
	SS7	Base	Radial	2	-405	215
	SS8	Base	Radial	-605	0	215
	SS9	Base	Tangential	71	71	215
	SS10	Base	Tangential	200	0	215
	SS11	Base	Tangential	-285	-285	215
	SS12	Subgrade - 1	Vertical	-45	-45	350
	SS13	Subgrade - 1	Vertical	-140	-141	350
	SS14	Subgrade - 1	Vertical	280	282	350
	SS15	Subgrade - 1	Radial	-4	-148	315
	SS16	Subgrade - 1	Radial	-298	5	315
	SS17	Subgrade - 1	Radial	-3	-454	315
	SS18	Subgrade - 1	Tangential	152	0	315
	SS19	Subgrade - 2	Tangential	0	304	575
	SS20	Subgrade - 2	Vertical	-45	-45	575
	SS21	Subgrade - 2	Vertical	-210	-213	575
	SS22	Subgrade - 2	Radial	-3	-350	575
	SS23	Subgrade - 2	Tangential	201	-2	575
	SS24	Subgrade - 3	Vertical	-45	-45	825
	SS25	Subgrade - 4	Vertical	-45	-45	1075
TDR Probes	MC1	Subgrade 2-3	Radial	0	-550	675
	MC2	Subgrade 3-4	Radial	0	550	925
Temp. Probes	TP1	Base	NA	180	350	190
	TP2	Base	NA	210	-300	190
	TP3	Base	NA	-150	-420	190
	TP4	Base	NA	-350	220	190
	TP5	Subgrade 1-2	NA	300	100	425
	TP6	Subgrade 1-2	NA	70	-70	425
	TP7	Subgrade 1-2	NA	-200	-400	425
	TP8	Subgrade 1-2	NA	-150	150	425
	TP9	Subgrade-3	NA	-70	50	825
	TP10	Subgrade-4	NA	-70	50	1075